VNIVERSITAT DE VALÈNCIA

Escola Tècnica Superior d'Enginyeria ETSE-UV

Doctoral Programme in Electronic Engineering

Doctoral Thesis

Design and Development of Safety and Control Systems in ATLAS

Author:

Ignacio Asensi Tortajada

Supervisor:

Dr. Eng. José Torres País

Universitat de València (UV)

Department of Electronic Engineering

Co-supervisor:

Dr. Carlos Solans Sánchez

CERN Staff Scientist

Department of Experimental Physics

Valencia, Spain - September 2021

A dissertation submitted to the University of València
for the degree of Doctor of Philosophy.

VNIVERSITAT DE VALÈNCIA | Escola Tècnica Superior d'Enginyeria ETSE-UV

Declaration

D. JOSÉ TORRES PAÍS, Doctor en Ingeniería Electrónica, Profesor Titular del Departamento de Ingeniería Electrónica de la Escola Tècnica Superior d'Enginyeria de la Universitat de València y D. CARLOS SOLANS SÁNCHEZ, Doctor en Física, científico en la Organización Europea para la Investigación Nuclear

HACEN CONSTAR QUE:

D. IGNACIO ASENSI TORTAJADA, ha realizado bajo su dirección el trabajo titulado "Design and Development of Safety and Control Systems in ATLAS", que se presenta en esta memoria para optar al grado de Doctor por la Universitat de València. Y para que así conste a los efectos oportunos, y dando su conformidad para la presentación de este trabajo delante del Tribunal de Tesis Doctoral que corresponda, firma el presente certificado, en Valencia, a 15 de Junio de 2021.

Fdo. D. José Torres País
UNIVERSITAT DE VALÈNCIA
ESCOLA TÈCNICA SUPERIOR D'ENGINYERIA
Departamento de Ingeniería Electrónica
Av. De la Universidad s/n, 46100 Burjassot (Valencia)

Fdo. D. Carlos Solans Sánchez
CERN
1211 Geneva 23
Switzerland

Acta de calificación

Tesis Doctoral:	DESIGN AND DEVELOPMENT OF SAFETY AND CONTROL SYSTEMS IN ATLAS
Autor:	IGNACIO ASENSI TORTAJADA
Director:	DR. JOSÉ TORRES PAÍS
Codirector:	DR. CARLOS SOLANS SÁNCHEZ

El Tribunal nombrado para juzgar la Tesis Doctoral citada anteriormente, compuesto por los doctores:

Presidente: _____

Vocal: _____

Secretario: _____

Acuerda otorgarle la calificación de: _____

Y para que así conste a los efectos oportunos, firmamos el presente certificado.

En Valencia, el _____ de _____ de 2021

Contents

Resumen

Contexto de investigación y motivación

El gran colisionador de hadrones, o LHC, es el acelerador de partículas más grande y potente del mundo. Ha sido construido por el CERN, la Organización Europea para la Investigación Nuclear, entre 1998 y 2008 en Ginebra, Suiza. Sucesivas mejoras en el LHC supondrán a partir de mediados del 2027 un incremento de la luminosidad, cuando pasará a llamarse High Luminosity LHC (HL-LHC).

ATLAS es un detector multi-propósito y el experimento más grande de los cuatro principales situados en LHC, su construcción se inició en 2003 y comenzó a funcionar en 2008. Consiste en una compleja infraestructura que se extiende a lo largo de una caverna experimental, donde se encuentra el detector, y dos cavernas de servicios. ATLAS está compuesto por sub-detectores y una infraestructura que incluye sistemas electrónicos, generación de campos magnéticos, distribución de gas, criogenia y refrigeración. La interdependencia entre los sistemas es tan elevada que el comportamiento de todo el detector es muy difícil de predecir en caso de mal funcionamiento de uno de sus componentes.

Esta tesis se divide en dos partes, por una parte la seguridad y operación de la infraestructura y por otra los sistemas de control y toma de datos.

La primera parte de la tesis se dedica a la seguridad y operación de la infraestructura. Después de más de 10 años de funcionamiento, el riesgo de posibles fallos en elementos de la infraestructura derivados de su envejecimiento supone un peligro con posibles consecuencias para la operación en tiempo y coste a pesar del constante mantenimiento. Igualmente, las continuas mejoras y modificaciones a las que se somete la infraestructura, aumentan la necesidad de una mejor base de conocimiento y de su transferencia entre los expertos de los diferentes sistemas que forman el experimento.

El envejecimiento de los sistemas aumenta el riesgo de funcionamiento incorrecto en los sistemas de refrigeración principales y los cercanos a la electrónica suponiendo un mayor riesgo de inundaciones y daños en componentes electrónicos de difícil sustitución. Los sistemas de detección convencionales se basan en pequeños sensores cuya superficie de actuación se limita a la inmediata proximidad del sensor. Sin embargo, la rápida detección de pequeñas y grandes cantidades de agua, en lugares de restringido acceso y en grandes superficies es necesaria. En consecuencia, la investigación sigue una estrategia en la que se incluye materiales que proporcionan mayor superficie supervisada a coste inferior. Los resultados mostraron grandes posibilidades en los materiales basados en nanotubos de carbono.

Adicionalmente, el conocimiento de la infraestructura que se encuentra en constante cambio es un reto cada vez mayor al que se enfrentan los expertos, para su correcto mantenimiento y operaciones de mejora. Por ello en la tesis se plantean dos hipótesis relativas a la seguridad de la infraestructura de ATLAS: ¿Puede mejorar la seguridad del detector mediante el uso de nuevos sensores? ¿Podría un Sistema Experto proporcionar mayor conocimiento y seguridad en las operaciones de mantenimiento y operación en la infraestructura de ATLAS?

La segunda parte de la tesis se centra en los sistemas de control y toma de datos utilizados para la caracterización de sensores de Píxel monolíticos en TowerJazz 180 nm. Los sensores de Píxel monolíticos muestran un potencial muy grande para la física de altas energías, sin embargo, siguen limitados por su resistencia a la radiación y facilidad de uso en experimentos como ATLAS. Existe una necesidad de mayor modularidad, adaptabilidad y flexibilidad para caracterizar los detectores de Píxel monolíticos. Sistemas de caracterización utilizados previamente se basan en osciloscopios y sistemas dedicados. El uso de FPGAs puede proporcionar mayor precisión y velocidad en la toma de datos de una forma que no es escalable con osciloscopios y con un coste más reducido que con anteriores tecnologías. En este contexto, en la presente tesis se plantea la siguiente hipótesis. ¿Puede el uso de FPGAs reemplazar la tecnología previa en caracterización de los sensores de Píxel?

Objetivos

Teniendo en cuenta el contexto de la investigación y las motivaciones mencionadas, el objetivo general de la presente tesis doctoral es el siguiente:

La investigación y desarrollo de nuevas soluciones para mejorar la seguridad del detector frente a fugas de agua y el control de los sistemas de Píxel en estado de I+D para ATLAS, reduciendo el impacto de las operaciones en el detector y los costes en la toma de datos para el Run 4, durante el tiempo de operación y de mantenimiento.

Se propone los siguientes objetivos específicos para la realización de la investigación a las hipótesis previamente planteadas:

1. Diseño y desarrollo de un Sistema Experto para ATLAS. El sistema debe emular el razonamiento de los expertos siendo capaz de entender preguntas y proporcionar respuestas. Para ello se ha de diseñar y recopilar una base de conocimiento detallado de las partes críticas del detector como los sistemas de seguridad, grupos de gas, refrigeración, criogenia, campos magnéticos y electricidad. Se ha de diseñar un sistema de inferencia lógica que interprete la base de conocimiento para producir simulaciones y mostrar de forma comprensible el comportamiento de ATLAS, respondiendo a los escenarios que se le plantean.

2. Diseño y desarrollo de un sistema para la detección y actuación en caso de fugas de agua. El sistema tiene como objetivo reemplazar la tecnología existente en el marco de los sistemas de supervisión para el *Run* 4 de ATLAS. El nuevo sistema debe reducir activamente el riesgo constante de fugas en los circuitos de refrigeración y ser capaz de cubrir grandes superficies con una alta sensibilidad y rápida velocidad de actuación con un bajo coste.

3. Demostrar la flexibilidad de las FPGAs para su uso en la caracterización de sensores de Píxel monolíticos mediante el diseño y construcción de una Unidad de Trigger Lógica para la toma de datos con un telescopio para haces de partículas. La nueva unidad debe aportar mayor control, flexibilidad y reducción de costes. Adicionalmente se ha de desarrollar e implementar el entorno de análisis de la resistencia a la radiación de las memorias de tecnología de Towerjazz 180 nm.

Metodología

La presente tesis doctoral se basa en el trabajo de investigación desarrollado en el experimento de ATLAS en el CERN, en el marco de la colaboración entre el grupo EP-ADE del CERN y la Universidad de Valencia como miembro del grupo EP-ADE. En los siguientes puntos se describe la metodología e investigación llevada a cabo con el objetivo de alcanzar los objetivos previamente enumerados.

El experimento ATLAS del LHC

Este capítulo describe el experimento de ATLAS en el LHC, sus sub-detectores e infraestructura; y se enumeran los criterios básicos de su diseño. La infraestructura se describe a través de sus edificios, racks, estaciones de refrigeración, distribución eléctrica, de gas, criogenia y sistemas de seguridad. La mayor parte de la infraestructura descrita en este capítulo serán los componentes que se describan en el Sistema Experto.

Sistema Experto de ATLAS

En este capítulo se describe como partiendo de la consideración de la infraestructura como un complejo árbol de dependencias, se ha creado un Sistema Experto basado en objetos, que es capaz de simular las reacciones de la infraestructura como respuesta a los escenarios presentados por un usuario.

El Sistema Experto de ATLAS contiene una base de conocimiento sobre la infraestructura, presentada al usuario a través de diagramas similares a los utilizados en los sistemas SCADA y de interfaces de búsqueda. Las motivaciones del Sistema Experto son desarrollar el conocimiento de la infraestructura como conjunto, reducir el riesgo de efectos inesperados en las intervenciones y comprender las causas de situaciones inesperadas en la infraestructura. Sus principales objetivos son:

- Describir la infraestructura de ATLAS con sus elementos e interconexiones entre ellos de forma comprensible para usuarios de ATLAS provenientes de diferentes disciplinas y con diferentes niveles de conocimiento.

- Emular de forma rápida el comportamiento de los sistemas en cualquier escenario propuesto por el usuario.

- Utilizar tecnologías estándar para facilitar su manteamiento durante la vida del detector.

Los sistemas representados en la infraestructura incluyen: campos magnéticos, gas, refrigeración, criogenia, ventilación, electricidad y sistemas de seguridad incluyendo DSS.

La arquitectura del sistema está compuesta por una base de datos orientada a objetos, un servidor de simulaciones y una aplicación web cliente-servidor. La Figura 1 muestra tres bloques físicos, el bloque de la izquierda consiste en una máquina virtual que contiene la base de datos y el servidor de Python, el bloque central es el servidor web que ejecuta la aplicación web y el bloque de la derecha es el cliente donde se ejecuta la interfaz gráfica.

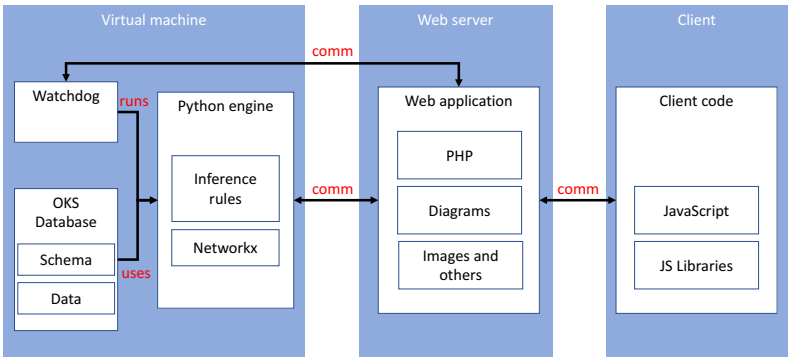

Figura 1: Diagrama de la arquitectura del Sistema Experto de ATLAS

Se utiliza una base de datos de objetos del sistema de Trigger de ATLAS (OKS), que será la misma durante la vida del experimento. Los objetos están implementados como instancias de las clases descritas en la propia la base de datos, que contienen atributos y relaciones a otros objetos. El servidor de simulaciones controla la deducción lógica aplicando reglas en relación con las clases de los objetos en la base de datos. El sistema aloja en memoria un grafo de objetos basado en la red de sistemas descritos en la base de datos, con ayuda de la herramienta Networkx. Cuando el servidor recibe una propuesta de cambio en la infraestructura por un usuario, aplica las reglas para deducir el estado de los objetos en el nuevo escenario. Una vez terminado el proceso, envía el nuevo estado de la infraestructura a la interfaz donde se presenta al usuario, el cual puede continuar interactuando con el sistema. La comunicación entre cliente y servidor se realiza a través de un protocolo creado para la aplicación basado en tecnologías

comúnmente utilizadas como AJAX y JQuery, y protocolos de datos como JSON.

Se han desarrollado dos tipos de interfaz de usuario, una basada en tablas y listas de búsqueda que proveen de información detallada sobre los objetos y sus dependencias y otra de tipo visual basada en diagramas. La Figura 2 muestra la página de seguridad del detector con su diagrama. La barra superior azul contiene de izquierda a derecha el acceso al menú de la aplicación, nombre de la página actual, número de alarmas y sistemas afectados, idioma, un botón para reiniciar escenario, caja de búsqueda y tiempo de la simulación. El diagrama está dividido en localizaciones físicas cuyo nombre Figura en la esquina superior izquierda y dentro de ellas hay pequeñas cajas que representan sistemas o grupos de sistemas con tres iconos por caja. Se ha establecido una convención de colores para definir tipo de localización y tipo de sistema. Los iconos permiten apagar o encender el sistema, observar su estado y obtener más información. En las cajas que representan grupos un icono permite desplegar su contenido.

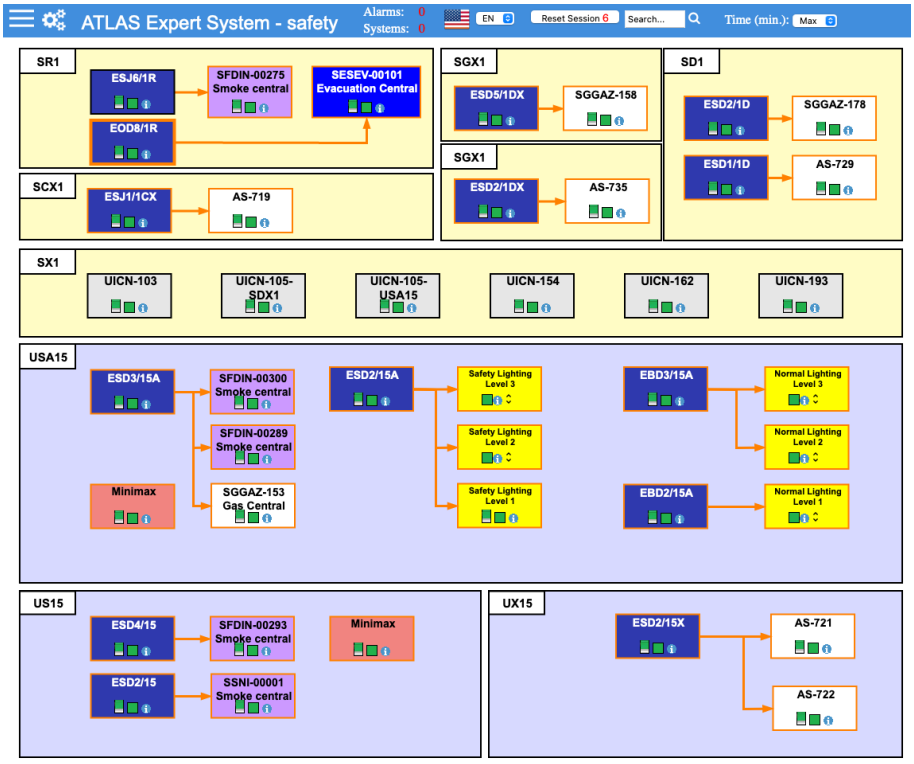

Figura 2: Expert System safety page

Los elementos de la infraestructura están representados en la base de datos como objetos que instancian una clase. Las clases tienen relaciones con otras en las que

pueden proveer a la otra clase (*provide*) o recibir (*feed*), de esta forma se definen respectivamente como relaciones padre-hijo. Padre es el que provee y el hijo el que recibe. Cuando una simulación es iniciada debido a un cambio en un sistema provocado por el usuario, se calcula el estado de cada objeto de la base de datos según el estado de sus objetos padre. Como ejemplo, un rack de ordenadores se describe mediante la clase *Rack* en la base de datos y tiene relaciones como: fuentes de energía (*poweredBy*), elementos contenidos (*contains*), sistemas a que puede bloquear (*interlocks*), requerimientos de refrigeración (*waterFrom*). Cuando se resuelve el estado de un objeto todas las relaciones son consideradas al mismo tiempo.

Se ha establecido un modelo para estimar la fiabilidad de partes de la infraestructura mediante el Sistema Experto de ATLAS en el que la probabilidad supervivencia (P_s de *Probability of survival*) de un sistema supone la probabilidad de cumplir con su tarea y la probabilidad de fallo (P_f) se calcula como $P_f = 1 - P_s$. Se asume que la P_s de cada sistema puede ser inferida desde la base de conocimiento. Se genera un diagrama de bloques de fiabilidad para un sistema como un árbol de fallas en el que todos los elementos que afectan a la fiabilidad de un sistema son representados como nodos con una entrada y una salida. La P_s de un sistema será la composición de la P_s de todos sus nodos. Se considera la probabilidad de éxito de nodos en serie (P_s^s) y en paralelo (P_s^p), siendo en serie aquellos cuyo resultado depende del funcionamiento de todos sus elementos y en paralelo aquellos cuyo funcionamiento depende de al menos un elemento. Se puede deducir el principal componente de un sistema mediante el cálculo de la probabilidad de fallo de todos sus nodos. El procedimiento se reduce a un análisis de P_s de cada uno de los nodos en cada iteración. El efecto de cada componente del sistema permite la deducción del componente principal.

El cálculo de la causa más probable (*Most Probable Cause*) ha sido implementado en el Sistema de Experto para permitir una rápida estimación de la posible causa para el escenario presentado. El usuario propone un escenario mediante una lista de sistemas afectados y el Sistema Experto calcula de forma exhaustiva los padres comunes de los integrantes de la lista. Eso se consigue mediante un orden de resolución determinado por un algoritmo de búsqueda en anchura (*Breadth-first search*). Después, mediante un filtro, se seleccionan únicamente los padres que afectan a todos los objetos listados por el usuario. La búsqueda se puede realizar de forma no exhaustiva para los casos en los que el usuario no sabe con certeza el número de sistemas afectados. El uso de esta

herramienta en la sala de control y por parte de los expertos dará lugar a una mayor comprensión de las situaciones inesperadas durante la operación.

Detectores de Píxel

En el capítulo dedicado a los detectores de Píxel se describen los procesos de interacción de las partículas con la materia relevantes para este estudio, como la pérdida de energía por ionización, la curva de Bethe-Bloch, y los procesos foto-eléctrico, Compton y creación de pares para los fotones, que dependen de la partícula, su energía y el numero atómico y la densidad del material.

Los sensores de píxel se basan en el concepto de un diodo polarizado inversamente para detectar el paso de las partículas. Los diodos utilizan una unión de dos partes de silicio, una con dopaje negativo (*n-type*), donante de electrones y otra positivo (*p-type*), receptor de electrones. Esto forma lo que se denomina unión PN (*p-n junction*). Una creación de pares fruto del paso de una partícula es detectada gracias a una corriente generada en el diodo. Se contextualiza la tecnología CMOS, un proceso industrial que permite la realización de circuitos integrados que contienen dos polaridades de transistores MOS en el mismo chip. Gracias al silicio se puede crear un gran número de uniones PN en un solo chip divididas en píxeles.

Se describen los efectos derivados de la radiación en detectores de silicio que se dividen en tres, los dados por la dosis total de ionización (TID), pérdida de energía no-ionizante (NIEL) y aquellos que producen errores de estado (SEE) en un dispositivo. La TID afecta al funcionamiento de los transistores y el NIEL crea defectos en la red cristalina del silicio cambiando sus propiedades reduciendo eficiencia. Los eventos de error de estado causados por la radiación en la electrónica se dividen en aquellos temporales como el *Single Event Upset* (SEU) o causar daños permanentes como los debidos a un *Single Event Latchup* (SEL).

La familia de detectores de Píxel monolíticos de MALTA está siendo desarrollada para el HL-LHC y futuros experimentos. Son fabricados por ToweJazz mediante un proceso CMOS de 180 nm. Con un tamaño de píxel de 36.4×36.4 μm^2 y una matriz de 512×512 píxeles en MALTA y 16×64 píxeles en Mini-MALTA, mostrada en la Figura 3.

La matriz ocupa la mayor parte del chip y está dividida en sectores con distintas configuraciones y procesos de fabricación de los píxeles para su análisis. Además de

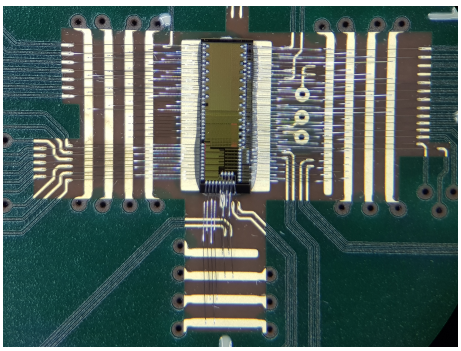

Figura 3: Detalle del chip Mini-MALTA soldado a la placa de pruebas

la matriz, los chips contienen la electrónica necesaria para su operación, reloj, control y lectura. Los chips son *wire-bonded* a una placa de pruebas y la lectura se realiza a través de tarjetas de evaluación de FPGAs comerciales de la serie 7 de Xilinx, como la Kintex KC705 a través del conector FMC (FPGA Mezzanine Card). La diferencia entre MALTA y Mini-MALTA es la arquitectura de lectura, MALTA es asíncrono, con 37 salidas diferenciales, mientras que Mini-MALTA es síncrono a 40 MHz.

Los parámetros más importantes para la caracterización de un detector de Píxel son la relación señal-ruido (SNR), la eficiencia y el umbral (*threshold*) de detección (producción de *hits*). Las pruebas para la caracterización de los chips se suelen realizar en instalaciones utilizando un haz de partículas y valiéndose de un telescopio para haces de partículas que permite la reconstrucción de las trazas de las partículas, siendo este un punto clave de esta investigación.

El chip SEU_TJ180 ha sido desarrollado y fabricado para el estudio de los efectos de la radiación en las memorias de la tecnología utilizada por Towerjazz 180 nm. Tiene tres tipos de memorias: una SPRAM con un bloque de un array de 16 puertos de 1024 bits, una DPRAM con un array de 8 puertos duales de 2048 bits y una memoria de registro de desplazamiento (*shift register*) de 16 canales.

Sistemas de control en física de altas energías

El capítulo está dedicado a describir las contribuciones a la investigación y desarrollo de sensores de Píxel monolíticos en Towerjazz 180 nm. Se ha desarrollado una Unidad de Trigger Lógica para la toma de datos usando un telescopio para haces de partículas, con el objetivo de aportar mayor control, flexibilidad y reducción de costes. Adicional-

mente se ha desarrollado e implementado el entorno de análisis de la resistencia a la radiación de las memorias de tecnología de Towerjazz 180 nm para el chip SEU_TJ180.

Telescopio de MALTA

La medida de la eficiencia de la colección de carga de Píxel suele llevarse a cabo mediante el uso de telescopios para haces de partículas. Recientemente se ha desarrollado un telescopio para haces de partículas utilizando sensores de MALTA en los planos que lo componen. Las trazas que siguen las partículas cargadas se reconstruyen a partir de las señales depositadas en los planos, que permiten evaluar la capacidad de detección de un sensor bajo test (DUT) que se pone en el centro del telescopio.

Unidad de Trigger Lógica

Se ha desarrollado una Unidad Lógica de Trigger (TLU) para el nuevo telescopio. La TLU es responsable de sincronizar el funcionamiento de los elementos del telescopio para la adquisición y guardado de datos. Cuando un plano detecta el paso de una partícula envía una señal la TLU, ésta procesa las señales de todos los planos y las combina según su configuración para decidir si generar una señal aceptada (L1A) de paso de partícula.

La motivación para el desarrollo de una nueva TLU es reemplazar la unidad previa basada en obsoleta tecnología NIM. Su configuración se realiza mediante combinaciones de conexiones entre los módulos con distintas funciones alojados en una crate que forman la TLU. Se pretende reemplazar debido a su alto coste, poca flexibilidad, alta complejidad de operación y dificultad de transporte.

La TLU de MALTA, mostrada en la Figura 4, está basada en un dispositivo programable de puertas lógicas (FPGA). El uso de esta tecnología permite reducir los costes, el peso, facilitando al mismo tiempo su operación y flexibilidad. La conexión con los planos se realiza mediante dos conectores FMC, uno de entrada y otro de salida.

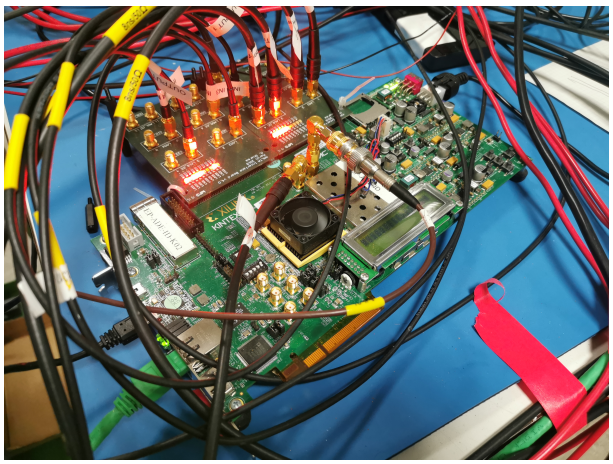

Figura 4: TLU de MALTA en funcionamiento

La combinación de las señales se realiza en la FPGA programada con el firmware diseñado para la TLU. El control de la unidad está centralizado en una interfaz gráfica que permite la configuración de combinaciones, operar el telescopio y monitorizar la toma de datos. La Figura 5 muestra la interfaz gráfica de la TLU. El entorno de software facilita la comunicación entre la TLU y su interfaz, a través de Ethernet utilizando el protocolo de IPbus.

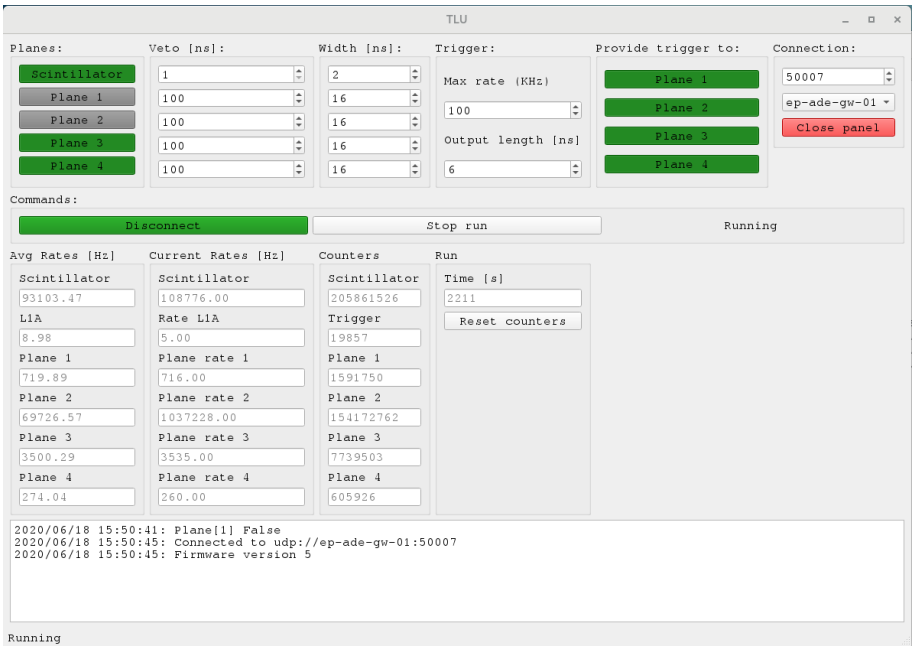

Figura 5: Interfaz gráfica de usuario de la TLU del telescopio de MALTA

La TLU de MALTA ofrece flexibilidad de configuración de forma remota lo que reduce las interrupciones en la toma de datos evitando la necesidad de entrar en el área de irradiación. Ha sido utilizada para la toma de datos en los beam tests de DESY y SPS. En la investigación se llega a la conclusión de que es posible adaptarla a otros sistemas.

SEU_TJ180

Se ha preparado el banco de pruebas para el estudio de la resistencia a la radiación de las memorias utilizadas por la familia de sensores de MALTA mediante el uso del chip SEU_TJ180. La metodología consiste en la escritura y lectura continuada de las memorias durante la irradiación en un haz de iones pesados para establecer la sección eficaz de un SEU. Se ha diseñado y fabricado una PCB para la operación y alimentación del chip. Se conecta mediante FMC a una FPGA Kintex KC705 para su control y lectura. Un firmware ha sido desarrollado en VHDL para controlar el chip desde la FPGA y un entorno de software ha sido preparado para operar y alimentar el chip a través de fuentes de alimentación, ejecutar los tests de forma automatizada y tomar los datos.

Detección de fugas de agua

El riesgo en la infraestructura de ATLAS debido a fugas de agua es uno de los más importantes. Pequeñas cantidades de agua pueden afectar a la electrónica de manera irreparable y grandes fugas son poco probables, pero pueden tener un gran impacto. El sistema actual de detección de agua está basado en sensores de cable Raytech (anteriormente TraceTek) T3000 cuya resistencia varía en la presencia de líquidos y módulos de lectura TTC-1 encargados de medir la resistencia de los cables y proporcionar una respuesta binaria. Esta solución implica grandes costes para cubrir grandes áreas, tiene un gran desgaste en el tiempo y no han resultado una solución fiable.

Se ha desarrollado una nueva solución para la infraestructura de ATLAS con el nombre de RELIANCE (Reliable Liquid Detection for Critical Environments). Después de un proceso de búsqueda para un nuevo sistema de detección, el candidato elegido es un material basado en nano-tubos de carbono (CNTs) desarrollado por la Universidad de Washington (USA) llamado Smart Paper. Se trata de un material conductivo parecido al papel, cuyas propiedades conductivas cambian en presencia de agua

gracias a los cambios mecánicos en la estructura de las fibras del papel que incluyen los CNTs. A diferencia del papel corriente, que aumenta su conductividad en función de la cantidad de agua absorbida por el papel, y depende de la cantidad de iones disueltos en el agua para mejorar su conductividad, el Smart Paper, reduce su conductividad eléctrica en función de la cantidad de agua absorbida, porque su principal mecanismo es la separación de la red de nanotubos conductores.

Para la detección de agua el factor tenido en cuenta es la diferencia entre la resistencia en seco R_{dry} y la resistencia en húmedo R_{wet}, expresada como $\Delta R = R_{wet} - R_{dry}$. La Figura 6 muestra en la parte izquierda una foto de una hoja de Smart Paper. En la derecha se observa la ΔR > 2kΩ producida por 4 ml de agua.

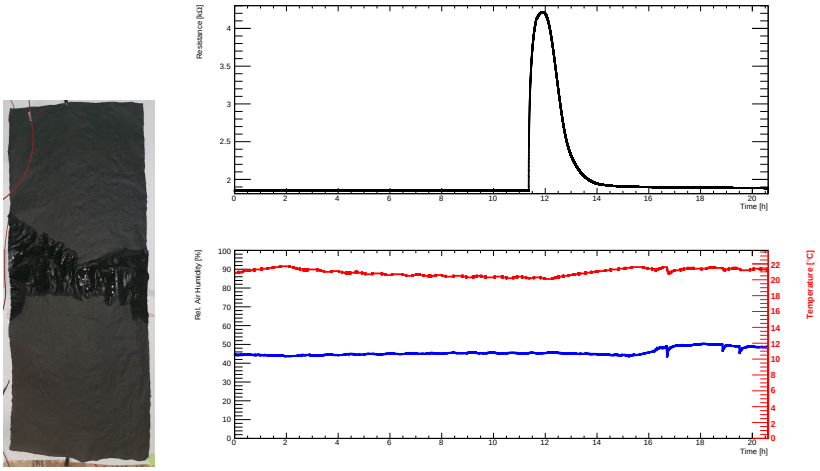

Figura 6: Izquierda: Smart Paper de 75×30 cm con la parte central humedecida con 4 ml de agua. Derecha superior: resistencia en función del tiempo. Derecha inferior: temperatura y humedad en función del tiempo

Dada la composición del Smart Paper, ésta es intrínsecamente susceptible a la humedad, temperatura, deformación mecánica y contacto con superficies conductivas. El Smart Paper ha sido caracterizado para diferenciar la presencia de agua de otros factores. A pesar de que el papel se ve influenciado por la temperatura y la humedad no ha sido posible establecer una correlación. La parte izquierda de la Figura 7 muestra la correlación negativa entre la resistencia y el tamaño del papel. La parte derecha muestra la ΔR en función del tamaño pudiendo observar una ΔR > 0.2 kΩ en los papeles más grandes.

La Figura 8 nos permite medir el mínimo volumen de agua necesario para conseguir

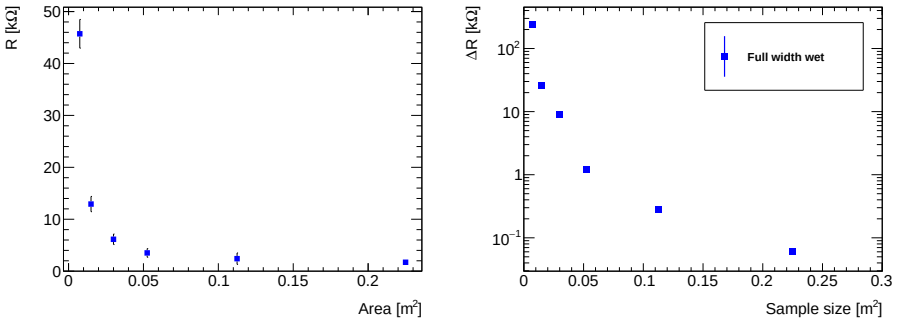

Figura 7: Izquierda: Resistencia en función del tamaño del papel en seco. Derecha: ΔR en función del tamaño del papel en tests con 0.5 ml de agua.

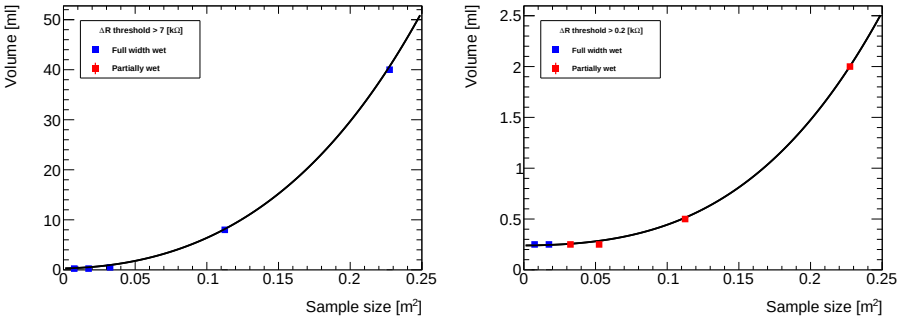

Figura 8: Volumen de agua en función del tamaño del papel para una respuesta mínima de ΔR > 6 kΩ (izquierda) y ΔR > 0.2 kΩ (derecha).

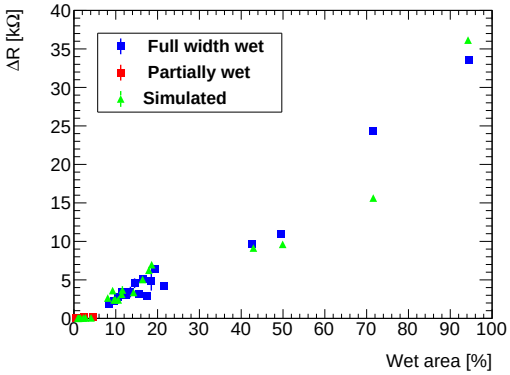

Figura 9: ΔR en función del porcentaje de área húmeda. Modelo eléctrico en verde y reales en azul y rojo. Los tests corresponden a papeles de 0.225 m^2 y vertidos de agua entre 0.5 ml y 16 ml.

un ΔR > 6 kΩ (izquierda) y ΔR > 0.2 kΩ. Un importante fenómeno observado durante la caracterización del papel es el salto en la respuesta cuando existe línea húmeda

cubriendo el total del ancho en el papel.

En la Figura 9 se puede observar una clara dependencia lineal entre ΔR y la superficie mojada. Los puntos en verde son producto de un modelo funcional de conductividad eléctrica propuesto para el Smart Paper. El modelo divide el papel en una matriz de $M \times N$ celdas resistivas donde el cambio de cada una de ellas afecta al resto.

Se ha desarrollado un sistema de lectura (*read-out*) para el leer el Smart Paper, llamado *RELIANCE box*, tiene como requerimientos poder monitorizar los sensores en las cavernas, analizar la señal para descartar falsos positivos y comunicarse con DCS para su configuración y propagación de alarmas. La Figura 10 muestra el sistema de detección (*read-out*) llamado *RELIANCE box*, basado en un Raspberry Pi 4 conectado a un ADC a través de una PCB hecha a medida. El papel se conecta al sistema a través de unas pinzas dentadas y la señal es filtrada en los módulos de la PCB antes de ser leída por el ADC. El objetivo de los filtros es reducir el impacto del ruido electromagnético en la señal.

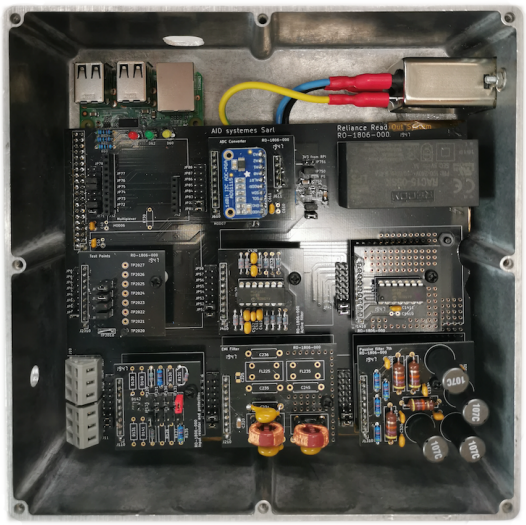

Figura 10: *RELIANCE box* version 2

Un entorno de software opera el sistema en tiempo real. Se ha desarrollado como una librería en C++ compilada siguiendo las herramientas estándar de ATLAS. Tiene como funciones principales la lectura del ADC, conversión de sus valores en base a las constantes de calibración, detección de alarmas y propagación del estado.

Adicionalmente se ha desarrollado un algoritmo embebido en el software llamado *Chasing Averages* cuyo propósito es diferenciar fluctuaciones debidas a factores

ambientales de una rápida evolución de la señal debida al contacto con el agua. El algoritmo, basado en el cálculo de la ratio entre la media de los primeros m valores y la media de los siguientes n valores, se expresa como

$$\frac{\overline{R_m}}{\overline{R_n}} = \frac{\frac{1}{m}\sum_{i=0}^{m} R_i}{\frac{1}{m}\sum_{i=0}^{m+n} R_i} \tag{1}$$

siendo el último índice de $\overline{Rm}$ el valor más reciente y el primer índice de $\overline{Rn}$ el más antiguo. La Figura 11 muestra una medición con distintos valores en los dos parámetros del algoritmo m y n.

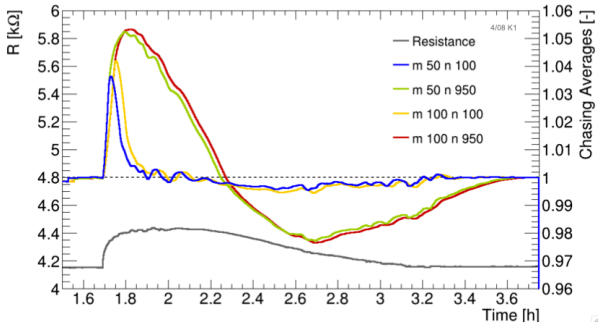

Figura 11: Medición de un Smart Paper de 75×30 cm^2 con 0.5 ml de agua utilizando el algoritmo *Chasing Averages*.

La supervisión de *RELIANCE box* se ha desarrollado como un servidor OPC Unified Architecture (OPC-UA) utilizando el entorno Quasar para facilitar su integración en DCS. El software online ejecutado en el *RELIANCE box* se ha desarrollado como una máquina de estados siguiendo la convención establecida para para DCS.

Conclusiones

La presente tesis doctoral investiga y desarrolla nuevas soluciones para la seguridad del detector, el conocimiento de la infraestructura y su control. Los desarrollos reducen el impacto de las operaciones del detector y costes en la toma de datos para el Run 4, durante el tiempo de operación y de mantenimiento.

Se ha implementado un Sistema Experto para ATLAS que ofrece a sus usuarios una simulación fiable de la infraestructura de ATLAS, permitiendo la planificación de intervenciones reduciendo sus riesgos y la obtención de información de gran parte

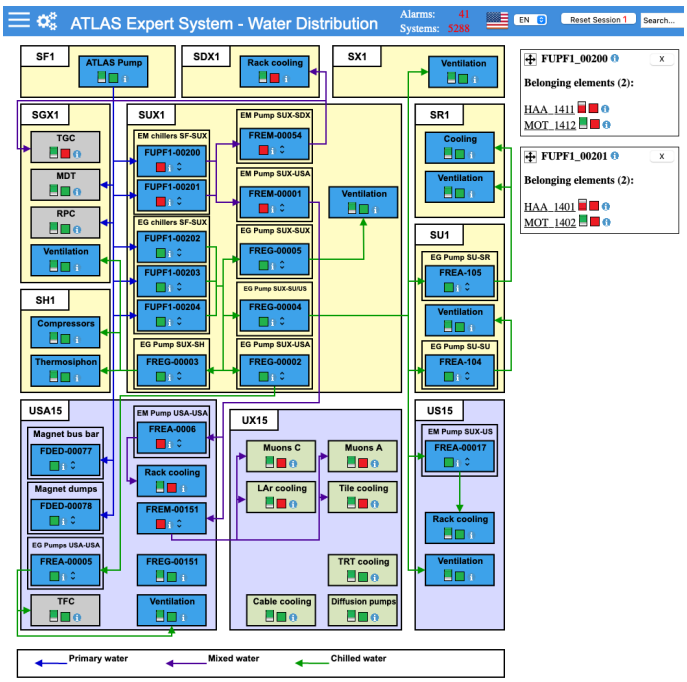

Figura 12: Distribución de agua en el Expert System durante la simulación del mantenimiento anual de agua fría.

de sus sistemas y el diagnóstico de posibles causas de situaciones inesperadas. Está siendo utilizado por expertos de la infraestructura y en la sala de control en ATLAS. Los resultados muestran un alto grado de concordancia entre sus predicciones y el resultado de las intervenciones y eventos. Como ejemplo se propone la intervención anual de mantenimiento de las unidades de refrigeración, mostrada en la Figura 12, debido a que es una intervención anual cuyo impacto puede ser subestimado. En la parte derecha de la Figura se muestran dos grupos desplegados, FUPF1-00200 y FUPF1-00201 con sistemas apagados. En la barra azul superior se indica que 41 alarmas y 5288 sistemas han sido afectados. En la parte de la izquierda es visible el impacto de la intervención en la refrigeración de los racks en SDX1 (superficie) y USA15 (subterránea), estaciones de refrigeración de muones C y A así como LAr y Tile. La Figura 13 muestra el resultado detallado de la simulación. En la parte superior se pueden ver los comandos que han iniciado la simulación, en la parte central hay paneles que muestran el estado de DSS y en la parte inferior el resto de sistemas afectados.

Se puede mejorar la seguridad frente a fugas de agua mediante el sistema implementado para ATLAS. El sistema se basa en un sensor de celulosa y nanotubos de

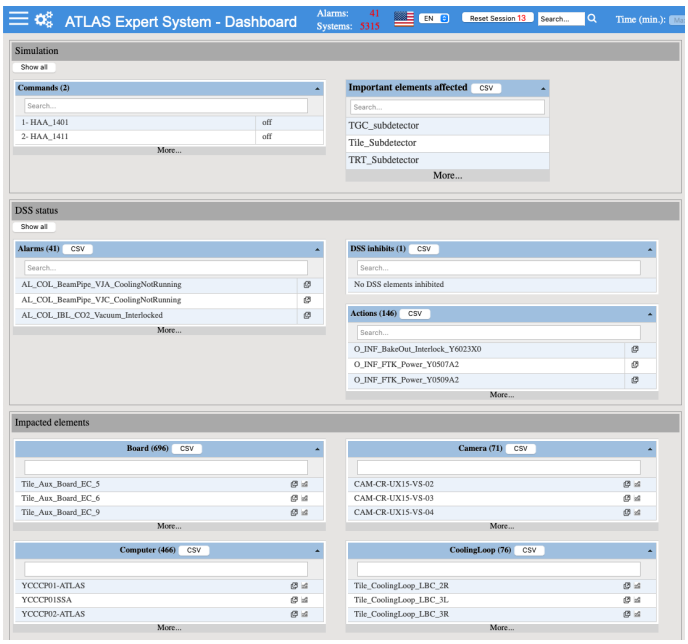

Figura 13: La página *Dashboard* muestra el resultado detallado de la simulación

carbono que puede ser fabricado de forma industrial y un sistema de adquisición de datos embebido e integrado en DCS. El sistema está actualmente en fase de pruebas en la caverna de servicios de ATLAS y permite la detección de fugas de agua a partir de unas pocas gotas en grandes superficies con un tiempo de reacción inferior al minuto. La Figura 14 muestra el panel de DCS de un *RELIANCE box* en la caverna USA15 de ATLAS.

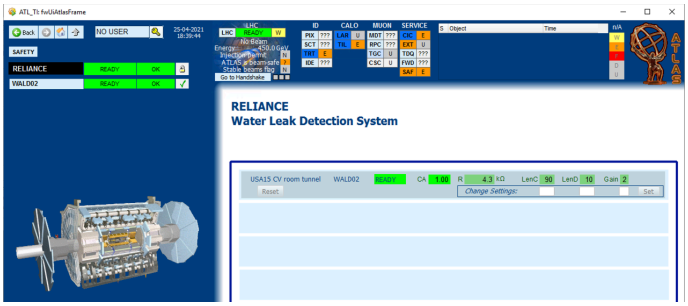

Figura 14: Panel de RELIANCE en DCS.

El sensor tiene el potencial para convertirse en un nuevo estándar para la tecnología de detección de agua dada su sensibilidad e indisolubilidad en agua. A pesar de los retos actuales que presenta la tecnología, entre los que se encuentran la conectividad

del sistema de lectura con procesos industriales y el despliegue en las cavernas de ATLAS, el sistema podrá monitorizar el desarrollo de una fuga de agua y proteger el costoso equipamiento con mayor cobertura que la tecnología anterior.

Se ha demostrado que el uso de FPGAs para tareas de toma de datos mejora la eficiencia de toma de datos y reduce el tiempo necesario para ajustar configuraciones distintas, mediante el desarrollo de una Unidad de Trigger Lógica para el telescopio de haces de partículas en el marco de la caracterización de detectores de Píxel. La unidad permite la operación del telescopio para haces de partículas y ha servido para reemplazar la tecnología anterior y mejorar su rendimiento y flexibilidad de uso. La Figura 15 muestra la toma de datos con el telescopio utilizando dos planos y un DUT.

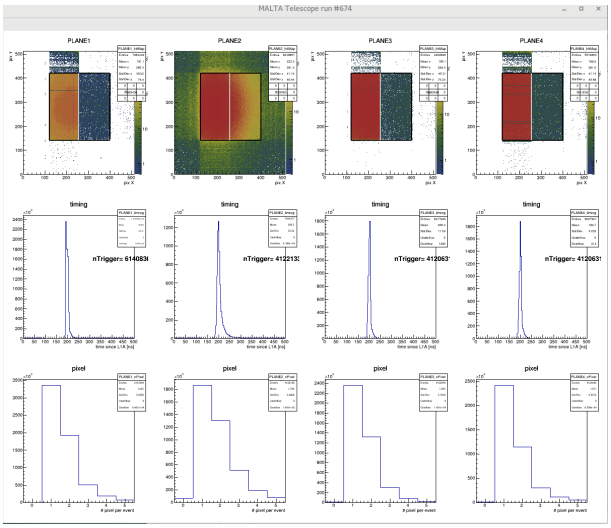

Figura 15: Captura de la toma de datos del telescopio utilizando la TLU de MALTA

Los beneficios obtenidos son muchos, una electrónica más ligera y de menor coste, mayor flexibilidad en la configuración y uso, así como menor número de interrupciones durante la operación del telescopio debido a las capacidades remotas de las FPGAs. La TLU de MALTA basada en una FPGA ha demostrado su capacidad durante las campañas de tests con haces de partículas con resultados que se ajustan a los requerimientos para el telescopio.

Igualmente se ha desarrollado el entorno de caracterización del SEU_TJ180 chip para evaluar la resistencia de la tecnología de las memorias de Towejazz 180 nm. La Figura 16 muestra en la izquierda la PCB y en la derecha la PCB conectada a la FPGA en el soporte de protección para la irradiación. El sistema permite ejecutar tests

de forma rápida desde la FPGA lo que permite tener una respuesta inmediata de los resultados durante el tiempo del haz que suele ser reducido de alto coste.

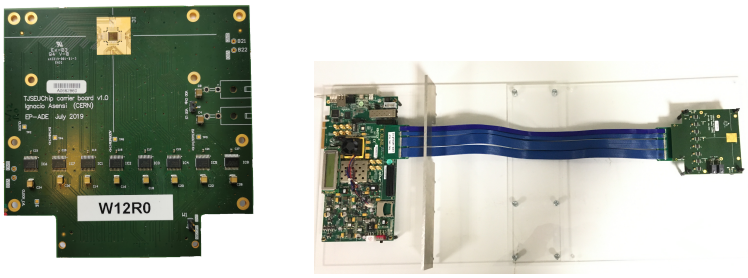

Figura 16: Izquierda: PCB de soporte para el SEU_TJ180. Derecha: PCB conectada a la FPGA montada en el soporte.

Con todo lo explicado en el resumen, quedan abordadas las hipótesis planteadas, en los sucesivos capítulos se demostrarán las mismas para alcanzar la tesis final.

Abstract

The LHC at CERN is the largest particle accelerator in the world. It is preparing to run from 2022 to 2025 after which it will undergo an upgrade to become the High Luminosity LHC that is scheduled to start in the middle of 2027. The instantaneous luminosity will go from the previous 2.1×10^{34} $cm^{-2}s^{-1}$ up to 7.5×10^{34} $cm^{-2}s^{-1}$ and deliver a total integrated luminosity expected of 3000 fb^{-1} by the end of its lifetime. This represents a great challenge in terms of radiation hardness that requires research, development and improvements in many areas such as electronics and safety.

The ATLAS infrastructure requires vast amounts of knowledge in many areas in order to plan interventions or to react properly to unexpected events during operation and maintenance. A main contribution of this research to the safety of ATLAS has been the development of an ATLAS Expert System, a knowledge-base mean that contains an overall representation of the experiment's infrastructure systems and their inter-dependencies in the way they function. This tool is currently being used by Technical Coordination and the sub-detectors teams to prepare interventions, understand their risks in all the infrastructure and analyse events in the ATLAS control room. In an effort to improve the safety infrastructure, a new water leak detection system has been developed based on a novel sensing technique, that improves the precision and reliability of the safety system. The system has been tested as a prototype in the service cavern of ATLAS and will be commissioned for operation during Run 3.

In the context of the characterization of monolithic Pixel detectors, a Trigger Logic Unit has been developed for a new beam telescope. It has been used in the test-beam campaigns during LS2, and it has improved the operation procedures of the telescope. It provides a more flexible interface while preserving the functionalities and performance of the previous technology based on NIM electronics. Also, a test framework has been designed and produced for the study of the radiation effects in the memory

cells technology used in the MALTA family.

Keywords: LHC, ATLAS, CMOS, leak detection, expert system, beam telescope, SEU, radiation hardness

Acknowledgements

First, I would like to thank the CERN Doctoral Programme and Dr. Ludovico Pontecorvo as well as the Escola Tècnica Superior D'Enginyeria of Valencia for the trust and the founding of this doctorate; and specially for the great opportunity that has been to participate in the ATLAS experiment.

I would like to express my gratitude to Dr. Carlos Solans for being my mentor and for his supervision at CERN, which has gone far beyond the academic mission. For his advice, teachings and the constant encouragement that have made the submission of this thesis possible. I am indebted for his trust and opportunities he provided on my career. And I would like also to extend my gratitude to Prof. José Torres from the University of Valencia, for all his trust and help; and all his advice during the supervision of my PhD.

I would like to thank all my friends and colleagues at the ATLAS ITk Pixel group, with whom I had the opportunity to share the last three years: Heinz Pernegger, Valerio Dao, Abhishek Sharma, Andrea Gabrielli, Leyre Flores, Florian Dachs, Lingxin Meng, Roberto Cardella, Patrick Freeman, Mateusz Dyndal, Francesco Piro, Enrico Schioppa, Cesar Augusto Marin, Susanne Kuehn and Milou Van Rijnbach. I want to give a special thanks to Valerio, for his crucial help and patience to answer all my questions and always being accessible regardless of the time.

I would like also to thank the friends and colleagues in ATLAS, with whom I have shared work and many experiences all this time. I want to thank Andre Rummler for his help and support in the ATLAS operations and for his many new ideas and contributions to the results presented in this thesis. I want also to thank Florian Haslbeck for all his dedication and the interesting conversations and fun times. I would like also to thank Gustavo Uribe, Nicolas Fischer and Kaan Yuksel for their help in ATLAS.

I would like to thank my colleagues from outside CERN, Anthony Dichiara and

Sheila Goodman from the University of Washington, for making this collaboration possible and for the amazing work. And also many thanks to all the people who helped me in my early steps in the research world. It has truly been an invaluable experience working and sharing great times with all of you.

I would like also to express my greatest thanks to my wife, Liz Arnanz, for all her love, support and her immense patience and understanding during the hard time of this PhD. También me gustaría agradecer a mis amigos en Ginebra y Valencia por su apoyo y momentos de distracción que tanto me han ayudado. Finalmente, me gustaría agradecer a toda mi familia por su incondicional apoyo y cariño, así como por la educación y oportunidades que me han dado siempre. A vosotros os dedico este trabajo.

Chapter 1

Introduction

1.1 Research context and motivation

The Large Hadron Collider (LHC) at CERN is the largest particle accelerator in the world. I was built by CERN (*CERN Conseil Europeén pour la Recherche Nucléaire*) between 1998 and 2008 in Geneva, Switzerland. It will undergo an upgrade to become the High Luminosity LHC (HL-LHC) that will start in the middle of 2027.

ATLAS (A Toroidal LHC AparatuS) is a multi-purpose detector, the largest of the four main experiments located at the LHC. Its construction started in 2003 and started its operations in 2008. It is a complex infrastructure based in a experimental cavern where the detector is located and two services caverns. ATLAS consists of sub-detectors and a infrastructure including electronic systems, magnets, gas distribution, cryogenics and cooling. The behaviour of the infrastructure is difficult to predict due to the high level of inter-dependencies among the systems. This thesis is divided in two parts, the first part is related to the safety and operation of the infrastructure and the second part is related to the control and data acquisition systems.

The first part of this thesis is focused on the safety and operation of the infrastructure. The aging of the systems increases the risk in the main cooling systems and those nearby electronics. This implies the risk of major flooding and damages in electronic equipment that is difficult to replace. Conventional water detection systems are based in limited range sensors that can only target the surface contiguous to a small sensor. As a consequence, a research has been carried out to find new materials that ensure a

large targeted surface at a reduced cost. The results showed interesting water sensing capabilities for carbon nanotube based papers. Additionally, the knowledge base on the infrastructure, which has been under constant changes and upgrades has become a growing concern to the experts for its correct functioning and operations.

This thesis arises two hypothesis relative to the infrastructure safety of ATLAS: Can the safety of the detector be improved by the usage of new sensors? Could an expert system provide better knowledge base enhancing the safety procedures during operations and maintenance of the ATLAS infrastructure?

The second part of this thesis is focused on the control and data acquisition systems used for the Pixel sensor characterization. The monolithic Pixel sensors show great potential for high energy physics, nevertheless they are still limited by the radiation hardness and the complexity of operation in experiments such as ATLAS. There is a need for improvement in modularity, adaptability and flexibility to characterize the monolithic Pixel detectors. Previously used characterization systems used oscilloscope and dedicated systems. The usage of FPGAs can provide higher precision and speed in the data acquisition at a lower cost and more scalability than with the previous technologies.

In this context, this thesis considers the following hypothesis: Can the usage of FPGAs replace the previous technology in the characterization of Pixel sensors?

1.2 Objectives

In the context of the motivations and research previously mentioned, the general objective of this doctoral thesis is the following:

The research and development of new solutions to improve the safety of the detector against water leaks and the control of Pixel systems in R&D state for ATLAS. Reducing the impact in detector operations and costs in the data taking for Run 3, during the operation and maintenance.

The following specific objectives are proposed for the research of the previously formulated hypothesis:

1. Design and development of an Expert System for ATLAS. The system has to emulate the reasoning of experts and being able to understand questions and provide answers. For this, the knowledge base has to be gathered with detailed

information about critic parts of the detector and safety systems, gas distribution, cooling, cryogenics, magnets and electricity. Also, an inference logic system has to be designed in order to interpret the knowledge base and produce simulations. And finally, an interface is necessary to show the behaviour of ATLAS in a comprehensive manner, responding to the scenarios that are suggested to the system.

2. Design and development of system to detect and react to water leaks. It aims to replace the current technology for the Run 3 supervision systems of ATLAS. The new systems has to actively reduce the risk of damage from water leaks in the cooling circuits and being able to target large surface with high sensitivity and quick response time at a low cost.

3. Demonstrate the flexibility of FPGAs for the characterization of Pixel monolithic sensors by designing and constructing a Trigger Logic Unit for the data acquisition with a beam telescope. The new unit has to bring more control, flexibility and cost reduction. Additionally, an analysis environment for the radiation hardness has to be implemented to test the memories for the TowerJazz 180 nm technology.

1.3 Methodology and structure

This doctoral thesis is based on the research work carried out in the experiment of ATLAS at CERN, in the frame of the collaboration between the CERN EP-ADE group and the University of Valencia, as a member of the EP-ADE group. The following chapters aim to reach the objectives previously enumerated.

Chapter 2 is a brief introduction to the LHC and more particularly to the ATLAS experiment and its sub-detectors. It also outlines the more relevant systems for this thesis, Detector Safety System and Detector Control System. Its content is based on references mentioned.

Chapter 3 is dedicated to the development of the ATLAS Expert System. It describes the project and its motivation in the context of the developments in safety and operations of ATLAS Technical Coordination. It also describes the architecture and user interface as well as it provides examples of its usage and reliability. Parts of the Chapter 3 has been presented by the author as main contributor in CHEP 2018,

ICALEPCS 2019 and VCHEP 2021. It has also been selected for the Early-Career-Scientists Session at the ATLAS Week of October 2020. The author has been responsible for the original concept, the technical implementation, operations and outreach.

Chapter 4 consists of a brief description of the Pixel detector technology and a contextualization of the author's contribution with the ATLAS CMOS community through the characterization of the MALTA CMOS sensor. The author has participated in beam test activities and the development of software and performance tools.

Chapter 5 focuses on the work carried out by the author in two projects. The development of a new Trigger Logic Unit for the MALTA characterization in the beam tests. The author has been responsible for the main idea, the execution, procurement, performance testing and operations. The second consists of measuring the tolerance of the current technology to radiation effects. The author has been responsible for the main idea, execution, procurement, PCB design, manufacturing and hardware testing. Part of the Chapter 5 has been presented by in VERTEX 2020 and the 7th Beam Telescopes and Test Beams Workshop 2019.

Chapter 6 describes the project of developing a new leak detection system, the selection and characterization of the detectors, the monitoring system and its results and integration in the ATLAS Detector Control System. The author has been responsible for the main idea, execution, procurement, characterization of materials and the testing of software and hardware.

Chapter 2

The ATLAS experiment at the LHC

2.1 CERN and the LHC

CERN is the European Laboratory of Particle Physics. It is run by 23 Member States and other countries which are also involved in different ways. Employing around 2500 people, CERN facilities are also used by many scientists and universities from around the world. There are also around 8000 visiting scientists, half of the world's particle physicists, that come to CERN for their research. They represent 580 universities and 85 nationalities.

The list of achievements attributed to CERN is extensive, the Gargamelle chamber experiment in 1973 concluded with the discovery of the weak neutral currents, the discovery in 1983 with the experiments UA1 and UA2 of $W^{\pm}$ and Z particles, and in 2012 attracting much media attention the long awaited validation of the Standard Model with the proof of the existence of the Higgs Boson.

The Large Hadron Collider (LHC) is currently the main part of CERN's accelerator complex, as shown in Fig. 2.1. The LHC is the world's largest and most powerful particle accelerator with a circumference of 27 km at around 80 m depth across the border between Switzerland and France. Two particle beams collide heads on with each other at a center-of-mass energy of $\sqrt{s}$ = 13 TeV.

There are four large experiments in the LHC ring. ATLAS (A Toroidal LHC Ap-

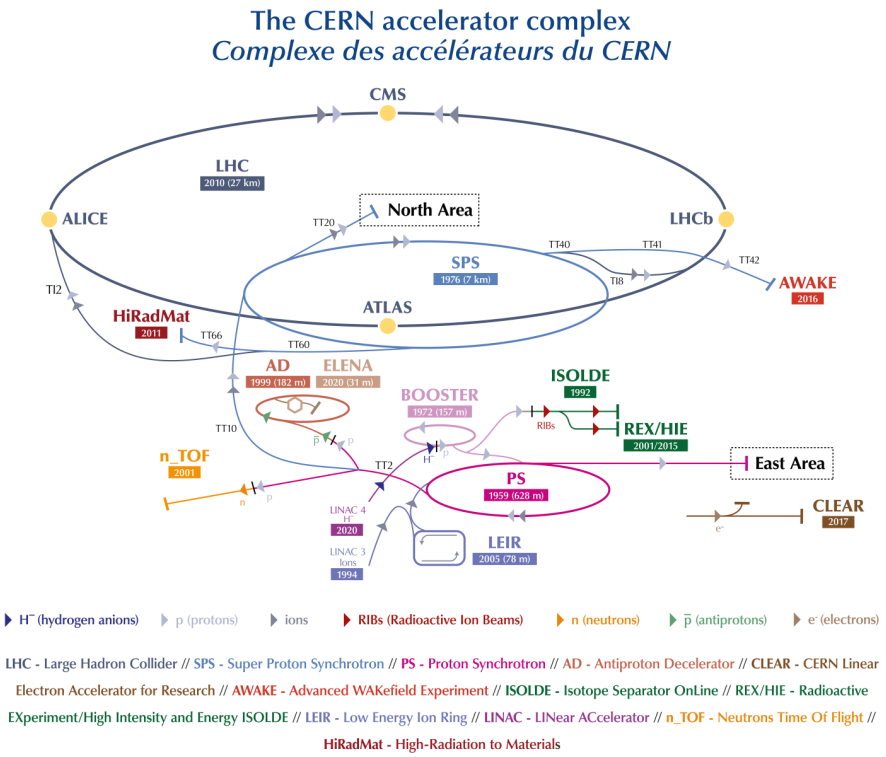

Figure 2.1: The CERN accelerator complex in 2019.

paratus) [1] and CMS (Compact Muon Solenoid) [2], are general-purpose experiments optimized to study new physics at the TeV scale. LHCb (Large Hadron Collider beauty) [3] is focused on the investigation of the CP violation on the bottom quark sector and ALICE (A Large Ion Collider Experiment) [4] on the study of quark-gluon plasma through Pb-Pb collisions.

2.2 The ATLAS experiment

The ATLAS experiment is a general-purpose detector designed to exploit the full potential of the LHC improving measurements of the Standard Model. It has cylindrical shape with 44 meters length and more than 25 meters height and an overall weight of approximately 7000 tonnes. It is divided into sub-detectors as show in Fig. 2.2. The Inner Detector represents the inner most part of ATLAS, surrounded by a solenoid magnet, the Calorimeters, the Muon system and the large superconducting air-core toroid

magnets.

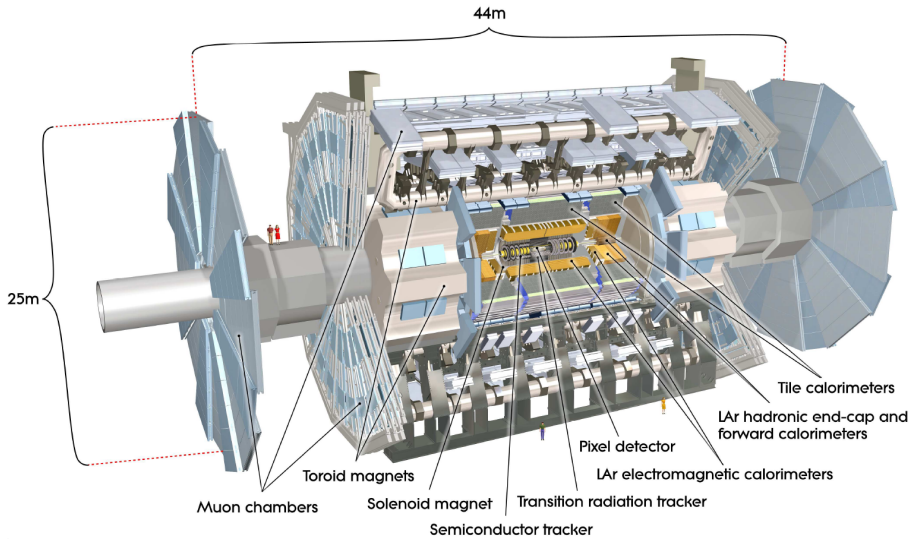

Figure 2.2: The ATLAS experiment and sub-detectors drawing.

Basic design criteria of the detector include a very good electromagnetic calorimetry for electron and photon identification and measurements and full-coverage hadronic calorimetry for accurate jet and missing transverse energy (E_T^{miss}) measurements. High-precision muon measurements. Efficient tracking at high luminosity for high p_T lepton-momentum measurements, electron and photon identification, τ-lepton and heavy-flavour identification, and full event reconstruction capability at lower luminosity. The pseudo-rapidity is defined as $\eta = -\ln(\tan(\theta/2))$ with η being the polar angle with respect to the beam direction. The other relevant coordinate of the detector is ϕ, which is the azimuthal angle measured upwards from the direction to the center of the LHC ring. ATLAS provides high efficiencies for most physics processes of interest at LHC by triggering and measurements of particles at low p_T thresholds.

2.2.1 The Inner Detector

Fig. 2.3 shows a drawing of the Inner Detector, a 7 m long cylinder composed of four systems. It is designed to reconstruct tracks and decay vertices in any event with high efficiency. It contributes to electron, photon and muon identification, using additional information from the calorimeter and muon systems. It supplies extra signatures for short-lived particle decay vertices.

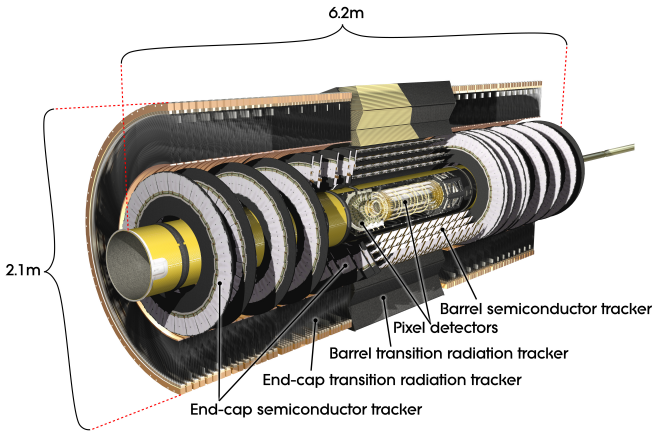

Figure 2.3: Inner detector drawing.

The Insertable Barrel Layer

The Insertable Barrel Layer (IBL) is the first layer of the pixel detector installed during LS1, at 3.3 cm from the beam axis. It is composed of 14 staves loaded with 20 50×150 μm^2 pitch pixel detectors. Each module has more than 20000 channels.

The Pixel detector

The Pixel detector is composed of 3 barrels at 5, 8, 12 cm away from the beam line, and 3 discs on each side at 45, 55, 66 cm from the interaction point, totaling 1.9 Million channels of size 50×400 μm^2, covering an active area around the beam pipe of 1.73 m^2.

The Silicon Semiconductor Tracker

The Silicon Semiconductor Tracker (SCT) detector uses small angle (40 mrad) stereo strips for the measurement of both coordinates, with one set of strips in each layer measuring ϕ. The pixel detector is much more radiation tolerant than the silicon strip tracker. The number of layers of the semiconductor detectors must be limited due to the amount of material they introduce and their high cost.

The Transition Radiation Tracker

The Transition Radiation Tracker (TRT) provides a larger number of tracking points, approximately 351000, with lower precision. It provides tracking with much less material per point and a lower cost. The barrel TRT tubes are parallel to the beam direction.

2.2.2 Calorimeters

Fig. 2.4 shows a representation of all the calorimeters of ATLAS, which cover the range of $|\eta| < 4.9$.

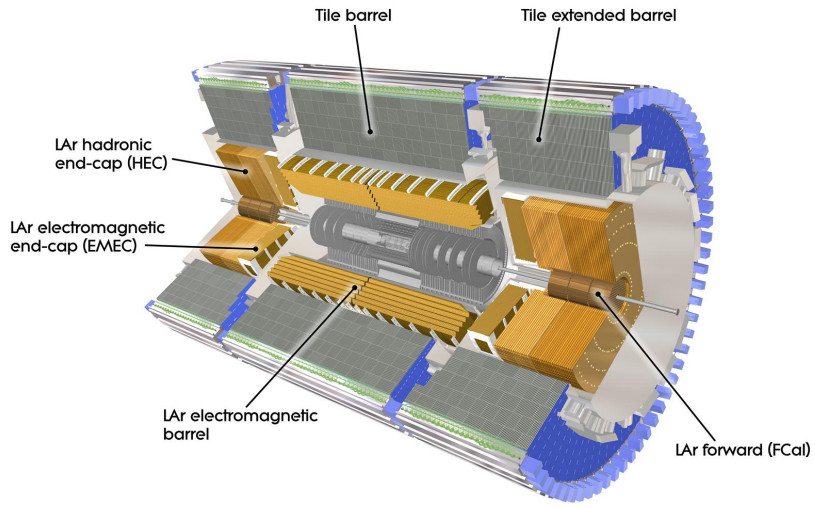

Figure 2.4: Layout of the ATLAS calorimeters.

The EM calorimeter is a Liquid-Argon (LAr) lead detector divided into a barrel and two end cap parts. It uses a calorimeter technique with accordion-shaped Kapton electrodes and lead absorbers, used for all electromagnetic calorimetry covering the pseudo-rapidity interval $|\eta| < 3.2$, and for part of the hadronic calorimetry in the range $1.4 < |\eta| < 4.8$.

The Hadronic Barrel calorimeter (Tile Calorimeter) is based on a sampling technique with plastic scintillator plates (tiles) embedded in a steel absorber. Tile are read-out on both sides by a wavelength shifting fiber, and groups of tiles are bundled together into cells that are read-out by a photo-multiplier tube (PMT). At larger rapidities, where higher radiation resistance is needed, the radiation-hard LAr technology is used for the

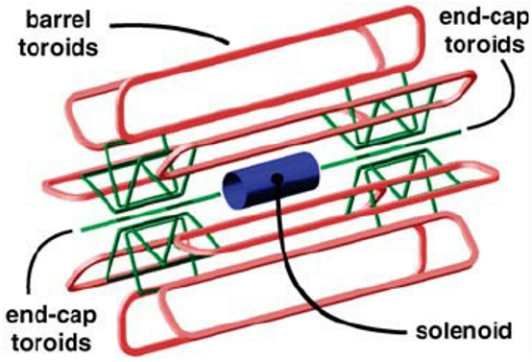

Figure 2.5: ATLAS Magnet systems

Hadronic End-cap Calorimeter (HEC) and the Forward Calorimeter (FCAL).

2.2.3 Magnet System

The ATLAS magnetic field configuration is optimized for particle bending around the various detectors in a light and open structure which minimizes scattering effects. The experiment magnet system arrangement consists of a central solenoid servicing the inner detector trackers with an axial magnetic field of 2 T, and a barrel toroid and two end cap toroids that generate a tangential magnetic field of approximately 0.5 T and 1 T for the muon spectrometer in the barrel and end cap regions respectively. Fig. 2.5 shows the position of the four superconducting magnets within the ATLAS detector.

The central solenoid is designed to provide a 2 T strong magnetic field in the central tracking volume made out of a single layer coil. It shares the cryostat with the Liquid Argon calorimeter and the flux is returned by the steel of the Hadronic calorimeter.

2.2.4 The Muon System

The ATLAS muon spectrometer has been designed to fulfill the following requirements: efficient use of the magnet bending power, pseudo-rapidity coverage of $|\eta| < 3$, and practical chamber dimensions for production, transport and installation. Fig. 2.6 shows the position of the muon chambers. The spectrometer is divided into three regions, barrel region ($|\eta| < 1.05$), transition region ($1.05 < |\eta| < 1.4$) and end-cap region ($|\eta| > 1.4$). Four different technologies depending on the spatial and timing resolution, resistance to radiation and engineering considerations have been used: Monitored

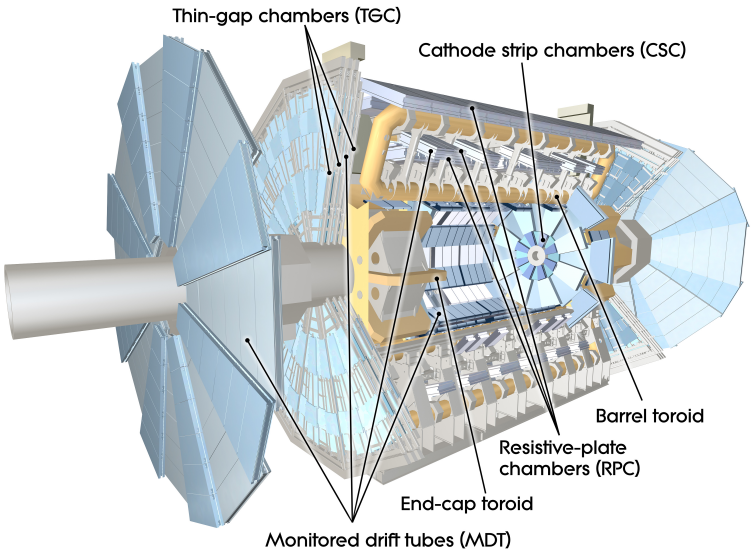

Figure 2.6: ATLAS Muon system

Drift Tube chambers (MDT), Cathode Strip Chambers (CSC), Resistive Plate Chambers (RPC) and Thin Gap Chambers (TGC).

Monitored Drift Tube Chambers

The MDT chambers are composed by multi layers of high-pressure drift tubes. Each multi layer is mounted on each side of the support structure. The drift tubes are made of aluminum, 30 mm of diameter, with a central wire of W-Re. They work at 3 bar absolute pressure with a non-flammable mixture of Ar-CO_2.

Cathode Strip Chambers

The CSCs are multi wire proportional chambers operated with a mixture of Ar-CO_2-CF_4. The distance between anode wires (2.5 mm) equals the distance to the cathode. The cathode readout is segmented into strips (5.08 mm) orthogonal to the anode wires. The precision coordinate is obtained by measuring the induced avalanche in the segmented cathode, achieving space resolutions better than 60 μm.

Resistive Plate Chambers

The RPC is a gaseous parallel-plate detector with a typical space-time resolution of 1 cm $\times$ 1 ns with digital readout. It is composed of two parallel resistive plates made

of Bakelite. The plates are separated by spacers that define the size of the gas gaps. The gas is a mixture of $C_2H_2F_4$. A uniform electric field of a few kV/mm produces the avalanche multiplication of ionization electrons. The signal is readout via capacitive coupling to metal strips placed at both sides of the detector and grounded.

Thin Gap Chambers

A TGC is built with 50 μm wires separated 2 mm. The wires are placed between two graphite cathodes at a distance of 1.6 mm. Behind the graphite cathodes, strips or pads are located to perform a capacitive readout in any desired geometry. Some advantages of these chambers are a fast signal, typical rise time 10 ns and low sensitivity to mechanical deformations.

New Small Wheel

The New Small Wheel (NSW) is under construction, installation and commissioning during LS2. It is composed of 16 sectors equipped with a Micro-megas for tracking and a sTGC chamber for triggering. The NSW will replace the current small wheel composed of CSC and TGC chambers.

2.3 Services

The ATLAS service buildings are shown in shown in Fig. 2.7 of the LHC. They are located in the area called Point 1, and they are split in surface and underground buildings. The surface buildings provide electricity (SE1), cooling (SF1, SUX1), ventilation (SU1), gas (SGX1), cryogenics (SH1), to the underground buildings that host the detector, the mono-phase detector cooling stations, and the proximity cryogenics (UX15), back-end electronics crates (USA15, US15), and access galleries (ULX15, ULX16). Table 2.1 lists ATLAS buildings.

2.3.1 Electricity

Electricity to operate CERN is provided by the French power grid. In cases of service interruption, CERN can switch to the Swiss power network with reduced capacity. The total power used by CERN is 140 MW, from which 70 MW is used up by the LHC and its experiments, ATLAS is approximately 10 MW. This is distributed from the 66

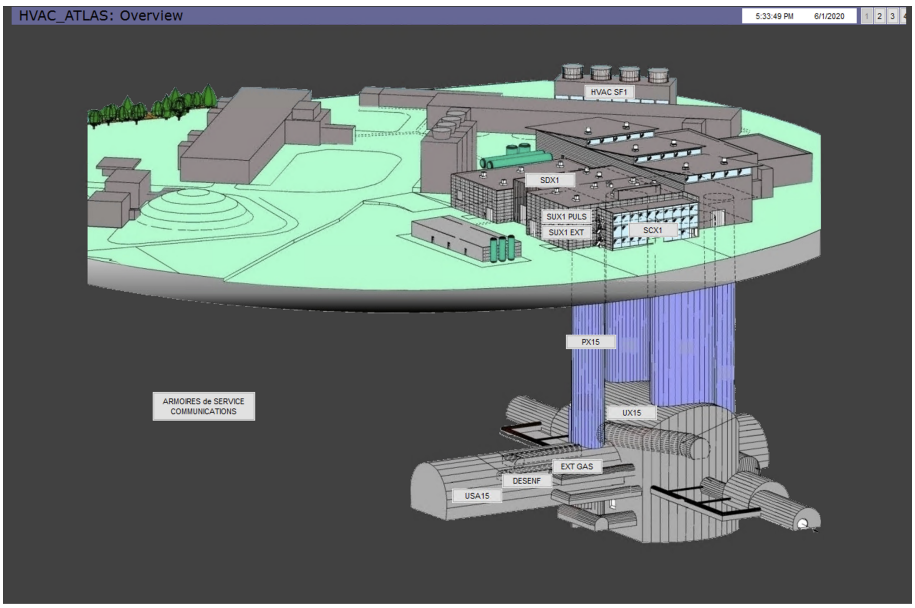

Figure 2.7: LHC Point 1 site.

Building	Services
SDX1	Surface computing facility, UPS batteries
SUX1	Surface chilled and mixed water production
SGX1	Surface gas storage and pumps
SH1	Primary cryogenics and dry air production
SF1	Primary cooling towers
SR1	Surface assembly site
SX1	Surface access to UX15, UPS batteries
USA15	Underground cavern. Back-end electronics, pumps, and transformers
US15	Underground cavern. Back-end electronics crates
UX15	Experimental cavern. Detector front-end, and front-end cooling stations

Table 2.1: ATLAS detector and infrastructure buildings.

kW supply for ATLAS Point 1, to several transformers that regulate the power down to 18 kW at the surface of Point 1. Second power transformers are located in the surface ATLAS buildings, and regulate down to 400 V. A grid of switchboards distribute the power to the surface equipment in SDX1, SUX1, SX1, and to the underground buildings USA15, US15, and UX15. The ATLAS electrical network has 3 different flavours. Regular power backed up by a 10 minute UPS. UPS power backed up by the ATLAS diesel, so called UPS power, and UPS power from the Meyrin campus UPS, so called safety network.

2.3.2 Water

Primary circuit of water for ATLAS is provided by the Swiss water network WSNET. This feeds the LHC and its experiments. Primary water is used in the production of Mixed 15 °C and Chilled water 5 °C in SUX1, through massive chillers, that are electrically powered. The Mixed and chilled water circuits are a closed circuit that goes down to USA15 and UX15. The primary water circuit is cooled down in Point 1 at the SF1 cooling towers through natural evaporation. Closed circuits are used as exchange with the HVAC circuits and the cooling stations.

2.3.3 Ventilation

The global environmental requirements in the ATLAS cavern require that temperature should remain stable at 25±3°C and the humidity should be between 25% and 60%. Ventilation in SR1, SDX1, USA15, US15 and UX15 is obtained by chilling the air with chilled water through air handling units. SUX1 contains air-conditioning units that provide cooled air though ducts in the PX14 shaft to the underground areas.

2.4 Cooling

Secondary water circuits are used as exchange with rack cooling circuit and individual cooling stations.

2.4.1 Rack cooling circuits

Three rack cooling circuits exist in ATLAS, they are located in SDX1, USA15 and US15. In all three cases, the rack cooling circuit is a closed circuit that exchanges the heat with the Mixed water supply from the surface. Few selected racks are also connected to a by-pass network that uses tap water to keep the supply in the event of a cooling circuit failure.

2.4.2 Mono-phase cooling plants

Technology used is a coolant in a single phase. It exchanges heat by changing its PV properties, and picks up heat by increasing enthalpy. Table 2.2 lists the cooling stations in ATLAS.

Plant	Power (kW)	Refrigerant	Channels
Tile	55	Water	24 cooling loops
LAR	250	Water	24 cooling loops
Diff pumps	50	Water	12 cooling loops
Muons (A and C)	300	Water	26 cooling loops
ID evaporative (pixel and SCT)	60	C_3F_8	4 distribution areas
TRT	70	C_6F_{14}	4 distribution areas
Cables	80	C_6F_{14}	32 distribution areas

Table 2.2: ATLAS cooling stations

2.4.3 Evaporative cooling plants

The evaporative cooling system adopted for the pixel and SCT detectors uses a two-phases system as it circulates through the detector. The coolant, C_3F_8, is motivated by the non-flammable and non-conductive requirements. Cooling stations are: Inner detector cooling plant, Thermosyphon system, and the IBL cooling station.

2.5 Safety Systems

The safety responsibilities for the ATLAS infrastructure include the safety of the personnel and the environment, equipment and infrastructure of the detector during data-taking, access and maintenance.

2.5.1 Smoke detection system

There are two types of smoke detection in ATLAS: Environmental smoke detection and rack smoke detection. The environmental detection system consists of sniffing pipes distributed withing the buildings near the ceiling. Aspirated air reaches a sensor connected to a PLC, that sends a signal to a smoke central (SFDIN).

Rack smoke detection system consists of a smoke detector mounted inside the turbine of the rack, that sends a signal to a central. Smoke centrals send signals to the DSS in order to propagate alarms.

2.5.2 Flammable gas, ODH, O2, CO2

Flammable gas, ODH, O2, and CO2 detectors are distributed through the galleries and installed as independent detectors. They are connected to central (SGGAZ). There are also dedicated detectors installed inside the experiment. In this case they aspirate the

air inside the experiment volume and all the way to US15, the signals are handled by central SSSNI-001.

2.5.3 Radiation monitors

ATLAS uses CERN's new CERN Radiation and Environment Monitoring Unified Supervision (REMUS) [5] for radiation safety which is common to all CERN experiments. It monitors the ambient dose equivalent rates (H*(10)) and provides continuous measurement of induced radioactivity and prompt radiation. Furthermore, dedicated sensors are located near the gates.

2.6 The Detector Safety System

The Detector Safety System (DSS) [6] is a common development for the LHC experiments, responsible for the protection of each of the experiments equipment. It requires a high degree of availability and reliability, and it is designed to detect possible operational problems and abnormal and potentially dangerous situations at an early stage and, if needed, it is also responsible to bring the relevant part of the experiment automatically into a safe state.

It is composed of a front-end and a back-end part. The front-end is based on a redundant Siemens PLC, to which the safety-critical part of the DSS task is delegated. The PLC Front-end is capable of running autonomously and of automatically taking predefined protective actions whenever required. It is supervised and configured by Wincc OA, a Siemens SCADA system, via an OPC server. The supervisory layer provides the operator with a status display and with limited online reconfiguration capabilities. Configuration of the code running in the PLCs is completely data driven via the contents of a Configuration database. Fig. 2.8 shows the layout of DSS in ATLAS.

Seven detector safety units (DSUs) are distributed in ATLAS. Table 2.3 lists the DSUs in ATLAS. DSU 1 contains a PLC and all the input and outputs for the surface. DSU 2 contains the other PLC connected to the one in DSU 1 via an optical links. DSUs 2,3,4 and 5 are all located in USA15. They cover most of the rack smoke detection, environmental smoke detection, gas, cooling an cryogenics alarms, as well as the interlocks to all the racks, and the cooling stations. DSUs 6 and 7 are located in US15, and serve the rack and environmental smoke detection, the sniffer system, and

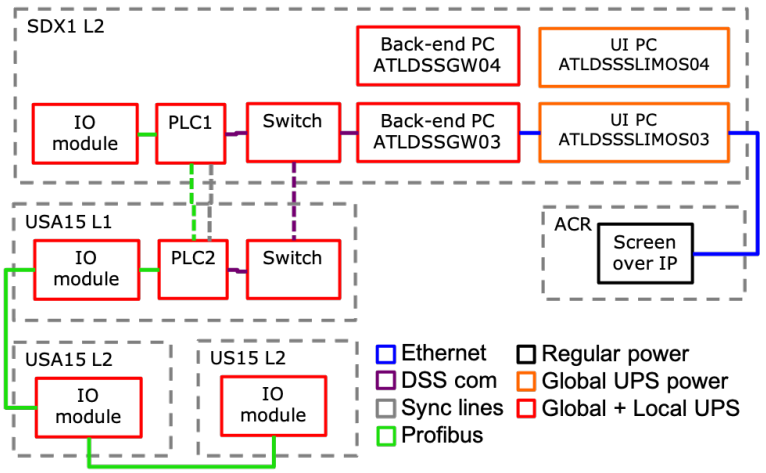

Figure 2.8: Layout of the ATLAS DSS.

DSU	Location	Rack
1	SDX1 L2	Y.18-06.D2
2	USA15 L1	Y.06-14.A1
3	USA15 L1	Y.07-14.A1
4	USA15 L2	Y.17-21.A2
5	USA15 L2	Y.16-21.A2
6	US15 L2	Y.12-05.S2
7	US15 L2	Y.11-05.S2

Table 2.3: ATLAS Detector Safety Units

the interlocks for the equipment in US15.

DSUs have inputs, if an input is active for a period longer than a minimum required persistency, it can trigger an alarm. DSUs have outputs that are connected to other systems as interlocks. If an alarm has an output associated, the interlock (action) can be activated when the alarm is triggered and thus, put the system in a safe state. The system is based on the concept of positive safety. In the event of a cable disconnected, the system is considered to be unsafe and it will trigger an action to return to the safe state.

2.7 The Detector Control System

The Detector Control System (DCS) [7] supervises individual detector components as well as the common experimental infrastructure. It enables equipment supervision using operator commands, reads, processes and archives the operational parameters of the

detector, allows for error recognition and handling, manages the communication with external control systems, and provides a synchronization mechanism with the physics data acquisition system. Given the complexity of ATLAS the usage of standardized hardware and software components ensure the efficient development and long-term maintainability of the DCS over the lifetime of the experiment.

Like the DSS, the ATLAS DCS uses WinCC OA industrial SCADA product to run a distributed system of 140 servers. Higher level control system layers allow for automatic control procedures, efficient error recognition and handling, manage the communication with external systems such as the LHC controls, and provide a synchronization mechanism with the ATLAS data acquisition system. Fig. 2.9 shows an online monitoring tool of DCS.

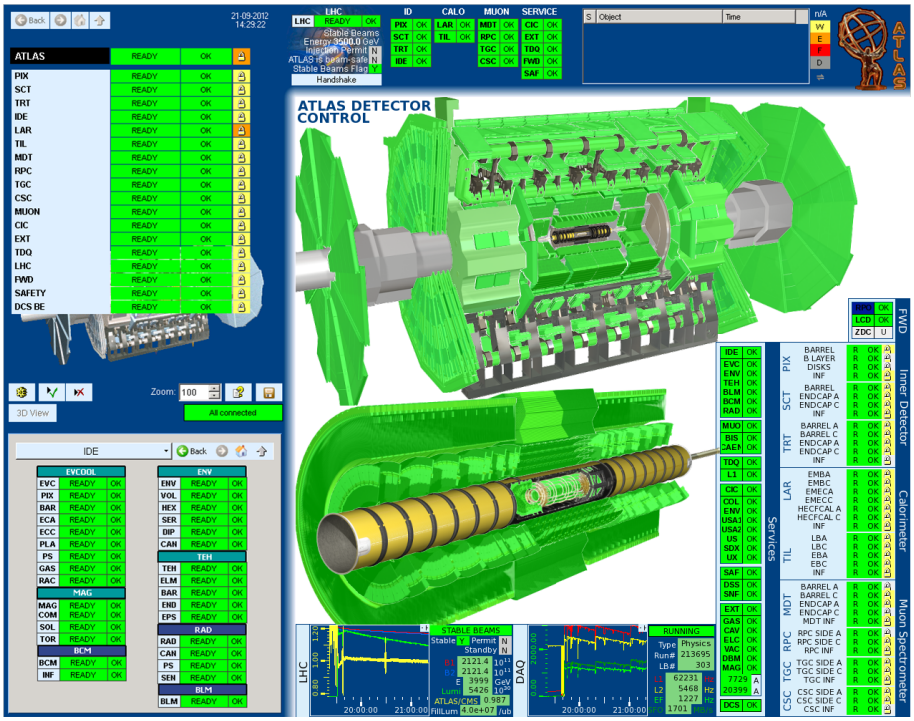

Figure 2.9: Online monitoring panel of ATLAS DCS.

Fig. 2.10 shows a diagram of the architecture of DCS. The DCS back-end has three layers, The local control stations (LCS) are responsible for the connection of the sub system front-end and its readout. The second layer consists of process control of subsystems with a single sub-detector control station (SCS) allowing its stand-alone operation. Global control stations (CGS) are running service applications and operator

interfaces, and provide the integration of the sub-detectors into the common ATLAS DCS.

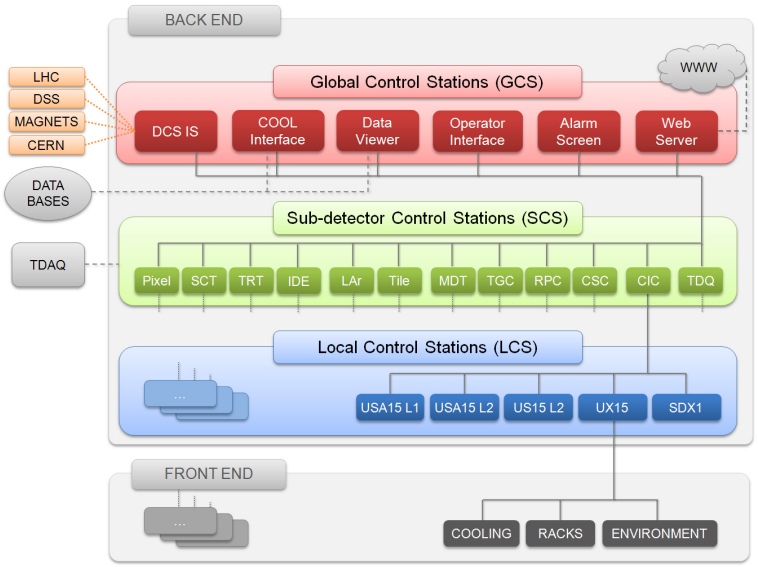

Figure 2.10: Block diagram of the ATLAS DCS architecture.

The DCS back-end is mapped onto a hierarchy of Finite State Machine (FSM) elements. State changes are propagated upwards and commands downwards in the hierarchy allowing for the operation of the complete detector by means of a single FSM object at the top level. For the top levels of the hierarchy, a fixed state model is applied. It reflects conditions optimal for physics data taking (READY), for unstable beam conditions (STANDBY), or an unpowered detector (SHUTDOWN). Compromised conditions are signalled by the NOT READY state, transient ones by TRANSITION. The state UNKNOWN is used when the actual condition cannot be verified. On lower level nodes, additional states reflecting sub-detector specific conditions are permitted. The actual state of these logical objects is determined by the states of the associated lower level objects (children) via state rules.

For critical parameters, alarms can be configured and are classified into one of the severity Warning, Error, or Fatal. To avoid the accumulation of a large number of alarms on the user interface, a masking functionality has been added to hide past occurrences e.g. after a follow up has been initiated.

Each FSM object in the lowest hierarchy level has an attribute called *Status* which assumes the highest severity of alarms active for the respective device. The *Status* is

then propagated up in the FSM hierarchy and thus allows for error recognition within the top layers of the detector tree and permits to identify problematic devices.

Chapter 3

ATLAS Expert System

3.1 Introduction

The huge infrastructure of the ATLAS experiment requires vast amounts of knowledge in many areas in order to execute a planned intervention or to react to an unexpected situation. With the aim of improving the knowledge base of the ATLAS experiment and help in the preparation of interventions an Expert System has been developed. Expert Systems are programs designed to gather expert knowledge, accept questions and provide answers with the goal of solving problems [8]. The dependencies between the systems in the infrastructure are sometimes hard to recognise and they are not always evident, even for experts in one domain. For example, an intervention in a cooling system, that it is well understood for the cooling expert, can reduce the heat dissipation in the cooling circuit of a set of racks that are supervising a task which the cooling expert is not aware. The ATLAS Expert System can foresee the impact of this intervention warning about the possible consequences, in order to reduce the probability of an unexpected event.

This chapter introduces the concept of expert systems and gives a detailed description of the design of the ATLAS Expert System including its architecture and features, simulation precision, and how it can be used in ATLAS.

All the work presented in this chapter has been done by a small team of people, within this group the author has been a main contributor and responsible for the project.

3.2 An Expert System for ATLAS

Chapter 2 illustrated an overview of the complexity of the ATLAS experiment and its infrastructure. The knowledge base of the ATLAS experiment's infrastructure is mostly documented in CERN's Engineering Data Management Service (EDMS) [9], a general purpose engineering documentation framework. Although it has accomplished its task during the life time of the ATLAS experiment, it does not provide an overall picture of the experiment's infrastructure because the information is highly compartmentalized, stored in many different formats, and indexed without sufficient meta-data in order to quickly navigate over the relevant documentation. To this end, the goals of the Expert System were set in order to overcome this limitation. The main goals of the Expert System are:

- Provide a description of ATLAS and its elements in a way that is understandable to a multi-disciplinary team of experts.
- Provide a user-friendly representation of the elements and their dependencies in graphical and text manner.
- Emulate the behaviour of the sub-systems by means of a simulator with different scenarios.
- The simulator has to accept input from the user and quickly answer how ATLAS would behave with the given input.
- Use standard technologies if possible to simplify maintenance.

With these requirements in mind, the ATLAS Expert System is conceived to describe the experiment's infrastructure including gas, cooling, cryogenics, ventilation, electricity distribution and detector safety systems, and their interaction with sub-detector systems (inner detector, calorimeter, muons) and magnets.

It is designed as a user-friendly web-based interface to a simulation tool that aims to allow non-experts to learn about the infrastructure.

3.3 Expert systems

Expert systems are computer programs which emulate the decision-making process of human experts. They have a long history dating from the 1970s and 80s. Usually

consisting of a knowledge base, an inference engine, and a user interface. There are 4 main types: rule-based, object-oriented, fuzzy and neural. Although there can be hybrid versions which combine the different types to provide the best solution like the fuzzy-neural.

In rule-based expert systems the knowledge base is expressed in a set of rules in the form of IF *condition based on experience* THEN *consequence based on experience*. Rules can combine logical AND or OR clauses.

Object-oriented expert systems, also known as frame-based, use objects to represent knowledge base and decision making. The objects store the knowledge and the inference engine applies rules associated to the attributes. Object-oriented expert systems use class inheritance which is an essential feature of the programming paradigm that provides the benefits of code re-usage and simplification [10].

Fuzzy expert systems use many-value or non-binary logic [11] to represent states that are not completely true or not completely false. They are intended to describe non-linear and complex behavior systems.

Neural expert systems are those that use neural networks to extract an output. These networks can be trained by experience and applied to unforeseen situations.

The ATLAS Expert System has been designed as an object-oriented expert system, using inherited attributes to define behaviours of types of systems in the infrastructure as it will be further discussed in section 3.5.1

Fuzzy logic has been evaluated several times as an extension of the Expert System, in order to describe objects that are affected but not totally off. Despite this interesting concept, the repercussions of this logic result in many new states for the objects that are not easy to understand. The benefit of a neural network relies on the training of past events, which are however limited in time and impact. The current object-oriented model has a deterministic outcome that is not compatible with the training of a neural network node.

3.4 Architecture

From a technical perspective, the system is divided in three components: an object-oriented database, a python server and a web application with a client–server architecture. Fig. 3.1 shows a block diagram of the system's architecture where the blue outer

lines around the blocks represent physical layers.

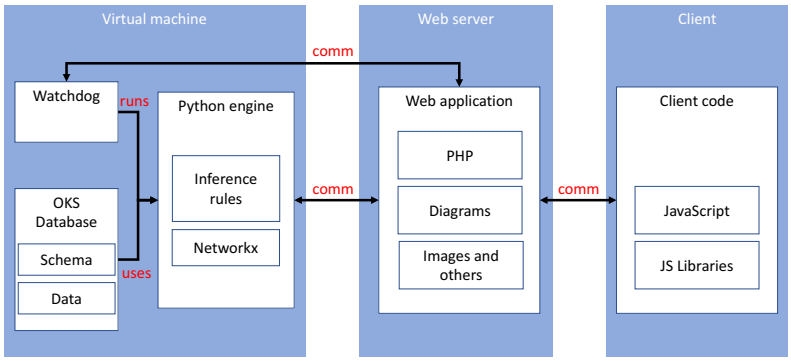

Figure 3.1: Block diagram of the Expert System's architecture

3.4.1 Back-end

The back-end is composed of the object-oriented database and the python server.

The database is the *ATLAS TDAQ object-oriented configuration database* also called *Object Kernel Support* (OKS) [12], which it is expected to be maintained during the life of the experiment which makes it the perfect candidate for such task. Objects are described as an instance of a class defined in the schema. Each class can have attributes of any standard type (string, integer, float) and cardinality (single, multiple), and relationships, that are a special kind of attribute where the type is any other class defined in the schema. To describe different elements of the infrastructure we require many classes e.g. racks, computers and electrical switchboards. Some classes represent physical objects like a rack or a crate, while others represent abstract concepts like DSS alarms (described in 2.6) or PLCs. Since the aim of the Expert System is to have a functional description of the infrastructure, the implementation is chosen to reduce the amount of code while keeping the explanation realistic.

The python online server runs the inference logic engine applying rules based on the database objects, with their attributes and relationships, and interacts with a web application, receiving user input and providing scenarios as answers. The engine uses the Python Networkx [13] graphs and network library which is used to transform the mesh of systems from the database into a graph. It also allows the usage of standard tools in the detection of cycles and measurement of the closest distance between nodes. A watchdog daemon running in the virtual machine hosting the server manages the

execution of the environment, it can for example receive commands from the client side to restart the python engine.

The client-server communication protocol is a custom-made protocol which uses widely used technologies like JSON and asynchronous JavaScript. Requests are sent to the server using commands such as *FindObject*, *ChangeSwitch* and *TriggerAlarm*. There is a total of 87 commands implemented. Request and replies include meta-data like an *Exception* which can warn about errors during the simulation and *TokenId* to distinguish between different users.

3.4.2 Front-end

The front-end user interface consists of a web application built in PHP which runs in a CERN hosted web server and contains JavaScript code that is executed in the client browser. Fig. 3.2 shows the application's welcome page, the page shows a search box that allows the user to quickly search for an element, and a list of links to pages with the most visited or relevant diagrams describing parts of the ATLAS infrastructure. Table 3.1 shows the list of diagrams in the Expert System. The actual diagrams are built on-the-fly from an XML description using the MXGraph [14] library.

Figure 3.2: Expert System welcome page

3.5 User interface

The user can interact with the Expert System with two different oriented types of interface. The first type is a visual-oriented interface with descriptions in the form of diagrams. They are flow chart-like diagrams similar to those used in SCADA systems.

Family	General diagram	Dedicated diagram
Sub-detectors	Detector status	IBL, Pix, SCT, TRT, LAR, Tile, MDT, RPC, TGC, CSC
Electricity	General, 18kV, Diesel	UPS SDX1, SX1, USA15, US15
Racks		Gas Racks, Racks SR1, SDX1, SGX1, USA15, USA15 A2P, US15, UX15
Magnet	Summary	Magnet cryogenics, Vacuum, Electricity
Cryogenics	Distribution	SH1, USA15, UX15, ANRS, Argon
Water	Distribution	SF1, SPS, SUX1, SH1, SDX1, USA15, US15, back-up chiller
Gas	Summary	CSC, MDT, RPC, TGC, TRT, TFC
Cooling	Detector	CR Room, US15, UX15, IBL, Evaporative, TRT, Cables, LAR, Tile, Muons, Diff. pumps
Safety	Safety	Light, Elevator, Sniffers, Flammable gas, Smoke, Fireman boxes
DSS	DSS racks	DSU
Services		Compressed air, Network, Ventilation

Table 3.1: Visual diagrams in the ATLAS Expert System.

This view provides general pictures of sets of systems and how their elements are interconnected. The second type is a tables-and-lists oriented interface that provides detail description of elements including relationships, pictures and relevant information.

Fig. 3.3 shows the safety page, an example of the visual-oriented interface. The upper blue bar is present in both types of interface. From left to right it shows the menu icon, the page's title, the number of affected alarms and systems, the language options, a button to reset the simulation, the search box and simulation time constraints.

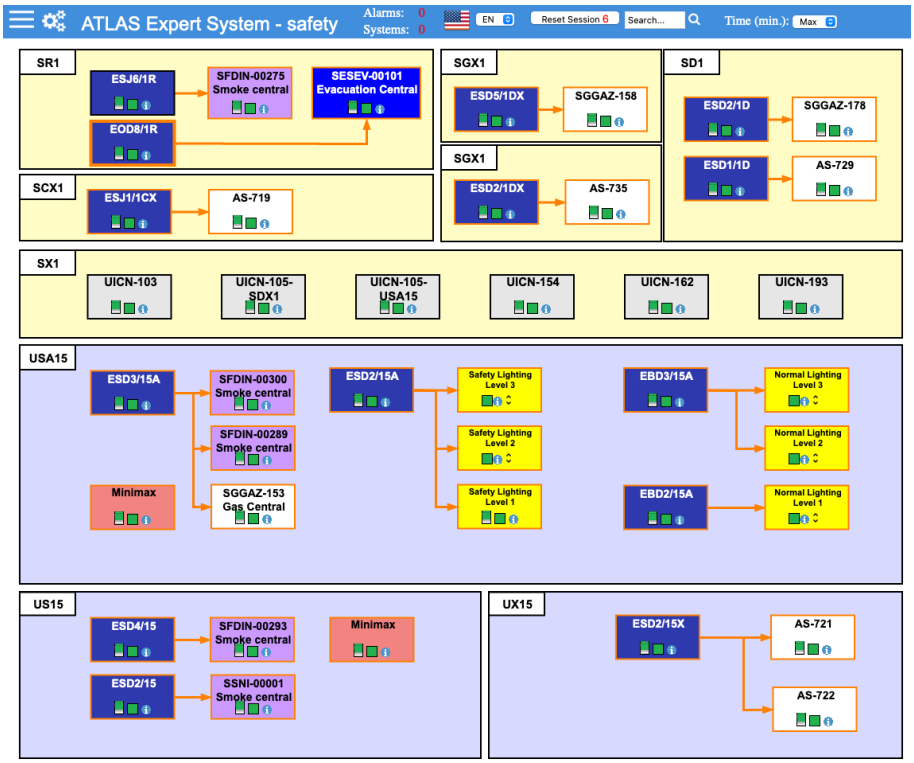

Figure 3.3: Expert System safety page

Bellow the blue bar, we can see the diagram which is divided in large squares with

a label in the top left. They represent areas or buildings in the infrastructure. A color convention has been established on which yellow background indicates surface buildings and blue background indicate underground caverns. The smaller boxes represent individual or groups of systems. They also follow their own color convention to distinguish types of systems. In this diagram, we can see switchboards in deep blue, smoke detection centrals in purple, minimax (fire extinguisher system) central in orange, lighting in yellow and gas and other systems in white. The lines between the systems indicate a relationship between them and the arrow indicates the parent-child direction of this relationship. Black color lines indicate normal powering, there can be other colors such as orange for UPS backed up powering and blue for water. Fig. 3.2 shows examples of coloring convention.

Figure	Fill (Hex)	Outline (Hex)	Type	Meaning
	2F39AE	FF8000	Box	Switchboard with UPS or Diesel coverage
	3DA2EA	000000	Box	Water system with normal power
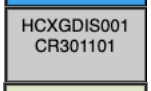	CBCBCB	000000	Box	Gas system with normal power
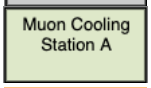	FF0000	000000	Box	Control or monitoring
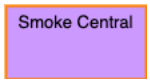	CC99FF	FF8000	Box	Smoke central with UPS or Diesel coverage
	FF0000	-	Line	Control or monitoring
	000000	-	Line	Power supply
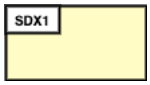	FFFCC5	000000	Area	Surface area or building
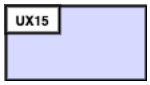	D7D9FF	000000	Area	Underground area or building

Table 3.2: ATLAS Expert System color convention.

Fig. 3.4 shows a detail of the safety page. The ESD2/15A box represents an electrical switchboard supplied from the safety network. Inside the box there are three icons with the functions of *switch*, *state* and *more info* buttons. The three boxes on the right

part are groups of lighting systems and contain three icons: *state* in green, *more info* and *expand*. Groups don't have switch button because it is not allowed to switch off a group of objects, they are an arbitrary collection of objects. The *expand* button shows all the elements contained in the group.

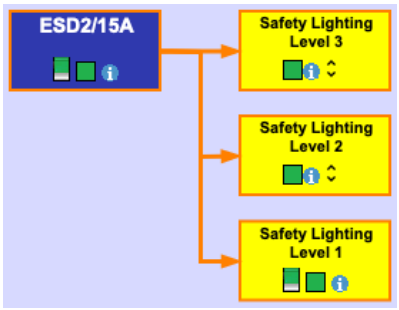

Figure 3.4: Detail of the Expert System safety page

From the visual-oriented interface, the user can take the action of switching off an element by clicking the left most button in the box. This will start a simulation and the first feedback to the user will be the switch turning to red. Then a spinning wheel will show that the simulation is running. Once the simulation is finished the results will be transmitted to the front-end and the user can immediately see the consequences. The upper bar will show at least one system is affected and other elements in the diagram will change their state (state button turning red) if they are affected by the simulation. The user can continue then to interact with the system that will continue to show the current simulation until the reset button is pressed. Once a simulation has been triggered, all the pages will show the impact of that simulation.

In order to avoid unnecessary information flow between the back-end and the front-end, only the status of the objects represented in the page will be returned, as well as a summary of the objects affected and alarms triggered by the simulation.

Fig. 3.5 shows an example of the tables-and-lists oriented interface with the search functionality. The table in the left part shows filtered items and the columns in the right show the attributes, relationships and pictures of the selected system. The user can navigate in the most-right column through clicking links to nearby systems.

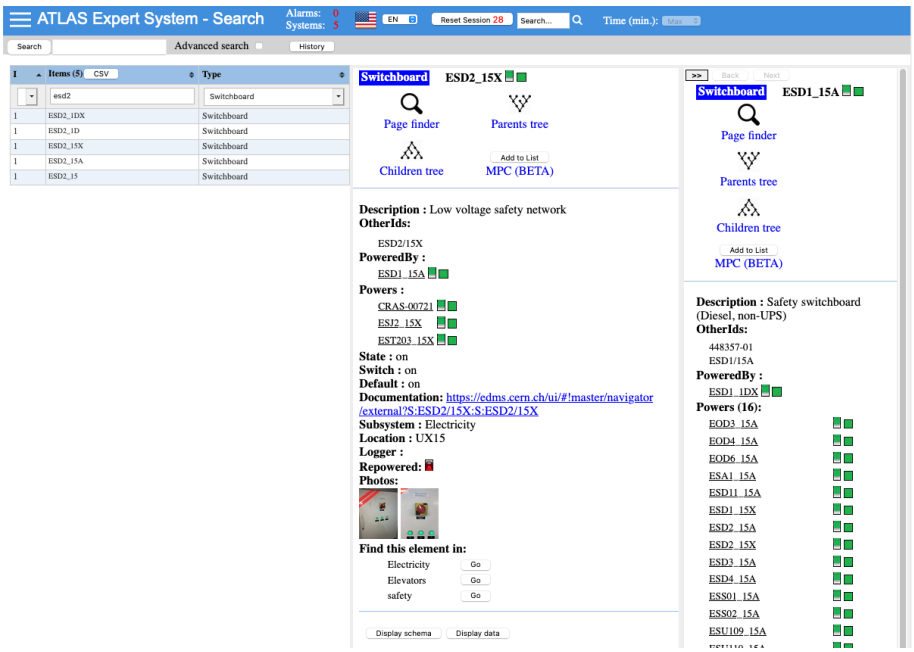

Figure 3.5: Expert System tables-and-lists oriented interface

3.5.1 Knowledge representation and Inference Engine

Each type of object is stored in the database as an instance of a class. One object can have *n* number of relationships. These can be relationships that *feed* the current class, and those that feed another class. The objects in the former type of relationships are called parents, and the ones in the later are called children. Making use of the object-oriented programming paradigm, classes that implement relationships that feed from another class extend from the feeder class, and those that provide to another class extend from the provider class. When a simulation is triggered, the engine calculates each object's state based on the state of its parent objects.

For example, a physical rack is described as an object using the class *Rack*. Fig. 3.6 shows the class *Rack* diagram model. Rack objects can have relationships like power sources (*poweredBy*), computers contained inside (*contains*), interlocks (*interlockedBy*) or cooling requirements (*waterFrom*). In this case, the parents are the objects behind the *Provider Based* relationships like *poweredBy*, *interlockedBy* and *waterFrom*, while the children are those behind the *Receiver Based* relationship like *contains*. When solving the state of an object, all the objects within one relationship are considered at once, and they are solved by the inference engine applying a set of rules.

The individual resolution of every feeder relationship contributes to the final state of the object.

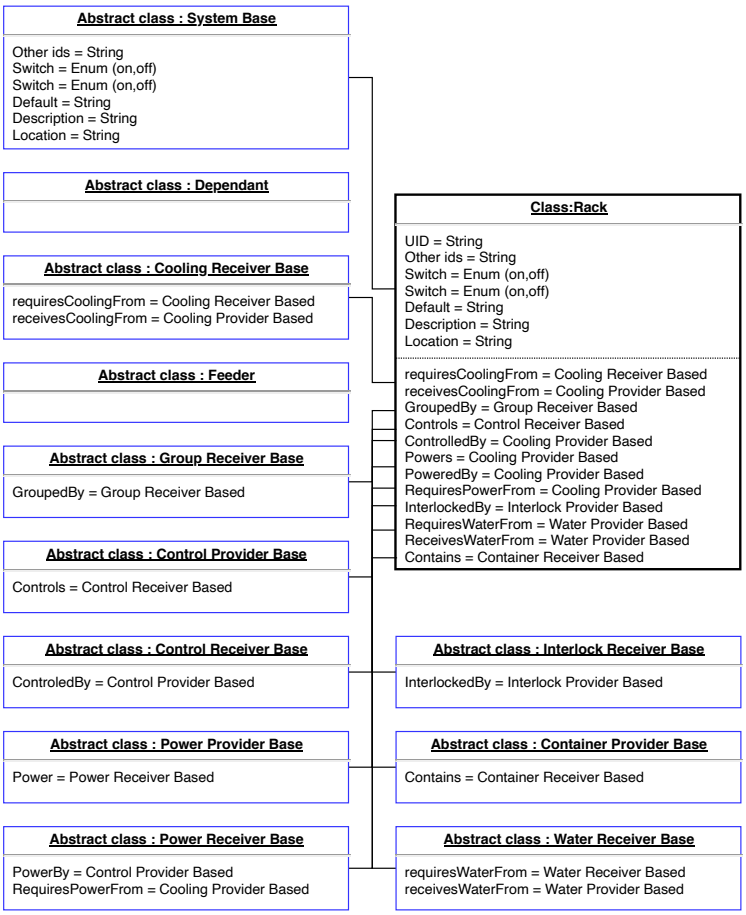

Figure 3.6: Inheritance diagram of the class Rack in the Expert System

A graph representation is built with all the objects in the database using Networkx *MultiDiGraph* object where the edges correspond with the relationships. When a simulation is triggered due to the change of state of any element, a resolution of the state is propagated over the dependent objects traversing the graph using the breath-first algorithm, process shown in Fig.3.7. Due to the circular dependencies between the dependent objects, the process is repeated as many times as required for achieving a stable state. Once this stable state is reached, the result is sent to the user interface.

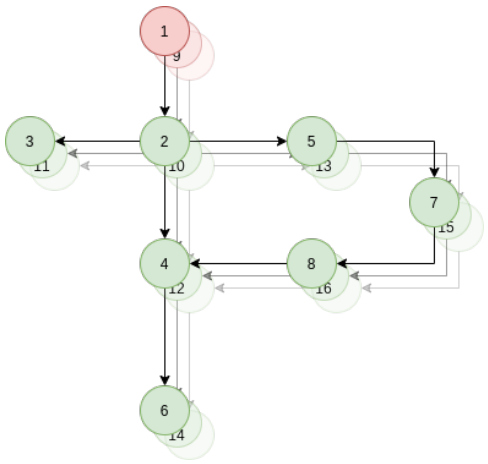

Figure 3.7: Depending objects breadth-first propagation order

3.6 Simulation example: Annual water maintenance

Annual interventions play a key role in the infrastructure maintenance and safety of the detector. Although they are carried out every year, errors may occur due to oversights of routine procedures. To prevent this, the Expert System is used before these interventions to evaluate the impact in detail, and accordingly, take preventive measures to minimize its impact.

The following example corresponds to the annual maintenance of mixed water production chillers which is a clear example of an intervention whose impact is usually underestimated. The intervention implies the maintenance of the 2500 kW chillers located in SUX1 that take water from the primary circuit and chill the secondary circuit down to 15°C. This mixed water is circulated down to USA15 with the help of two 22 kW pumps where it is used by the heat exchanger of the rack cooling circuit as primary cooling for the racks. It is also pumped again in USA15 to the UX15 cavern where it is used as primary for four cooling stations (Muon A, Muon C, Tile, LAr). The mixed water is also pumped to SDX1 for the cooling circuit of the racks.

Fig. 3.8 shows the Expert System water distribution page while simulating the aforementioned maintenance intervention. The blue bar at the top shows the massive impact on operation: there are 41 alarms and 5288 systems affected in total. The two black outlined squares on the right, FUPF1-00200 and FUPF1-00201, are expanded groups displaying the two intervened (switched off) systems, HAA-1411 and HAA-1401. Each of them is a TRANE CVGE050 centrifugal compressor that uses 625 kg of

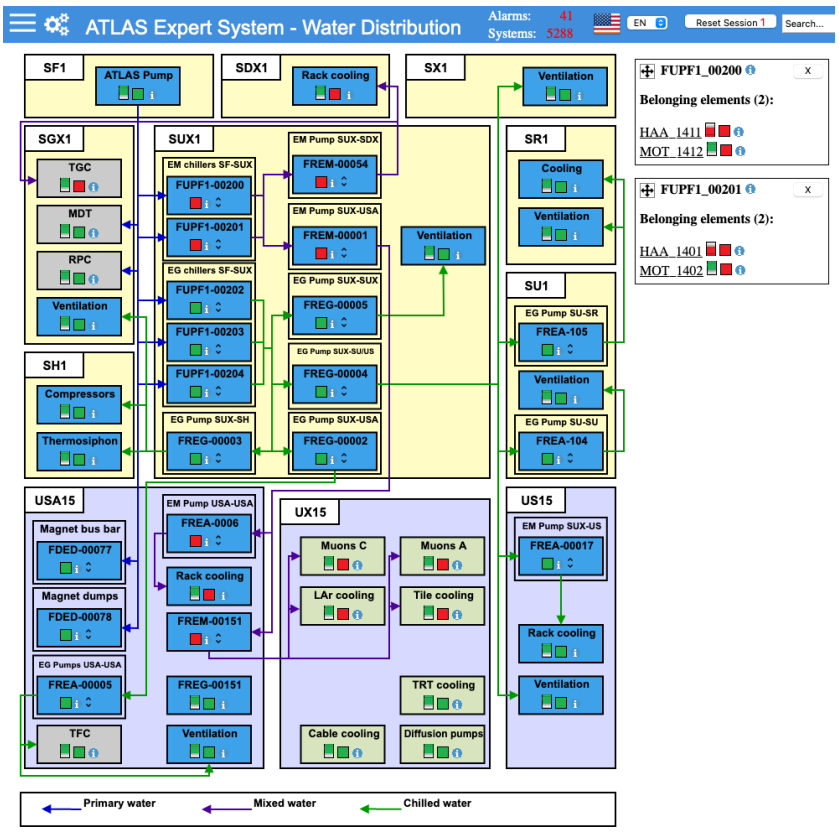

Figure 3.8: Expert System water distribution simulating annual maintenance of chilled water

R-134a as a refrigerant for an output cooling power or 2.5 MW. From this page, we can already observe the impact of the intervention in Rack cooling in SDX1 and USA15, muon cooling stations C and A was well as LAr and Tile cooling stations. Rack cooling groups include many racks which are critical for monitoring.

Fig. 3.9 shows the detector status page with severe impact during the intervention. Fig. 3.10 shows the Expert System dashboard page. The dashboard shows relevant information about the intervention that can be downloaded in CSV format for offline analysis. The panel in the top shows on the left the list of commands executed by the user, and on the right the list of most important parts of the infrastructure affected in the intervention. The panel in the middle shows the DSS status, with lists for triggered alarms, inhibited items and actions taken by DSS. The panel in the bottom shows lists with elements affected in the simulation grouped by types of elements.

This is a simple simulation that can be triggered in 2 clicks and takes 2 seconds

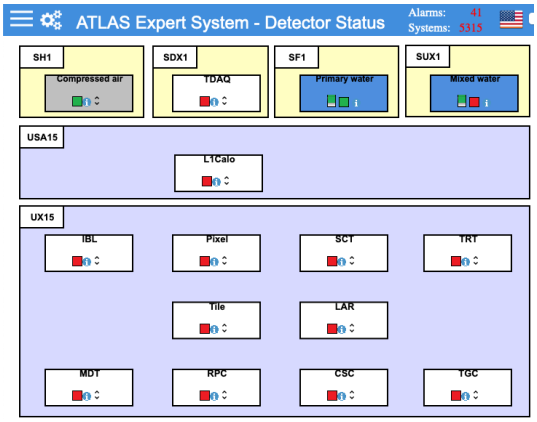

Figure 3.9: Expert System sub-detectors page simulating annual maintenance of chilled water

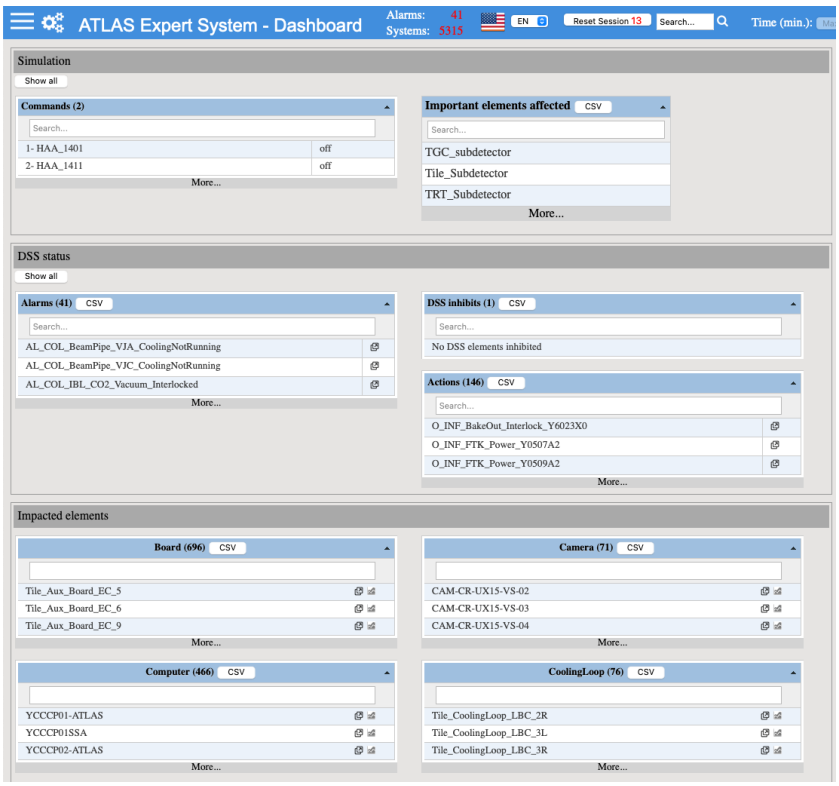

Figure 3.10: Expert System dashboard showing the simulation report

to run. The outcome of the simulation can be interpreted by any of the visual pages of the Expert System, including the preferred sub-detector page for the user, and can be evaluated in terms of alarms triggered and systems affected. Post mortem intervention analysis is used every year as a source of information to improve procedures and the exactitude of the Expert System knowledge base. Currently, the simulation has been proved, using these analysis, that it describes the detector's behaviour with a high degree of accuracy during the intervention.

3.7 Reliability of ATLAS equipment

Expert System simulations allow to investigate the consequences of user proposed changes to the infrastructure. Furthermore, using the ATLAS Expert System we can establish a model to estimate the reliability of a system [15]. Let P_s be the probability of success defined as the odds of a system of accomplishing its assigned task [16] and the probability of failure P_f is calculated as $P_f = 1 - P_s$. In the following paragraphs we will assume that P_s of individual components can be inferred from the Knowledge Base.

We build a reliability functional block diagram for a system as a fault tree in which all elements affecting the reliability of the system under study are represented as nodes with a given input and output. We will define the P_s of a given system as the composite P_s of all the nodes. We considered as possible configurations nodes in series and parallel. In a series configuration, a failure of any of the component results in the failure of the entire system. In a parallel configuration, at least one of the elements is required to succeed.

The probability of success of a system in series P_s^s of X_i components is the product of the $P_s(X_i)$ of the components as described in equation 3.1

$$P_s^s = \prod_{i=1}^{n} P_s(X_i) \tag{3.1}$$

The probability of success of a system in parallel P_s^p is defined as the complementary of the dot product of the complementary of the components, as described in equation

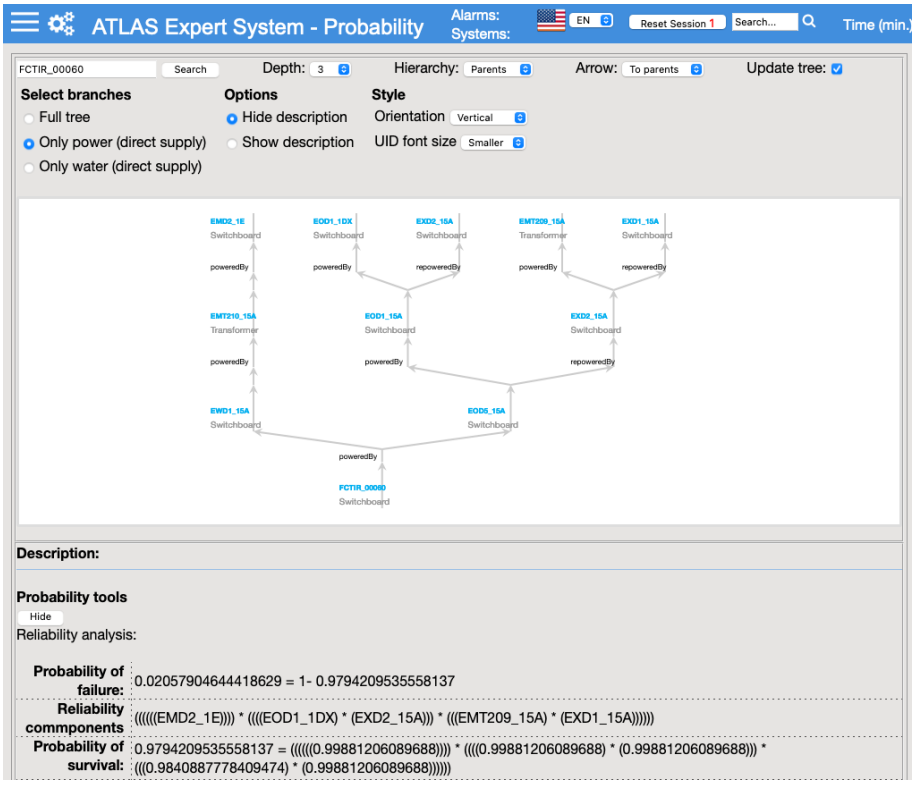

Figure 3.11: Expert System reliability analysis tool result for FCTIR-00060

3.2.

$$P_s^p = 1 - \prod_{i=1}^{n} (1 - P_s(X_i)) \tag{3.2}$$

Fig. 3.11 shows the reliability analysis of the FCTIR-00060 switchboard, the main power line to the evaporative cooling of ATLAS. On the top, we can see the dynamic tree tool setting and the parents tree of FCTIR-00060. Underneath, there is a table with the risk analysis results: probability of failure $P_f = 2.05\%$, reliability components and probability of survival full formula.

We can deduce the principal components of a given system by calculating the probability of failure of all its nodes. In this case, the calculation is done repeated times, on each the reliability of a different node is reduced. This way we examine the effect of each component's reliability on the overall system reliability and deduce which is the principal component of the system of the evaporative cooling.

Performing a probability of failure analysis on every system in the knowledge base

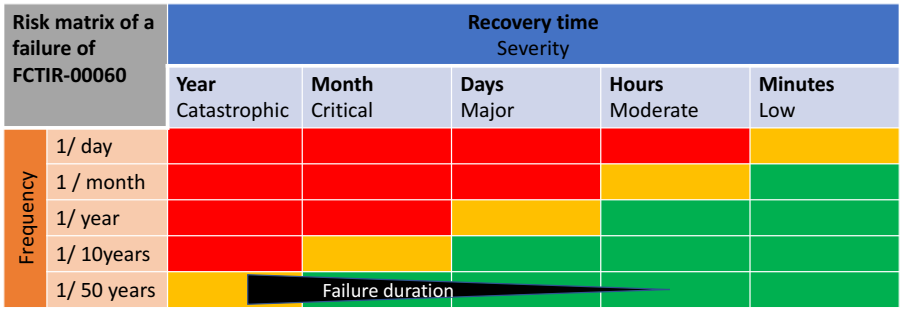

Figure 3.12: Risk matrix of a failure in FCTIR-00060

we see interesting results. In a sample of 1762 entries with a mean of 96.2%, the object representing the switchboard FCTIR-00060 has a probability of success P_s of 46.63% with a confidence level of 95%. Although each system has been assigned with an arbitrary P_s, one interesting observation is our calculations agree with the ATLAS records. Systems with history of being more problematic are indeed scored with lower P_s in the analysis.

Fig. 3.12 shows a risk matrix to determine the risk as a function of the frequency of a failure and the time to recover from this failure. Although the probability of failure of FCTIR-00060 is low, it can have a catastrophic severity. The severity of a failure in FCTIR-00060 increases with the duration of the failure. Inner detector modules contain hybrid sensors with wire-bonds that are very sensitive to rapid changes in temperature and are constantly cooled to -25°C. A failure in the cooling would provoke a thermal shock breakages in the wire-bonds and hybrids themselves. The recovery time from this event would depend on the number of damaged modules and the spare units.

3.8 Most Probable Cause

The Expert System can search the Most Probable Cause (MPC) for a user-provided scenario traversing the graph representing the dependencies in a reversed direction. The scenario is provided to the MPC algorithm as a list of elements. The cause is calculated in an exhaustive manner searching for the common parents of all the elements in the list. These parents are then filtered and only those that affect all the elements in the list are selected. This is done by running a breadth-first algorithm starting from each object provided by the user and filtering the parents who are present in all the results.

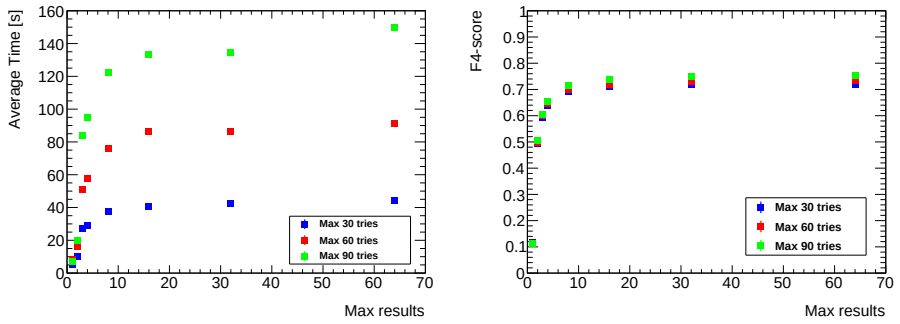

Figure 3.13: MPC algorithm performance. Left: Average processing time vs maximum number of results. Right: F_4-score vs maximum number of results

Furthermore, the MPC can be executed in non-exhaustive way filtering the parents that affect at least the elements provided in the list. This mode is intended for experts that might not have the full picture of the affected systems. The MPC algorithm shows best performance in terms of speed when it orders the provided objects by eigenvector centrality before processing them.

The MPC algorithm uses two parameters. First, the maximum number of attempts which is the number of parents that will be processed. Second, the number of results shown to the user. Fig. 3.13 right shows stabilization of the F_4-score showing a value of 0.7 after 8 results. The F_4-score is a measure for the quality of the results that is calculated by Eq 3.3 where β is equal to 4. Precision is the number of correctly identified positive results divided by the number of all positive results including those not identified correctly. The recall is the number of correctly identified positive results divided by the number of all samples that should have been identified as positive.

$$F_\beta = (1 + \beta^2) \cdot \frac{\text{precision} \cdot \text{recall}}{(\beta^2 \cdot \text{precision}) + \text{recall}} \tag{3.3}$$

The left part of the plot in Fig. 3.13 indicates that the number of attempts does not strongly affect the maximum results and consequently also not the quality of the results. Therefore, increasing the maximum number of results would increase the processing time without significantly improving the quality of the results. A number of 8 maximum results and 30 tries has been established as the best parameter set for the algorithm in terms of time vs accuracy with an average time of 37 s and a F_4-score of 0.7.

Fig. 3.14 shows the MPC tool output after entering the list of 41 alarms which were

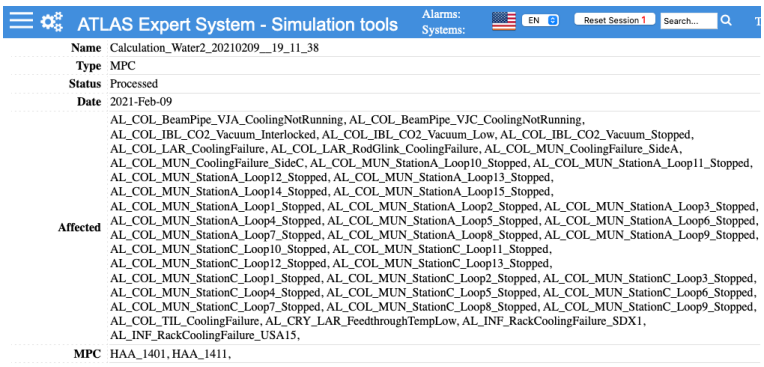

Figure 3.14: Expert System MPC result of the scenario during water distribution simulating annual maintenance of chilled water

triggered during the annual maintenance of the chilled water production system. The result is calculated to be HAA-1411 and HAA-1401 which correctly reflects the real root cause. The process is more time consuming compared with the normal simulation, around 10 minutes compared to typically a few seconds. The results are stable and reproducible. The state of other elements of the database does not influence the speed of the algorithm, and the same result is obtained each time. In order to speed up the simulation further, the result could be stored in a pre-computed cache of expected scenarios, that could be presented to the user with very little latency.

The search for the MPC can be used to understand many situations in the control room and by safety system experts in the early steps of critical situations, when time is essential and the cause of a failure is not well understood.

3.9 Conclusions

This chapter has described the design and development of an object-based Expert System that gathers expert knowledge of many domains of the ATLAS detector infrastructure. It offers to the users a visual oriented and list oriented set of pages, and a simulator tool to be used for operation and interventions. It is already used in ATLAS to plan interventions through simulation, that can be used to understand the extent of the intervention, and allows for implementation of compensatory measures to reduce their impact. Nevertheless, it is mandatory, that the Expert System is kept up to date with the upgrades of the detector like the ones that have taken place during LS2.

In addition to being a simulation tool that extends the knowledge base of ATLAS

the Expert System has additional functionalities, it extends its functionality in risk analysis tools like Fault Tree Analysis. It also helps in the understanding of real events with a most probable cause tool which accepts input of what is happening and responds with possible causes. The performance, evaluated as the agreement between the simulations and the actual impact of interventions or events, shows good results with a high degree of agreement and a fast simulation time.

Chapter 4

Pixel detectors technology

4.1 Introduction

The purpose of this chapter is to give an overview of the silicon pixel sensors technology in high energy physics and to explain their most fundamental concepts necessary to understand chapter 5. It also outlines the processes involved in the interaction of radiation with matter and it introduces the MALTA family of Monolithic Active Pixel Sensors which target the High Luminosity LHC and future HEP experiments; and the SEU_TJ180, a chip designed to test the effects of radiation on the memories of this technology.

4.2 Interaction of particles with matter

Particles passing through matter results in the deposition of energy. The amount of energy deposited depends on the particle, its energy and the material.

Photons, as the particles resulting from electromagnetic radiation, interact with matter via three processes: the photoelectric effect, the Compton effect and pair production. The photoelectric effect consists of the emission of electrons due to ionization of the material in which a photon transfers its energy to an electron that is released from an atom. The Compton effect is the scattering of a photon by the electric field of a charged particle, typically the electron of an atom. In this process, not all the energy of the photon is absorbed, and the energy that is not used for the displacement of the elec-

tron is emitted as a new photon. Pair production is the process through which a photon produces a pair of particles where one is the anti-particle of the other, conserving the energy and quantum numbers. Typically an electron (e^-) and a positron (e^+) that both have a mass of 512 keV are the result of pair production of a photon in excess of 1.024 MeV.

In all these process we can measure the intensity of the incident particle beam as $I(x) = I_0 e^{\frac{-x}{\mu}}$. This describes the attenuation in intensity of a monochromatic photon beam penetrating through a material where I_0 and I_x are the initial and final beam intensity, x is the thickness of the material, and μ is the attenuation length property of the material which depends on the photon energy [17]. As result of the photoelectric effect and pair production the energy is completely absorbed and in the Compton effect it is scattered in the material in a relatively large angle which will be commented later. Fig. 4.1 [17] shows the probability of photons absorption as a function of photon energy.

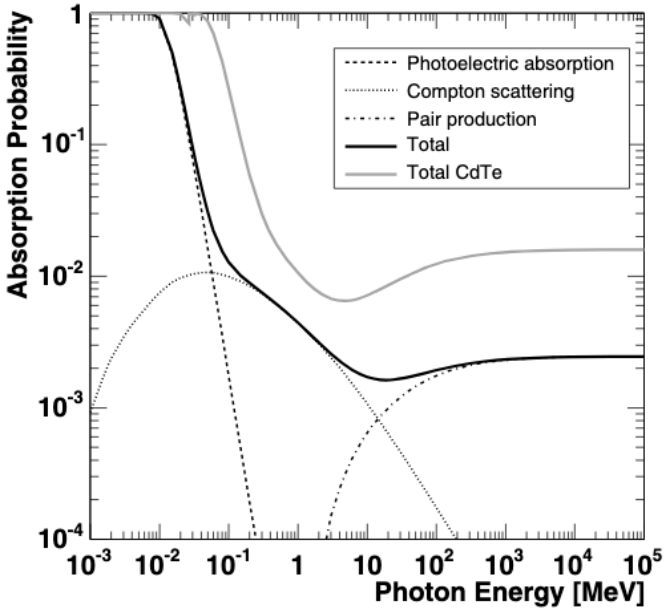

Figure 4.1: Probability of photon absorption for 300 μm silicon

Charged particles loose energy when interacting with matter via ionising collisions with electrons. The Bethe-Bloch formula (4.1) describes the mean particle energy loss

per unit length [18] in the valid range of $0.1 \leq \beta\gamma \leq 1000$.

$$-\left\langle \frac{dE}{dx} \right\rangle = Kz^2 \frac{Z}{A} \frac{1}{\beta^2} \left(\frac{1}{2} ln \frac{2m_e c^2 \beta^2 \gamma^2 T_{max}}{I^2} - \beta^2 - \frac{\delta(\beta\gamma)}{2} \right) \tag{4.1}$$

Where $K = 4\pi N_A r_e^2 m_e c^2 = 0.307075$ MeV cm^2, N being the Avogadro's number. z is the charge of the traversing particle in units of the electron charge. r_e is the classical electron radius. m_e is the electron mass. $m_e c^2$ is the electron rest mass energy. $\frac{Z}{A}$ is the ratio between atomic number and atomic mass of the material. I is the mean excitation energy. β is the velocity of the traversing particle in units of speed of light. γ is the Lorentz factor expressed as $\gamma = \left(\frac{1}{\sqrt{1-\beta^2}} \right)$.

Fig. 4.2 [18] shows an example of the positive value of the dE/dx, also known as the stopping power of the material, for muons traversing copper.

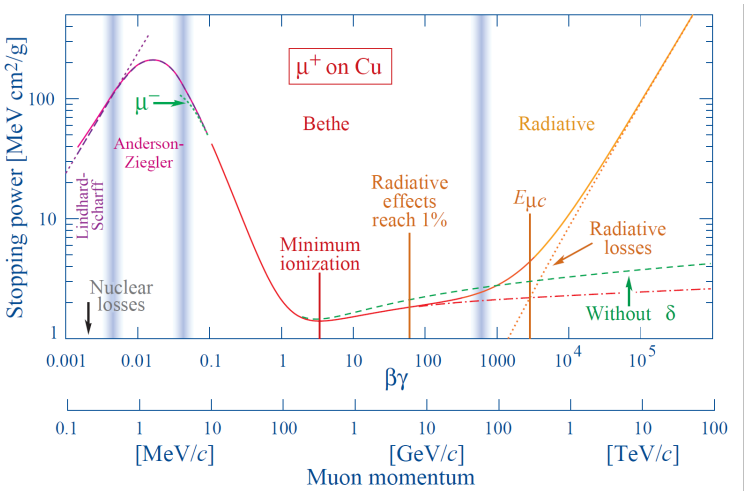

Figure 4.2: Stopping power for muons in copper as a function its momentum in $\beta\gamma$

Electrons at low energies lose energy due to ionisation. At higher energies, above tens of MeV, the dominant effect of energy loss is bremsstrerahlung, a photon emission produced by the deceleration of electrons when deflected by the nuclei. Fig. 4.3 shows the energy deposition distributions for electrons in silicon of 25 μm thickness at energies used in the beam facilities of DESY (Hamburg, Germany).

The radiation length, measured in X_0, is the thickness of the material over which the charged particle's energy is reduced by a factor of e in $E = E_0 e^{-x/X_0}$. When charged particles traverse a material, they are scattered in multiple angles due to the Coulomb interaction between the particles and the nuclei, having an important impact on the res-

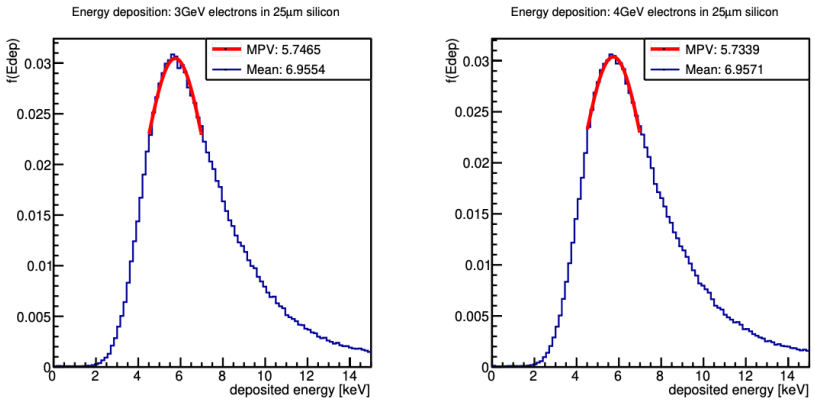

Figure 4.3: Energy deposition distributions for electrons at 3 GeV (left) and 4 GeV (right)

olution of silicon detectors with many layers. Multiple Coulomb Scattering angle after many iterations follows roughly a Gaussian distribution in root-mean-square (RMS) expressed as

$$\Theta_{plane}^{RMS} = \frac{13.6MeV}{\beta cp} z \sqrt{\frac{x}{X_0}} \left[1 + 0.038 ln \frac{x}{X_0} \right] \tag{4.2}$$

where angle Θ is expressed in rad, p is the particle momentum in MeV, βc is the velocity in units of the velocity of light, and z is the charge number of the projectile and x/X_0 is the thickness of the scattering medium in radiation lengths [17].

4.3 Silicon pixel sensors

Pixel detectors use diodes to detect passing particles. The diodes use a junction of a *n-type* (electron donor atoms) silicon in contact with a *p-type* (electron acceptor atoms) silicon to create a space charge region, in which current can only flow in one direction, this is called the *p-n junction*. Fig. 4.4 shows the space charge region in the depletion region causing an electric field across the junction. The potential difference is the built-in voltage. A reverse biased diode, will not allow current to flow, except of course if new charge carriers are generated in the circuit.

Electron-hole pairs generated by a traversing particle can be detected because they will create a current in the diode. In a semiconductor the electrons will flow to the *n-doped* region, and the holes to the *p-doped* region. The charges created along the path of a charged particle, will continue to be collected by the electrodes of the cir-

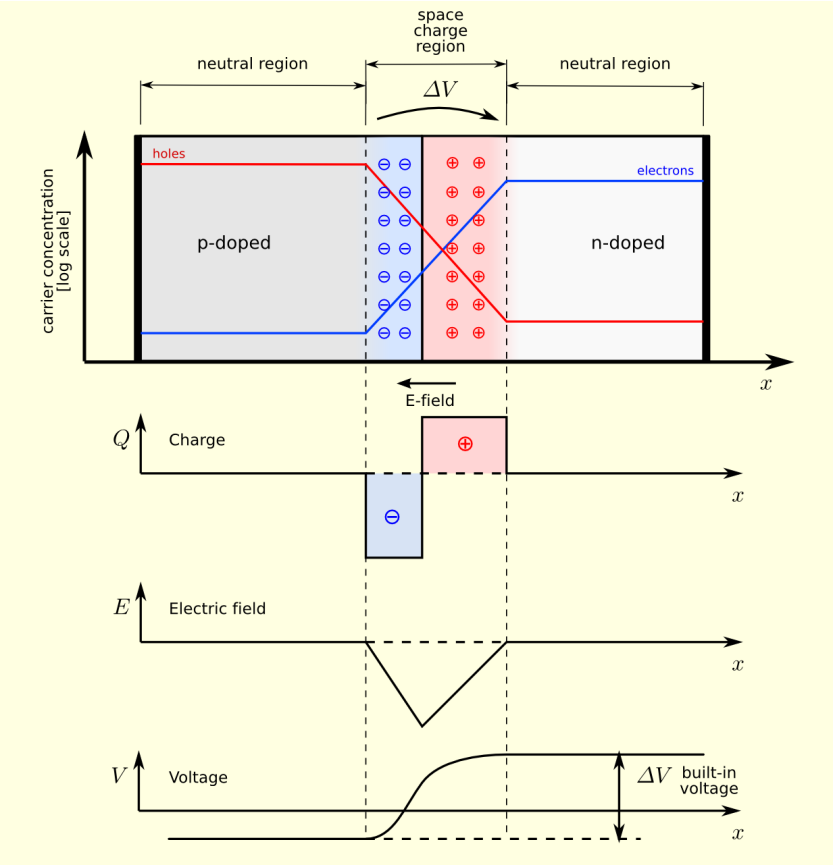

Figure 4.4: Top: A p-n junction in thermal equilibrium with zero-bias voltage applied. Under: plots for the charge density, the electric field, and the voltage. Source from Wikipedia

cuit according to the mobility of the material. This phenomenon is known as charge collection. The amplitude of the signal read out by the circuitry is proportional to the charge collected by the pixel and how fast it is collected. The silicon is depleted with a voltage in order to increase its charge collection properties. The higher the voltage the faster the charge collection, and the larger the charge. Finally, it is pixelated (segmented into little squares) that give it the characteristic name of pixels. Each pixel is read-out independently to gain granularity.

4.3.1 Monolithic Active Pixel Sensors

Complementary Metal-Oxide-Semiconductor (CMOS) technology is an industrial process that allows the realization of integrated circuits containing two polarities of Metal

Oxide Semiconductor (MOS) transistors, patterned on the same chip. Silicon technology allows to selectively dope a substrate, creating a large number of *p-n junctions* and thus creating a segmentation of the detector.

Pixel detectors can be divided into two categories: Hybrid Pixel Detectors (HPD), where a dedicated front-end chip is interfaced to the sensor, and Monolithic Active Pixel Sensors (MAPS), where a single chip integrates the sensitive matrix and the readout electronics. High resistivity substrates compatible with CMOS technology have enabled the development of Depleted-MAPS (DMAPS) in which the substrate is highly biased allowing for fast charge collection compatible with the needs of the HEP experiments.

4.4 Radiation effects in silicon detectors

When interacting with the silicon sensor material, the energy loss of highly energetic particles does not result exclusively in the generation of electron-hole pairs producing the electrical signal. They also produce the displacement of nuclei out of their lattice position. As discussed before, the interaction of radiation with matter can occur with the electrons of the silicon lattice, or with the nuclei. Given the exposure of the silicon sensors to different types of particles in the centre of the experiments (photons, electrons, protons, neutrons, and other hadrons). Radiation damage effects are usually divided into those derived from the Total Ionizing Dose, those from Non-Ionizing Energy Loss, and those that lead to Single Event Effects [19] [20].

4.4.1 Total Ionizing Dose

Total Ionizing Dose (TID) accumulates with the exposition to radiation. TID is measured in Gray, where 1 Gray is 1 J/kg, or expressed in Radiation Absorbed Dose (RAD) 1 Gray is 100 rads.

$$1\ \text{Gy} = 1\ \frac{\text{J}}{\text{kg}} \tag{4.3}$$

The leakage current of the device increases in transistors due to the degradation provoked by charges trapped inside the isolation layer. This change affects the threshold voltage and can give rise to leakage currents between drain and source of NMOS transistors and in between neighbouring transistors. Smaller size transistors show reduced

sensitivity to TID [19].

4.4.2 Non Ionizing Energy Loss

The Non-Ionizing Energy Loss (NIEL) is a quantity that describes the rate of energy loss due to atomic displacements as a particle traverses a material. It is responsible for the creation of defects in the crystal lattice changing its properties, it can change the doping concentration and even the type inversion. There is a loss in sensor performance due to the charge collection lower efficiency and it also results in increased leakage current [21]. Sensor gain would be affected, and the threshold should be adjusted to get the same efficiency. This will be explored in the different process modifications in MALTA pixels

4.4.3 Single Event Effects

Single Event Effects (SEE) are caused in the digital electronics due to the Ionizing radiation in the electronics. There are two main types of SEE: the Single Event Upset (SEU) and Single Event Latchup (SEL).

A Single Event Latchup is a destructive event on which a parasitic structure, equivalent to a thyristor, can short circuit the system drawing a large current which can destroy the circuit by thermal effect.

A Singe Event Upset (SEU) happens when a digital circuit, usually a memory cell, is disturbed by the charge generation from a passing ion to the point of changing logic state [22]. Although a SEU is not permanent, and can be undone by a reset, a bit flip can cause an important effect in the data taking.

4.5 MALTA family of monolithic pixel detectors

The Monolithic from ALICE To ATLAS (MALTA) is a large CMOS sensor designed to meet the ATLAS requirements and High Luminosity LHC and for future HEP experiments [23][24] fabricated in the TowerJazz 180 nm CMOS process on a 25 μm or 30 μm epitaxial silicon on top of a high resistivity wafer. It contains a matrix of 512x512 pixels of 36.4x36.4 μm^2 size, with a total chip size of around 2x2 cm^2. There is an smaller-size sensor called Mini-MALTA [25] with a matrix of 16x64 pixels of the same size.

Fig. 4.5 shows the layout of MALTA with a pixel matrix divided in 8 sectors with different front-end configurations. The larger portion of the chip is the pixel matrix, the periphery of the chip contains blocks necessary for the chip operation, clock, control and read-out.

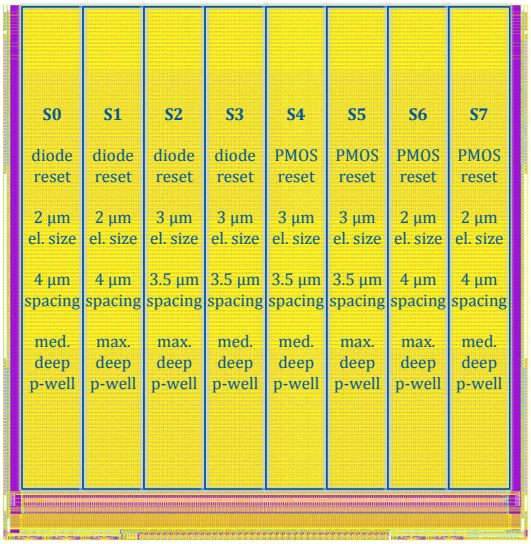

Figure 4.5: Layout of the MALTA chip with matrix divided in 8 sectors

Fig. 4.6 shows the layout of the pixel circuit with the separated analog front-end, the digital part and collection electrode.

The digital address and timing information of hit pixels is transmitted off-chip through a 37-bit parallel output, which uses either a low-voltage differential signal (LVDS) standard or a full-swing 1.8 V CMOS standard, designed to operate up to 5 Gb/s ensuring robust data transmission. MALTA is also designed to be daisy chained, the output of one MALTA is connected to the next, and read-out is performed from the end of the chain.

The slow control is a block that controls the operation of MALTA, it is divided into a core finite state machine, and the internal 16-bit register pool. The internal register pool holds the configuration for the registers, and is not directly accessible to the user. These registers have a default value after reset. The finite state machine core is interfaced through a serializer/deserializer in order to read or write into the register pool.

Fig. 4.7 shows the layout of the Mini-MALTA chip. The read-out of mini-MALTA

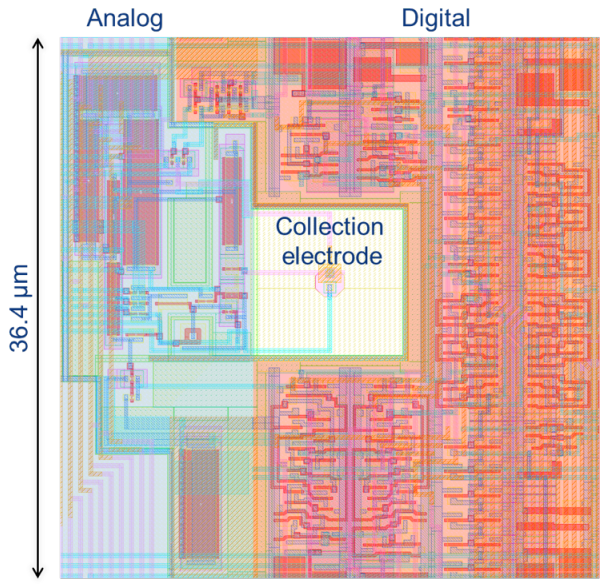

Figure 4.6: Layout of the MALTA pixel

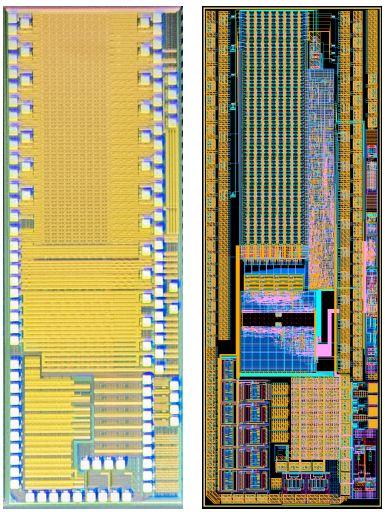

Figure 4.7: Picture (left) and layout (right) of the Mini-MALTA chip

contains a FIFO and a serializer with 8b/10b encoding, a 640 Mbps serialized output, and a 40 Mbit/s debug output. The slow control of mini-MALTA is based on a shift register.

Both MALTA and Mini-MALTA sensors, have pixel matrix divided in sectors with different fabrication processes which aim to study radiation hardness to NIEL and efficiency of the sensor. Fig. 4.8 shows the cross-section of the different processes used

in the sensors. On the top left it shows how detection efficiency is affected by diffusion in the original ALICE process. The top right shows the standard process with a continuous low dose n-type layer. The bottom left shows the process with the addition of a gap in the low dose n-layer through a mask change (n-gap). The bottom right shows the process of adding an extra deep p-type implant (called extra deep p-well). The aim of all these modifications is to have a larger gradient of the electric field lines in the substrate so that the charges produced there can drift quickly into the collection electrode in order to detect the hits. Mini-MALTA has increased size transistors to address the RTS noise, and increase the front-end gain. These are roughly 2.3 times larger than in the standard MALTA front-end.

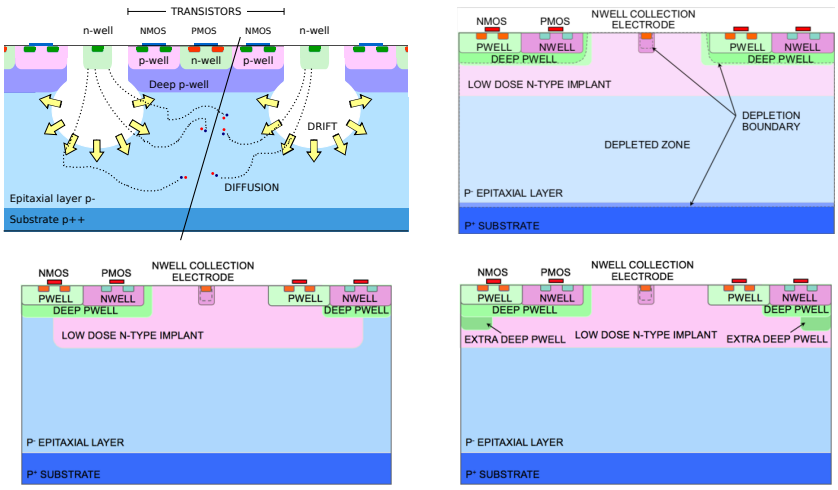

Figure 4.8: TowerJazz process cross section. Top left: standard process. Top right: continuous n-layer. Bottom left: n-gap or low n-implant removed at the edge of the pixel. Bottom right: extra deep p-well at the edge of the pixel. [23]

Fig. 4.9 shows the readout system used to characterize MALTA sensor which is very similar to the one for the Mini-MALTA sensor. On the bottom of the picture there is a high density 10 layers MALTA chip carrier board interfaced with a VIRTEX VC707 [26] or a Kintex KC705 [27] FPGA evaluation board. They are connected using a FPGA Mezzanine Card (FMC) connector. Fig. 4.10 shows a close picture of the Mini-MALTA assembled to the carrier board using gold wire-bonds.

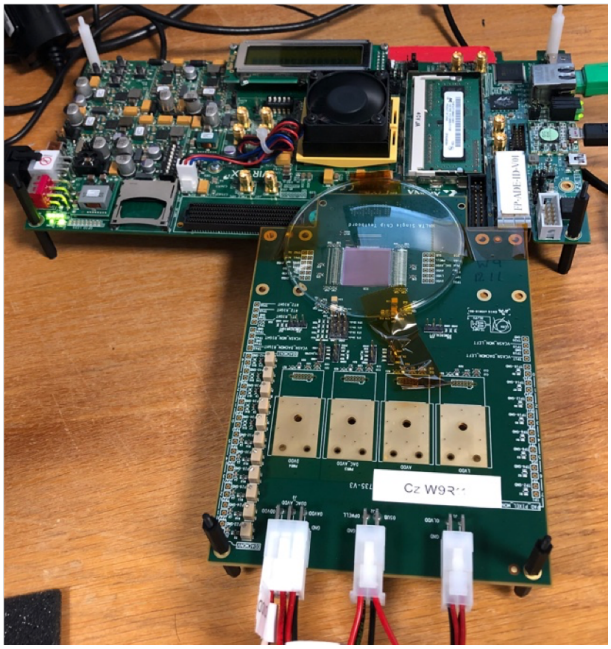

Figure 4.9: MALTA carrier board interfaced with a VIRTEX VC707 FPGA

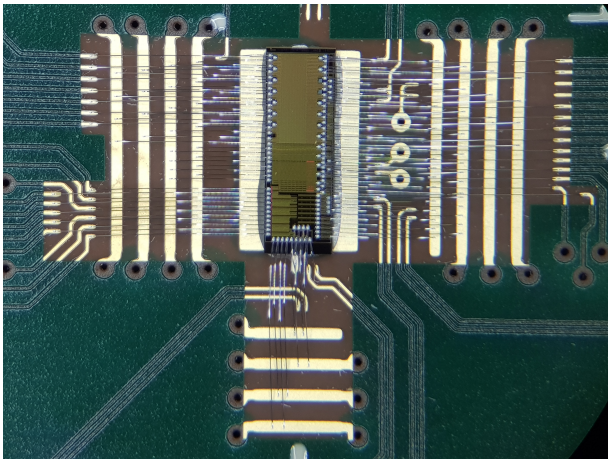

Figure 4.10: Picture of the Mini-MALTA chip wire-bonded to the carrier board

4.6 Sensor characterisation parameters and beam tests

4.6.1 Signal-to-Noise, efficiency and threshold

Besides the generation of a large signal from the energy deposition, a high signal-to-noise ratio (SNR) is an important parameter for the pixel detectors. In pixel sensors, it is usually expressed as equivalent noise charge (ENC), expressed as the ratio of produced

noise over the signal generated from a single collected electron.

$$ENC = \frac{V_{NOISE\_OUT}}{\mathrm{V_{OUT\_1e^-}}} \left[\frac{V}{V/e^-} \right] \tag{4.4}$$

The efficiency (ε) of a sensor is also an important parameter which is expressed as the number of detected (N_{det}) in the DUT divided by the number of total (N_{total}) particles in a reference detector in a given time window.

$$\varepsilon = \frac{N_{det}}{N_{total}} \tag{4.5}$$

The resolution of a detector σ_p has a direct dependence on the pixel size p. The resolution of a single pixel is given by

$$\sigma_p = \frac{p}{\sqrt{12}} \tag{4.6}$$

The threshold at which the chip is set to operate is the most important factor in the efficiency. The threshold should be a low as possible to improve the detection efficiency but high enough to reduce the hits generated by the noise on higher sensitive pixels.

4.6.2 Beam tests results

Beam tests consist of measuring the DUT with a beam of particles usually measured with the help of a multi-plane read-out system. Fig. 4.11 shows a photograph of a telescope in front of the beam line in the Super Proton Synchrotron (SPS) H6 beam-line in the north area at CERN.

Fig. 4.12 [25] shows the efficiency maps of a non-irradiated Mini-MALTA sensor, on the left and after 1x10^{15} MeV n_{eq}/cm^2 irradiation on the right. The measurements were taken at -20°C and operated at -6V, with a low threshold of 200e$^-$ on sectors with enlarged transistors in the front-end and 380e$^-$ for the standard size. White bins are noisy pixels on which efficiency has not been calculated. The performance of the different pixel configurations shows the different radiation damages.

Before irradiation (left map), the average efficiency of enlarged transistors is 99.6 ± 0.1%. On the sectors with standard transistors we can already observe lower efficiency: in the top 99.1 ± 0.1% for the modification with gap in the n-layer, in the middle 98.9 ± 0.1% for the extra deep p-well modification and in the bottom 97.9 ± 0.1% for

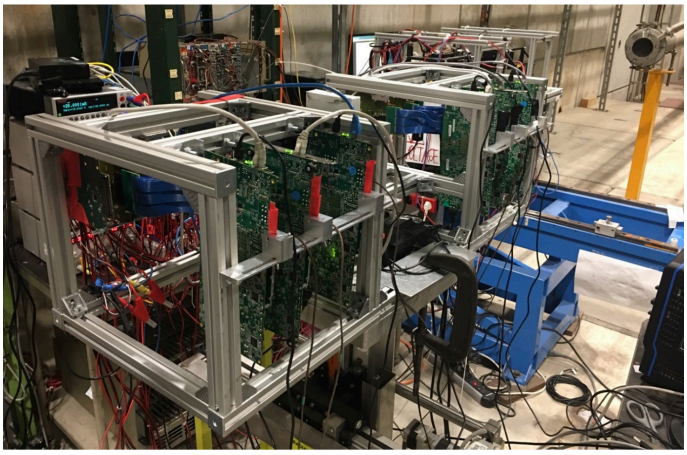

Figure 4.11: Telescope in the beam line of CERN SPS

continuous n-layer.

On the right map shows the efficiency maps after 1x10^{15} MeV n_{eq}/cm^2 neutron irradiation. Sensor regions with enlarged transistors (on the left) have higher efficiency with respect to standard transistors: 91.9% in the region with continuous n-layer, 97.9% with extra deep p-well and 97.6% with n-gap modification. There is larger decrease in efficiency, which is still observed in the regions around the pixel corners, in standard transistors regions due to the lower gain and high threshold (380e$^-$) regardless of the modifications. Efficiencies are: 78.8% in the continuous n-layer, 87.0% in extra deep p-well and 86.5% in n-gap modification.

Fig. 4.13 [25] shows the efficiency as a function of threshold at 1x10^{15} MeV n_{eq}/cm^2 irradiated Mini-MALTA [25]. As expected, the lower the threshold the higher the efficiency, reaching approximately 95% for continuous n-sectors with enlarged transistors and 98–99% for sectors with n-gap or extra deep p-well. These measurements highlight the improvements achieved in the sectors with new large transistors, and process modifications (n-gap and extra deep p-well).

4.7 Single Event Upset test chip

A dedicated test structure dubbed SEU_TJ180 was designed along with the first MALTA version with the purpose of studying the effects of SEUs in Towerjazz 180 nm memories [28] which are the ones used in the MALTA and MiniMALTA designs [29]. Fig. 4.14 shows the layout of the SEU_TJ180 chip. On the top left, there is a a sixteen

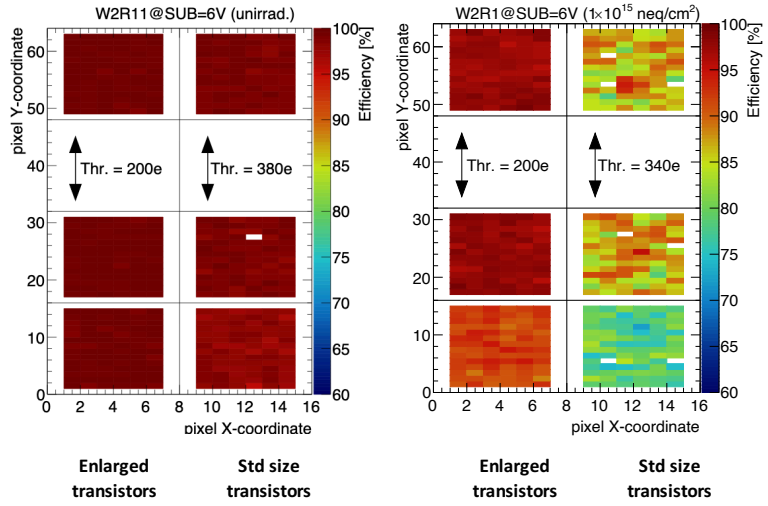

Figure 4.12: Efficiency of Mini-MALTA as a function for the track position. Left is non-irradiated, right after irradiation at 1x10^{15} MeV n_{eq}/cm^2

Signal	**Function**	**#Bits**	**Dir. (from chip)**
DATAIN	Input data	16	Input
ADDRESS	Address and memory selection	15	Input
DATAOUT	Output Data	16	Output
CLOCK	Clock	1	Input
BROADCAST	Broadcast (all memories)	1	Input
WRENB	Write Enable	1	Input
OENB	Read Enable	1	Input
SHIFT	Shift data	1	Input
RESET	Reset	1	Input
MUXSEL	Select data	2	Input

Table 4.1: SEU_TJ180 data bus and controls signals.

single-port RAM (SPRAM) block containing an array of 16 single port RAM memories (SPRAM) 1024@16 bits. On the top right, there is an array of 8 dual port RAM memories (DPRAM) 2048@16 bits. On the bottom there is a shift register which is 2048 cells long and 16 bits wide.

The SEU_TJ180 chip has a bus digital interface of 16 lines for data input, 15 lines for address and 16 for data output. All three blocks use the same 16 bit input lines. The SP_RAM and the DP_RAM blocks share the same control lines. The SP_RAM, the DP_RAM and the shift register share the input data lines and clock signal. The selection of the memories is based on a multiplexer managed by two bits. The list of signals used to operate the chip is shown in table 4.1.

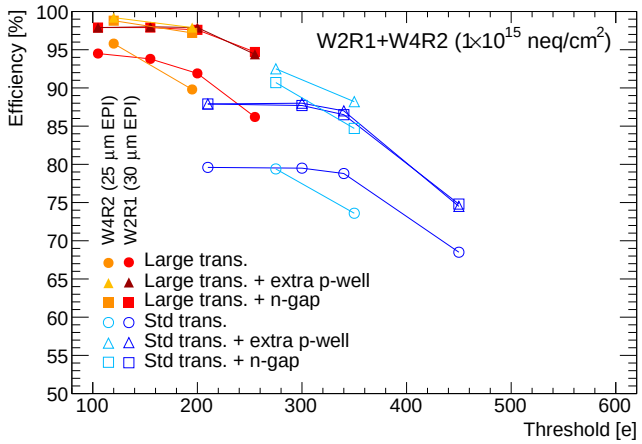

Figure 4.13: Efficiency as a function of threshold mean for neutron irradiated Mini-MALTA samples at 1x10^{15} MeV n_{eq}/cm^2 measured with a 2.5 GeV electron beam at ELSA in 2019. Sensor regions represented by colors. They have different epitaxial layer thicknesses: 25 µm (orange or light blue symbols) and 30 µm (red or dark blue symbols) [25].

Fig. 4.15 shows the diagram of the shift register, it is a chain of flip-flops sharing the same clock, in which the output of each flip-flop is connected to the data input of the next flip-flop in the chain. At each transition of the clock it shifts the data in the data present at its input and shifting out the last bit in the array. The Shift Register block has 2048 stages of 16 bits, for a total of 32 Kbits of memory. A dedicated read-out system for beam tests is designed and explained in Chapter 5.3.

4.8 Conclusions

This chapter has given an overview of the pixel sensors technology in high energy physics. The MALTA family of pixel detectors has been introduced. It is a radiation hard sensor able to reach efficiencies of 98% after irradiation at 1x10^{15} MeV n_{eq}/cm^2 with only 300 electrons of threshold. This results in a very low power consumption for a high efficiency. The SEU_TJ180 is a chip designed to study the radiation effects in the memories technology used in the MALTA family.

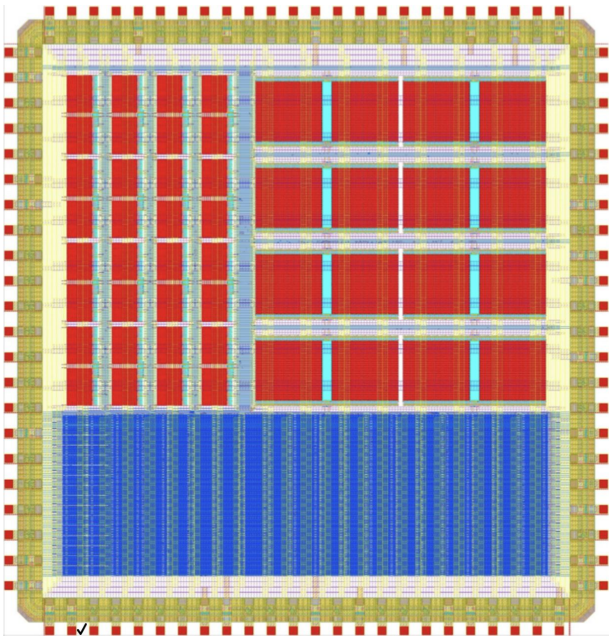

Figure 4.14: Floorplan of the SEU_TJ180 chip

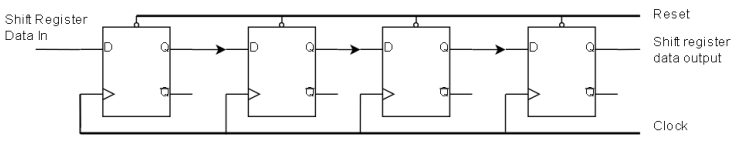

Figure 4.15: Diagram of the Shift register interconnection

Chapter 5

Control and Monitoring systems in Physics

5.1 MALTA beam telescope

Beam telescopes are tracking detector systems used for the characterization of pixel detector prototypes. Particles passing through to the telescope are reconstructed and used in the characterisation of a given device under test (DUT).

Fig. 5.1 shows the basic diagram of a beam telescope setup which usually consists of two arms around one or more DUT sensors. Each arm has one or more reference planes used to reconstruct the tracks which are interpolated into intercept positions on the DUT(s). Typically, telescope planes are not self-triggering and often, beam telescopes use a fast response detector such as a scintillator connected to a photo-multiplier, with a fast rise time to trigger the read-out of the telescope planes.

The particle beam passes through the scintillators, planes and DUT(s). A correct geometric alignment of the telescope components is necessary to ensure the accuracy on precision measurements. This is done by minimizing the distance from hit to track path (residuals) during the track reconstruction. Track reconstruction is a computing intensive process, in which all the recorded hits during an event are probed to match the path of the incident particle following the physics processes described in Chapter 4. The software package used for MALTA telescopes includes Proteus [30].

The resolution of the telescope is the uncertainty of the track position extrapolated

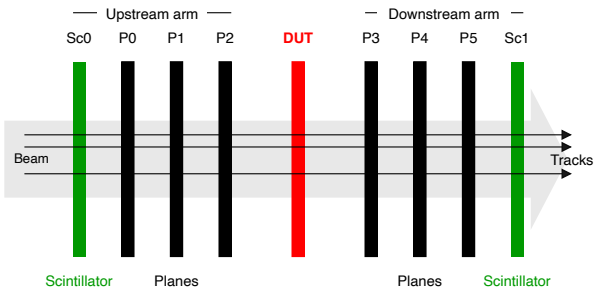

Figure 5.1: Diagram of a beam telescope with one DUT and two scintillators

to the DUT plane. Several factors affect the performance of a telescope, the distance among the planes, the thickness and pitch of the reference sensors and the beam properties. Generally, sensors with smaller pixel pitches and higher beam energies provide better resolution.

At high energies, such as the ones generated in the SPS H6 beam-line at CERN with 180 GeV pions/protons beam, the multiple scattering (θ_{ms}) of particles is minimal therefore particle trajectories can be approximated with a straight line. But at lower energies, such as 4 GeV electrons provided in DESY (Hamburg) and ELSA (Bonn), the scattering effects are larger and the usage of a track reconstruction algorithm is required. In this case General Broken Lines (GBL) framework [31] is used.

Fig. 5.2 shows a sketch of a telescope built using planes with MALTA sensors [25]. It consists of two optional scintillators, up to 3 planes with a 100 µm thick epitaxial MALTA sample on each arm and the DUT(s) usually placed inside a cold box in the center. Table 5.1 shows the simulated residuals on the DUT with the Allpix Squared framework [32] at different distance between the planes predicted for the scattering effects of two beams. At 180 GeV pions beam the predictions show a 4 µm without any corrections and a better performance with closer planes at 3 GeV electron beam. This confirms how for the same telescope configuration pions beam show better performance than electrons beam; and for an electrons beam it is necessary a telescope configuration with smaller distances among planes.

5.2 Trigger Logic Unit

A Trigger Logic Unit (TLU) is responsible for providing a common trigger for the Data Acquisition (DAQ) and the synchronization of the telescope elements including the

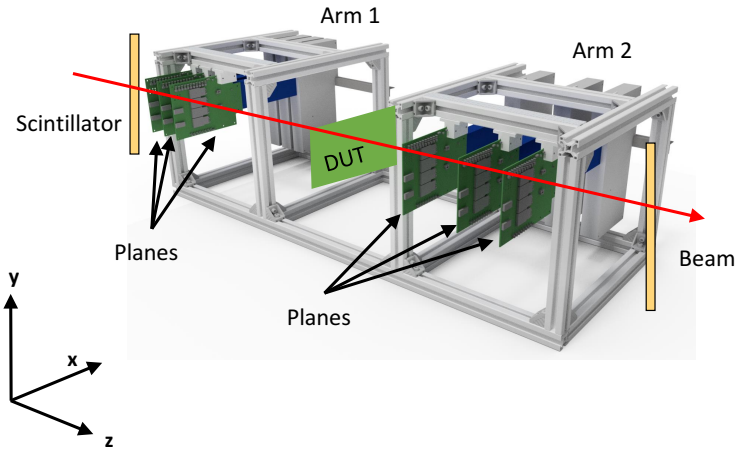

Figure 5.2: Sketch of a beam test telescope with 6 planes and 2 scintillators

	Pions 180 GeV	Electrons 3 GeV		
Plane	Position [cm]	Position [cm]	Position [cm]	Position [cm]
1	0	0	0	N/A
2	7	7	2	0
3	15	15	4	2
DUT	39	39	6	4
4	65	65	8	6
5	79	79	10	8
6	85	85	12	N/A
Residual	8 µm	87 µm	16 µm	17 µm

Table 5.1: MALTA telescope Allpix simulated residuals for 180 GeV pions and 3 GeV electrons beam.

DUT(s). It requires one or more input fast signals from the trigger detectors, that can be the actual detector planes or dedicated scintillators connected to photo-multipliers and discriminator electronics as mentioned before, it processes the signals and using a combination logic, it ignores or propagates the trigger to the read-out planes as a single accept signal (L1A). The hits which are not associated with a L1A signal are not recorded.

The former TLU used for the MALTA telescope was based on NIM (Nuclear Instrumentation Module) technology. Fig. 5.3 shows the NIM TLU in its crate. The operation of the NIM TLU requires the manual arrangement of many cables to configure parameters making the process a complex and highly time-consuming task. Further-

more, it is a heavy set of hardware unfit for travelling and it has a high cost.

NIM logic is a current-based active low logic with a negative *true* (at -16 mA into 50 ohms = -0.8 V) and 0 mA for *false*. Fig. 5.4 shows the operation scheme of the TLU with the NIM logic. The TLU accepts trigger signals from each plane and DUT(s) into an inverter, necessary for NIM logic, then signals are sent into a discriminator and then into a coincidence module on which the combination logic is defined by the configuration of the cables. The coincidence module also accepts a veto signal to reduce the coincidence rate generated by the time delay module at the output of the coincidence rate. Finally, the accepted L1A signal is sent to a fan in/fan out where it is duplicated and shifted to the right voltage in the level adapter module and propagated as L1A trigger signal to the telescope planes.

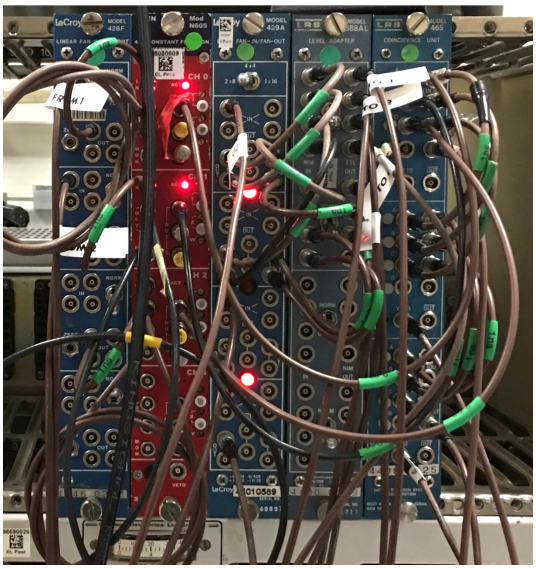

Figure 5.3: Front picture of the NIM logic based TLU. From left to right the modules are: inverter, discrimator, fan in/fan out and coincidence

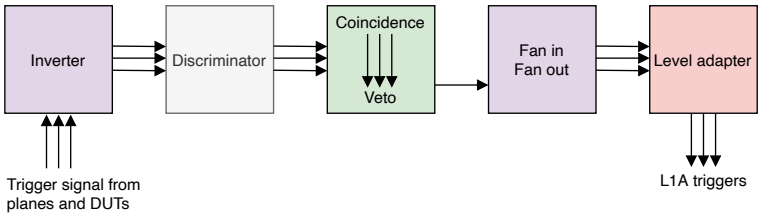

Figure 5.4: Block diagram of the NIM logic TLU

Field programmable logic technology (FPGAs) can be used to build a new TLU

more portable for the test-beam campaigns, reduce cost and weight and improve features and trigger control with the ability of software configuration. The flexibility of the NIM design that allows any trigger logic combination to be wired in a matter of minutes, is compensated with a highly portable device that can only be programmed by an FPGA expert. The challenge is to produce an application for an FPGA that is flexible enough to implement any trigger logic combination through software and achieve the following minimum acceptable requirements which have been addressed in the MALTA TLU:

- Number of input channels: a minimum of 4 input channels with at least one scintillator signal
- Maximum input rate per channel: at least 100MHz
- Length of input signal: a few ns
- Output length: a few ns (programmable)
- Maximum output rate: at least 10MHz (programmable)
- Number of outputs: a minumum of 6

5.2.1 The MALTA TLU

The new MALTA TLU is shown in Fig. 5.5. It is based on a Kintex-7 KC705 evaluation board used to process the combination logic and provide on-line monitoring. The TLU is interfaced using SMA connectors to the planes and scintillator through two custom SMA to FMC converter cards [33]. One is used for input signals and the other for output signals. Ethernet port is connected to the network for configuration and monitoring. A USB port is used for firmware programming onto the FPGA. All this connections between the telescope and the TLU are shown in the diagram in Fig. 5.6.

Input processing module

The MALTA TLU is designed to accept a range of input signal shape provided by LVCMOS_25 standard of the Kintex. As the input signals are supposed to be asynchronous, the first step is a signal processing block that captures the signal with the

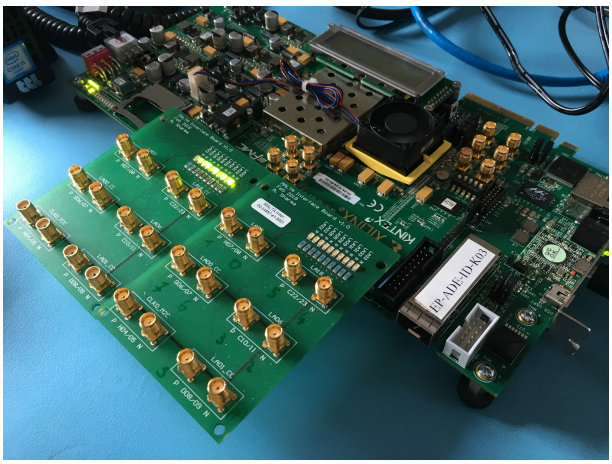

Figure 5.5: Picture of the MALTA TLU with two SMA to FMC cards

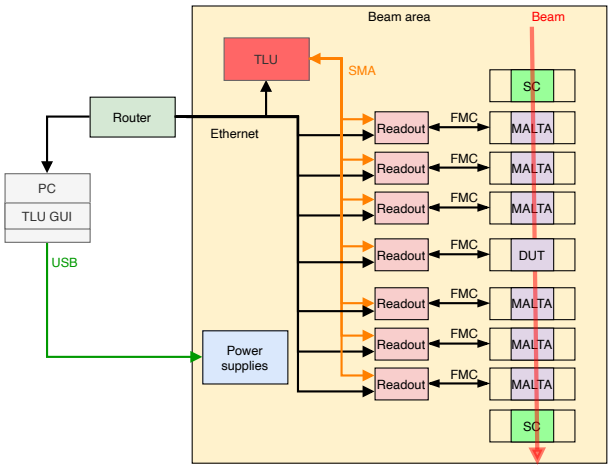

Figure 5.6: Diagram of the MALTA telescope and the TLU

internal 320 MHz clock. There is one module for each of the input signals and the goal is to transform it into a standard shape for the subsequent processing. This includes the stretching to a programmable length and the implementation of a possible veto window to avoid too close signals. The module contains a 32 bit counter to monitor the input rate of each channel.

Coincidence module

The coincidence is performed passing the individual channels by an AND gate. The list of channels to consider is fully configurable. The width of the signal from the previous

step, that is before the coincidence, acts as a coincidence window in the combination step. This window is necessary due to the non-digital nature of the signal from the MALTA planes on which the arrival time of the hits are proportional to the charge deposition. As such, the input signals are spread by typically 5 to 15 ns. This is observed in Fig. 5.7, which shows the L1A rate as a function of the stretched window width of the signals from the planes in ns. The longer the duration of the planes window the higher the opportunity for the coincidence logic to form a L1A trigger. A saturation effect is produced after around 25 ns because hit signals are ignored during the long stretched processed signals.

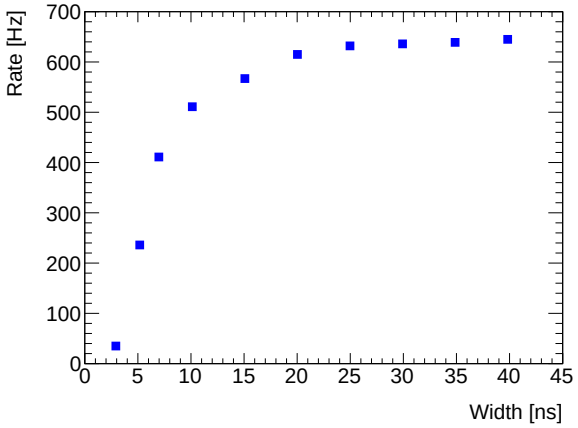

Figure 5.7: L1A rate with a source of Sr-90 as function of planes signal stretched width in ns

Output processing module

The output processing module is similar to the input processing and it allows to fully shape the output signal. The capability to control the output signal length is important to interface the TLU to the devices receiving the trigger while the veto is used to implement a maximum output rate. It also contains the total trigger counter counter.

Treatment of input scintillator signal

The scintillator allows the TLU for precise timing measurements. The coincidence of MALTA planes has a time resolution of several ns but basing the timing reference on a scintillator ensures a sub ns precision. It is important to note that the usage of

the asynchronous scintillator signals to the clock also introduces a jitter of the order of the clock to which it is introduced. For this reason, a special treatment is given to the scintillator signal. The coincidence of the signal from the telescope planes is used to create an enable window and such signal is logically summed (AND) with the scintillator signal and directly sent to the output to preserve the scintillator timing.

Fig. 5.8 shows the timing of the signals. The hits fasts signals are processed (in blue) and combined (coincidence entry) to form a L1A signal. When the combination logic is met, the a L1A is formed and a busy window on which no coincidences are accepted. In the case of this figure, the combination requires signal from the scintillator and the two planes. The L1A is sent to all the elements of the telescope including the DUT(s). The current hardware of the TLU allows sending L1A up to 10 devices.

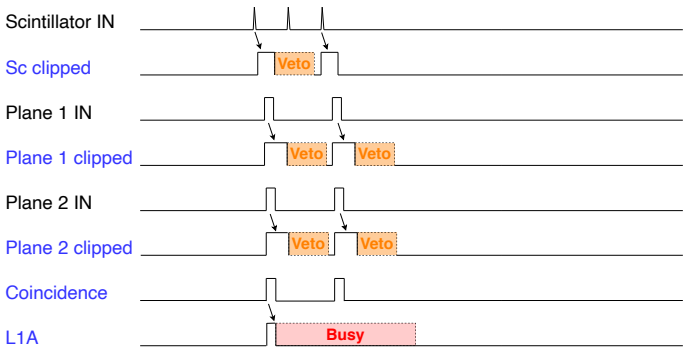

Figure 5.8: Diagram showing the timing of the signals and combination logic in the TLU

5.2.2 Architecture

Fig. 5.9 shows a basic diagram of the firmware written in VHDL. The Gigabit Ethernet port is controlled using the IPbus protocol [34] for readout communications, control and configuration. Two clocks are generated from the FPGA internal clock, one for IPbus running at 40 MHz and other for the input, output and processing modules at 320 MHz. The TLU core accepts analog asynchronous input signals from the FMC connector that are asserted synchronously with the TLU clock into the Input module that streches the signals and applies the vetos from the processing module. Their parameters such as signal width and veto window can be accessed from IPbus memory registers individually for each plane. The Coincidence module is in charge of the formation of a L1A signal. The coincidence logic can be also modified from the network

Address	Bits size	Description
0x32	1	Enable scintillator
0x3F	31	Firmware version
0x42	4	Planes to listen trigger
0x43	4	Planes to provide L1A
0x46 to 0x4F	20	Veto time
0x50 to 0x59	32	Counters
0x59	1	Start / stop run
0x5C	1	Reset counters
0x5D to 0x63	20	Trigger signal width

Table 5.2: TLU addresses of IPbus registers.

by the user as a set of binary options that can be enabled/disabled corresponding to each of the planes. The Output module processes the L1A signal to have a configurable width and maximum trigger rate. Each module has a counter. Table 5.2 shows the list of IPbus registers used for configuration and monitoring.

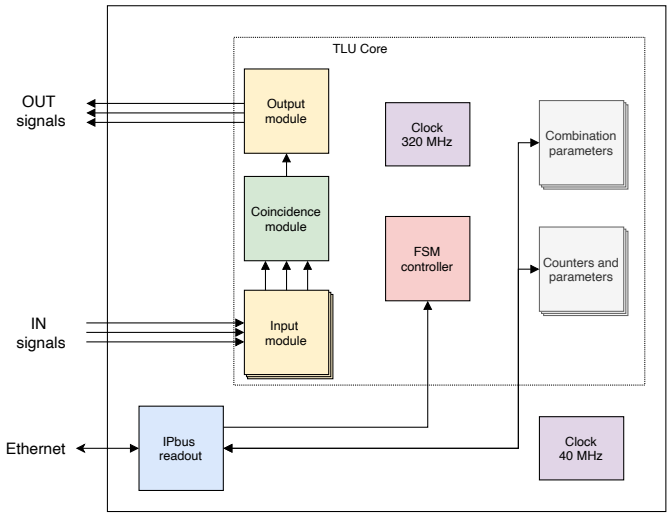

Figure 5.9: Block diagram of the TLU's firmware

5.2.3 Run operation

The telescope run can be operated and monitored over Ethernet using the TLU Graphical User Interface (GUI) shown in Fig. 5.10. The baseline is a C++ class in charge of communication with the FPGA using IPbus. This class contains all necessary methods to set the TLU configuration using 32-bit IPbus registers shown in Table 5.2. This class

can be used from telescope software framework and from the TLU GUI using a python wrapper. A basic terminal tool is also available for quick access. The upper panels allow the configuration of trigger planes, veto, width, L1A and connection settings. The middle panel has the start and stop of the run. The lower panel is used to monitor the number of triggers of planes and L1A. The lower text area is intended for debugging purposes

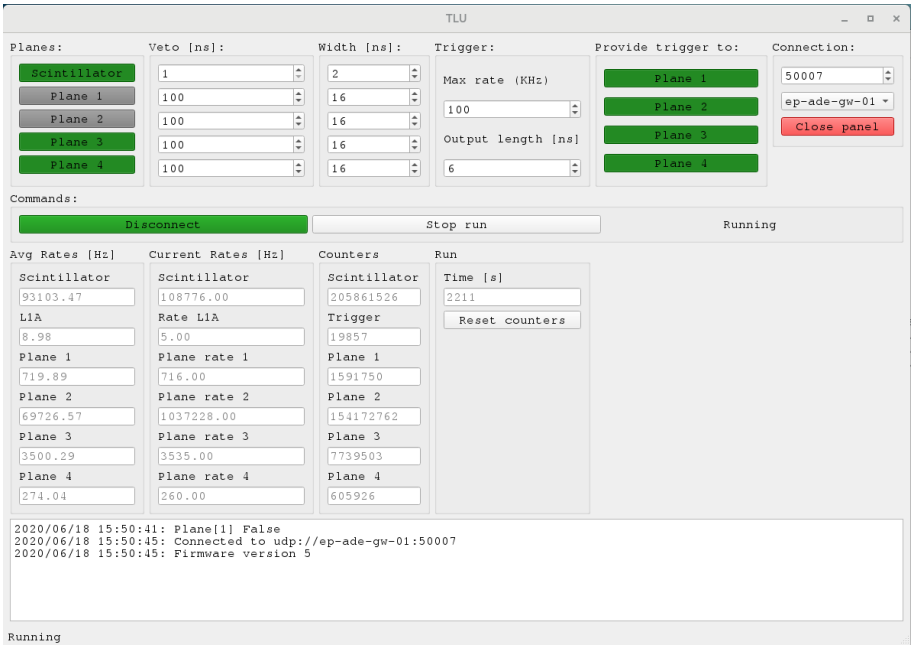

Figure 5.10: TLU GUI during operation.

The TLU GUI allows the configuration of the telescope setup to select the number of planes, scintillator and DUT(s). It provides full control over the telescope run and adjustable settings are: connection parameters, control of the telescope run (stop, start, pause), enable or disable input and output planes, set veto duration and width of each plane signal as well as maximum trigger rate. It displays the trigger rate and counters for input plans and L1A trigger. Fig. 5.11 shows the possible states in the Finite State Machine (FSM) and the commands to change state.

5.2.4 Beam tests and results

Fig. 5.12 shows the data acquisition using 3 planes and one DUT (shown as plane 2). The row on the top shows the hit map of each plane with a squared ROI. The middle

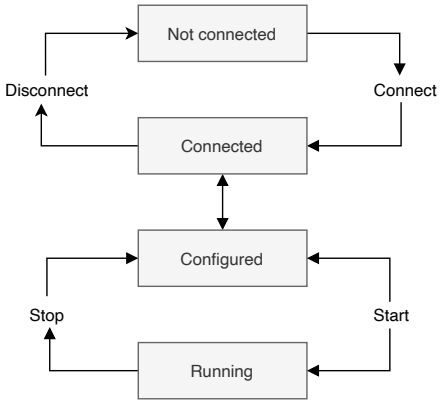

Figure 5.11: Block diagram of the TLU's FSM

row shows the number of hits as a function of time of arrival since the L1A in ns. The bottom row shows the number of hits as a function of the number of pixel per event.

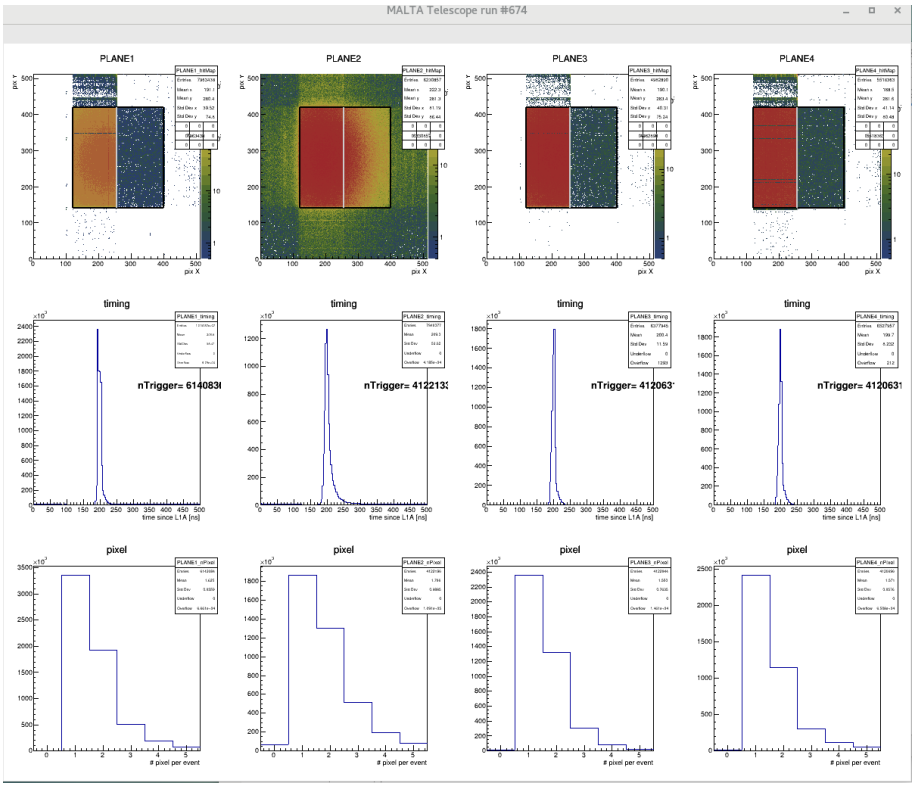

Figure 5.12: Telescope data acquisition using the MALTA TLU

The MALTA TLU has been used during the beam tests campaign at DESY to characterize the MALTA and MiniMALTA sensors achieving a spatial resolution of 12 µm

with a beam of electrons at 3 GeV energy. Fig. 5.13 shows the resolution of the telescope with MALTA planes with MALTA TLU. The two plots on the top show a resolution achieved with cosmic rays of σ=18µm for the X axis and σ=14µm for the Y axis. On the bottom, a resolution of σ=12µm on both axis with a beam of electrons at 3 GeV energy at DESY.

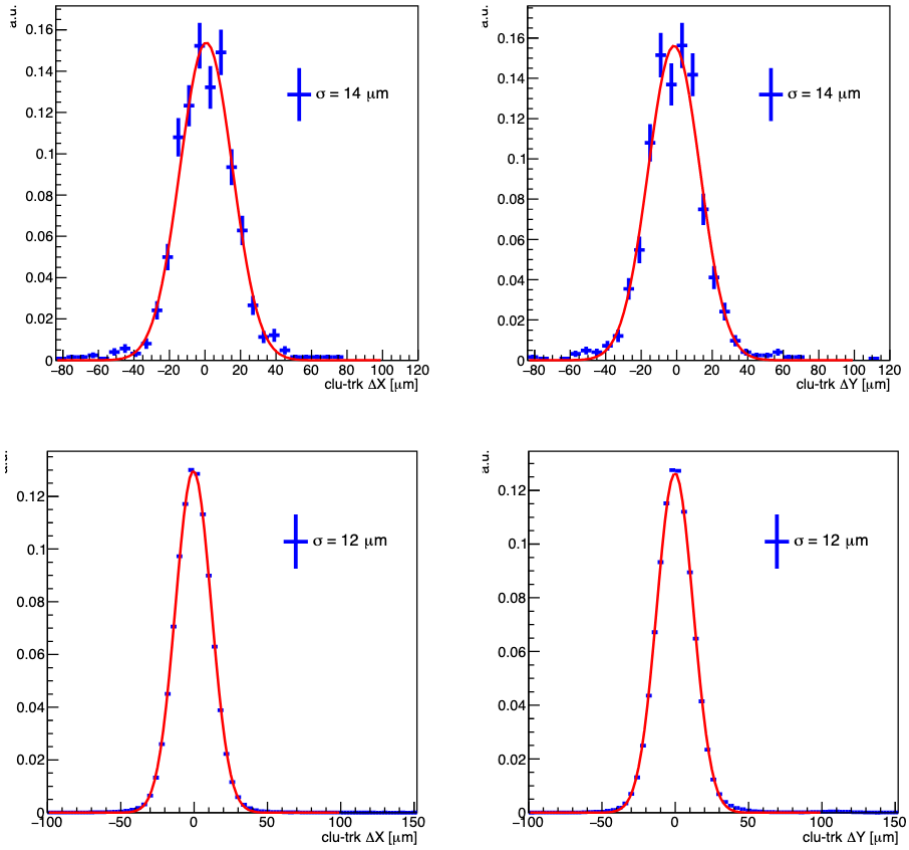

Figure 5.13: Telescope resolution based on track residual distributions. Top: measuring cosmic rays. Bottom: beam of electrons at 3 GeV energy

Fig. 5.14 shows the difference in time of the fastest hit of the cluster, matched with the track in the DUT, and the time of the hit in the scintillator. The DUT for this measurement is a non-irradiated MALTA with Czochralski silicon and the source is Sr-90.

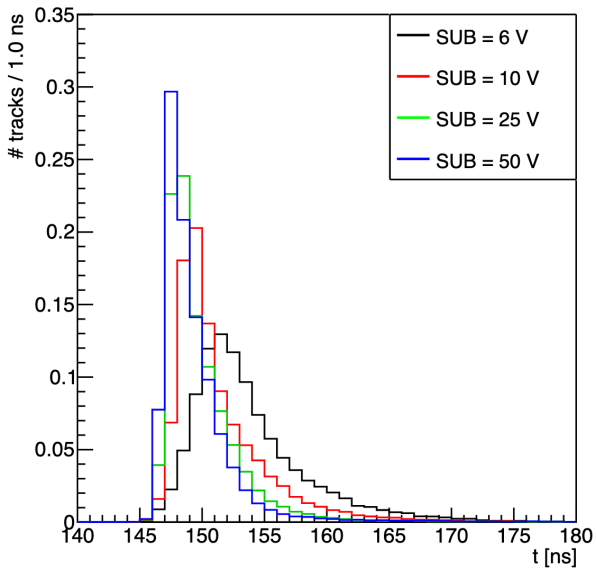

Figure 5.14: Difference in time between the scintillator and the fastest hit of the cluster in the DUT. Colors indicate bias voltage

5.3 Single Event Upset

The SEU_TJ180 was introduced in 4.7. It is a prototype chip designed to evaluate the sensitivity of different types of TowerJazz 180 nm memory cells technology to SEUs during and after irradiation. An SEU is a change of state in memory cells or registers in microelectronic devices caused by ionizing particles.

The methodology to test the SEU sensitivity of the TowerJazz technology consists of exposing the SEU_TJ180 chip to a heavy ions beam while monitoring the bit flips as a function of the time of exposure and particle flux. The SEU cross section σ in $cm^2/_{bit}$ is calculated as

$$\sigma = \frac{N_{SEU}}{N_{bits} \cdot \Phi \cdot t} \tag{5.1}$$

where Φ is the is the fluence of the beam expressed in number of particles per cm^2 and per second. During irradiation, data is send to the chip and read-out after a given time to be checked for bit flips.

Fig. 5.15 shows a diagram of the testing setup built to test the SEU_TJ180 chip in a beam facility. It consists of a chip assembled into a carrier board that powers the chip and it is interfaced to a Xilinx Kintex KC705 FPGA evaluation board. A firmware configures the FPGA to operate the chip with instructions sent over Ethernet from a PC outside of the beam area.

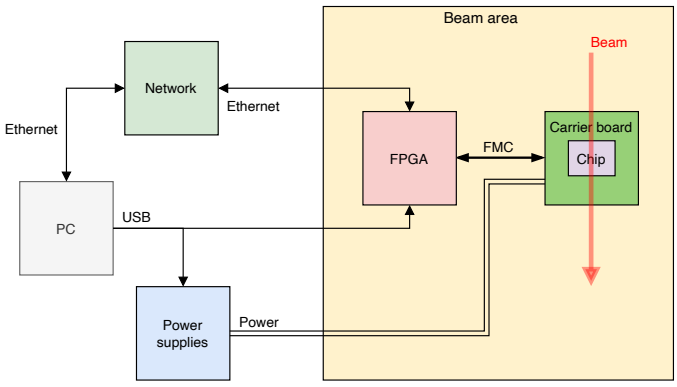

Figure 5.15: Diagram of the SEU_TJ180 testing setup

5.3.1 Read-out system

A 5 layers PCB carrier board [35] has been designed and produced to communicate with the SEU_TJ180. Fig. 5.16 shows a picture from the top of the SEU_TJ180 car-

rier board. The chip occupies the top region on the top layer, away from rest of the components to avoid the proximity of the beam. On the bottom layer there are 10 µf and 10 µf decoupling capacitors next to the power pads of the chip. A total of 8 level shifters with 100 µf decoupling capacitors are allocated on the top layer in a row to ensure the adaptation of voltages between the SEU_TJ180, designed to operate at 1.8 V and the Kintex-7 KC705 evaluation board operating at 2.5 V. The FMC connector is at the bottom underneath.

Figure 5.16: Picture of the SEU_TJ180 carrier board

Separated planes ensure independent powering of the level shifters and the chip from external power supplies using the connectors on the right. There are two separated ground planes for the PCB and FMC. Coupling between FMC and PCB grounds and between power planes of chip and level shifters is available via W1 and W2 jumpers. The traces that connect the chip to the FMC along the PCB are carefully balanced to avoid delays between them. M3 mounting holes are intended for stage mounting and chip cover.

The SEU_TJ180 has 92 pads of 57×57 μm^2 as explained in Chapter 4.7. Fig. 5.17 shows the wire-bonding schema.

Fig. 5.18 shows a basic diagram of the firmware written in VHDL. The Gigabit Ethernet port is controlled by the Tri-ethenet MAC module from Xilinx. The communication layer uses the IPBus protocol to provide communication for read-out, control and configuration. The data sent to the chip and data read from chip are written and read using IPbus registers. The list of signals used to operate the chip is shown in table

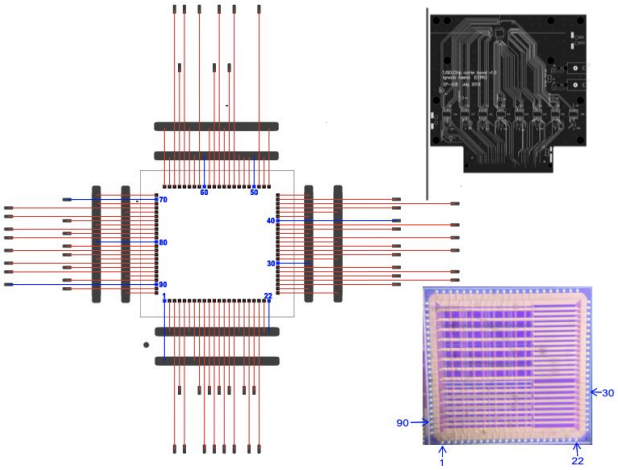

Figure 5.17: SEU_TJ180 wire-bonding schema and orientation onto the carrier board

4.1 in Chapter 4.7. The value of each signal and the control of the FSM to operate the chip is assigned from IPbus registers.

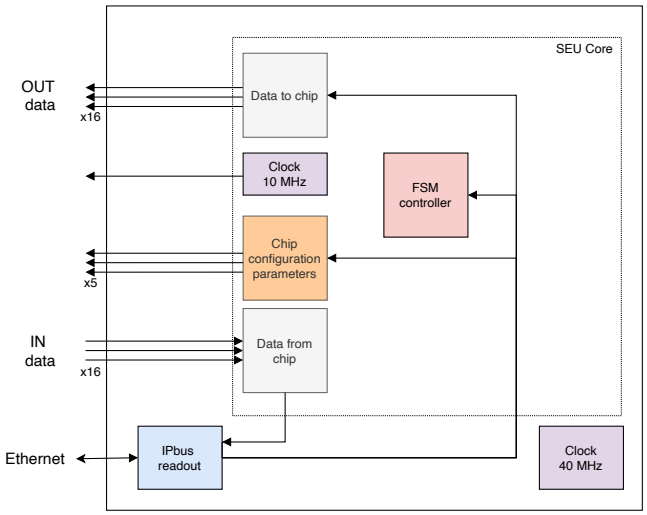

Figure 5.18: Block diagram of the SEU_TJ180 read-out firmware

A software environment has been developed for the operation of the chip. The baseline is a C++ class to communicate with the FPGA using IPbus. The class contains the methods to configure the chip, send data, read the output of the chip and perform automated tests.

5.3.2 Plans

The SEU sensitivity of the TowerJazz technology has to be measured in proton beams such as the KVI-CART at Groningen (NL) with heavy ions (Ne – Pb) with energies in the range 10 – 40 MeV/u. Tests are aimed to estimate the SEU and SEL cross sections as a function of the linear energy transfer (LET). Preparations for the beam tests include the mounting stage for the beam area.

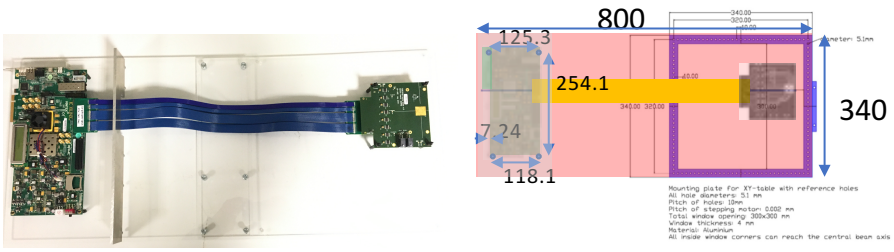

Figure 5.19: Photo (left) and (schematics) of the SEU_TJ180 read-out system mounted in stage

5.4 Conclusions

The MALTA TLU is an FPGA based system that replaces previous technology for a carry-on telescope to be a more flexible, configurable and lightweight solution. It allows remote changes of the telescope's configuration during operation, without the necessity of a person entering the beam area. Results demonstrate that the MALTA TLU meets the requirements for telescope.

An working setup has been designed and produced for the study of the radiation effects on the memory cells of TowerJazz 180 nm technology with the SEU_TJ180.

Chapter 6

Applications: the Water leak detection project

6.1 Introduction

Current water leak detection systems used in the ATLAS experiment are based in Raychem (former TraceTek) TT3000 sensing cables [36] and the TTC-1 [37] sensing readout modules, a schematic drawing of which is shown in Fig. 6.1. Cables are based on conductive polymer & fluoropolymer tubes that change their resistivity when exposed to water. Even if we ignore the fact that cables can only target very small surfaces they only provide a binary response, despite of the change in resistance that could be measured on the TTC-1. To cover a large surface using this technology is a huge investment and it is prone to miss water drops, failing to report the leak. These polymer-based systems are also degraded over time and during the last years they have been proven to be an unreliable solution.

This chapter gives a detailed description of a new water leak detection solution based on a carbon nano-tubes (CNTs) material proposed for the ATLAS detector and galleries as well as for similar experiments. We have named the project as RELIANCE (Reliable Liquid Detection for Critical Environments).

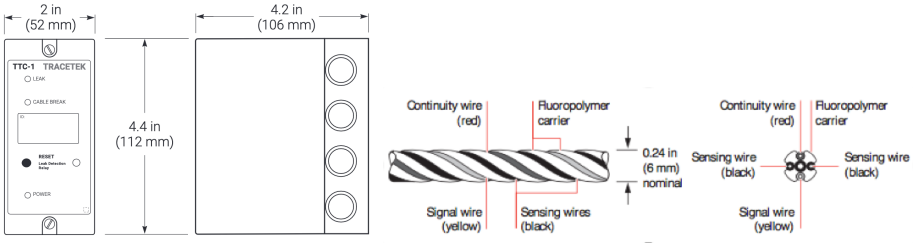

Figure 6.1: Left: TTC-1 sensing readout module. Right: TraceTek TT3000 sensing cable.

6.2 Detector selection

In order to develop a water leak detection system, it is necessary to consider the sensing material and the read-out module. The sensing material changes resistance in the presence of water, and the readout module monitors the electroconductive material.

The goal of developing a reliable and cost-effective water leak detection for large surfaces leads to the research of a water sensitive material, which can be produced in large quantities, in a low-cost industrial manner and with a small degradation factor. The research was focused on water sensitive conductive paper-like materials.

Initially, several samples of conductive paper-like material were procured and tested. Samples provided from TFP [38] which are nonwoven papers, based on Nickel Coated Carbon and Copper & Nickel Coated Carbon, were interesting candidates but the response to water was very poor. Fig 6.2 shows an example of the current as a function of voltage of these samples for the dry and wet cases, by comparing the current flow through the material in the presence of water to the dry conditions. Despite a 16% SNR observed, the current was of the order of nano-amperes (10e-9) which makes it difficult for our application. Plot on the left is for a dry sample, and on the right for a sample containing 2 ml of water. These and the following measurements were carried out with a Keithley 2410 pico-amperimeter.

After several samples, the best performing candidate was the Smart Paper [39], pictures of which are shown in Fig. 6.3, developed by the University of Washington.

Fig. 6.4 shows the current as a function of voltage, for a dry sample on the left, and for a sample with 2 ml on the right. In this case, the Smart Paper acts like a resistor, increasing the current linearly with the voltage across the sample. Samples with different amounts of water produce an almost identical curve. From these measurements, we

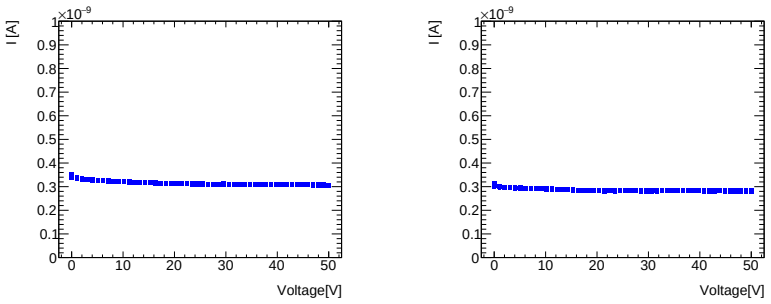

Figure 6.2: Current as a function of voltage of Copper & Nickel Coated Carbon Veil 8g/m^2. Left: dry. Right: sample with 2 ml of water.

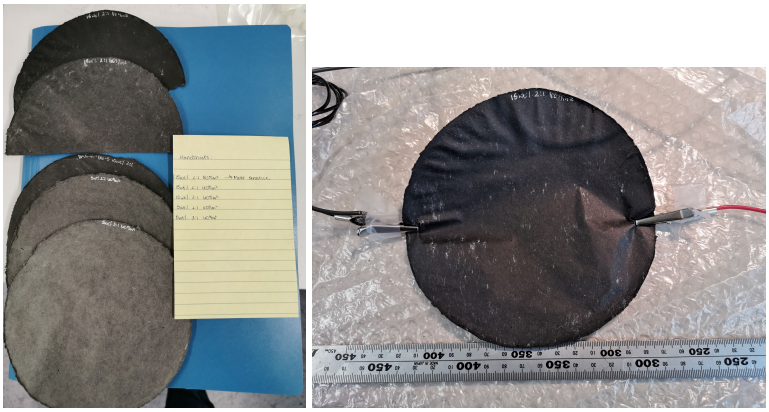

Figure 6.3: Left: 16 cm diameter Smart Paper samples with different concentrations of CNTs. Right: Smart Paper sample under measurement

can deduce that the voltage used to measure water changes is not an important factor for the water detection. The most important observable in our case is the difference of

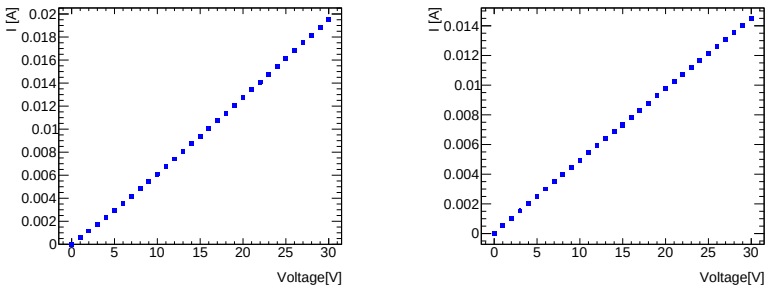

Figure 6.4: Current as a function of voltage of Smart Paper. Left: dry. Right: sample with 2 ml of water.

resistance between the wet and dry sample. ΔR is expressed as a formula in Eq.6.1.

$$\Delta R = R_{wet} - R_{dry} \tag{6.1}$$

Fig. 6.5 shows the resistance measurement of the Smart Paper with 4 ml of water poured on the sample after 11 hours producing an increase in resistance of $\Delta R > 2k\Omega$.

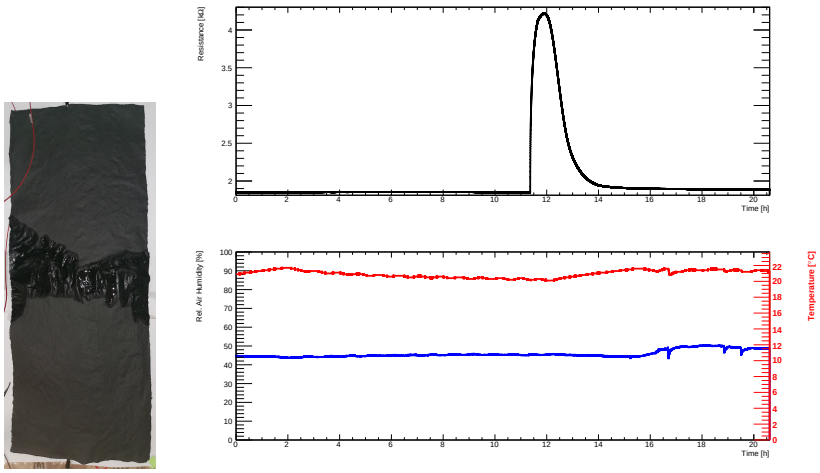

Figure 6.5: Left: 75x30 cm sample of Smart Paper with 4 ml of water. Right: On top resistance measure by time and on the bottom temperature in red and relative humidity in blue.

The Smart Paper is a lightweight, flexible and electrically conductive paper. The method that is prepared by consists in mixing carbon nanotubes (CNTs) with cellulose nano fibers (CNF) during the standard paper making process. This process results in formation of electric paths through the whole volume of the paper. The non-woven network of fibers, with the incorporation of conductive filler, performs sensitive resistive changes due to the dispersion of the fibers as a consequence of external conditions such as temperature, mechanical deformation and mainly humidity. The content of CNT on the paper is expressed as percentage of the total mass of the paper (*wt%*). Expressed as a formula in Eq. 6.2, mass fraction of a substance within a mixture is the ratio w_i of the mass m_i of that substance to the total mass m_{tot} of the mixture.

$$w_i = \frac{m_i}{m_{tot}} \tag{6.2}$$

Most of the research on CNT-cellulose papers are based in CNT contents up to 70 *wt%*

[40] [41], although contents higher than 15 *wt*% present difficulties capturing the CNTs within the cellulose fibers[42]. The content and ratio of CNTs and CNFs prepared during the making process has strong influence on the signal response with the highest sensitivity at 2:1 CNT:CNF ratio.

The Smart Paper was selected as a candidate for the detector due to its detecting performance, quasi industrial production and wide selection of density parameters, and different options for the CNF:CNT ratio controllable at production and its impact on signal detection. The particularity of the Smart Paper is that when in contact with water it reduces the conductivity increasing the resistance. This is contrary to the typical change in conductivity of paper (cellulose) with water.

6.3 Characterization of detector

The Smart Paper was characterized in terms of ΔR to different volumes of water and variations in environmental factors such as temperature, humidity and plastic deformations. The following paragraphs show different results of these studies to determine the electrical conductivity and factors that can have and influence on it.

Due to the intrinsic nature of the paper, influence of humidity and temperature have been considered. ATLAS galleries generally have stable controlled environmental conditions, humidity is 50% ±10% and temperature is 22° ± 1 °C. Proximity to heat sources or large air flows can heavily alter conditions and could affect water detection or trigger high changes in resistance. Although temperature and humidity clearly affect the resistance, as Fig. 6.6 shows, we can not establish correlation between them.

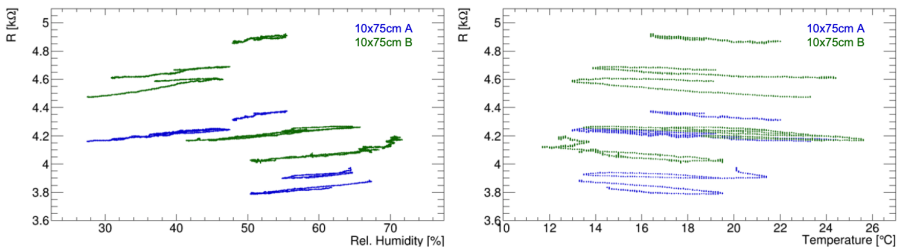

Figure 6.6: Measurements of two samples of Smart Paper without water. Left: Resistance vs relative humidity. Right: Resistance vs temperature.

6.3.1 Tests methodology

Physical connection between detector and the readout system has been studied using several attachment methods: aluminum tape, medical electrodes, copper wire sewed to the paper and different types of clips. Amongst them, the aluminum tape introduced unexpected noise and medical electrodes resulted in a progressive loss of sensitivity with time. Standard flat and crocodile clips have best performance regarding precision and usability although a better connection mechanism still needs to be identified.

To compare the impact of the clips, Fig. 6.7 shows resistance distributions for flat and crocodile clips. The RMS is 0.8 for flat ones, and 1.8 for crocodile ones. This measurement was repeated in different samples with similar results. To improve water detection, electrodes are placed at the maximum distance (length), forcing the longest electric path along the paper and therefore increasing the probability of being affected by areas with water.

Fig. 6.8 shows the linearity of the resistance versus the distance between the electrodes, with flat and crocodile clips. Resistance is increased with the distance due to the intrinsic resistivity of the Smart Paper caused by the conductive net of the CNF:CNT bonds in the paper and the clips.

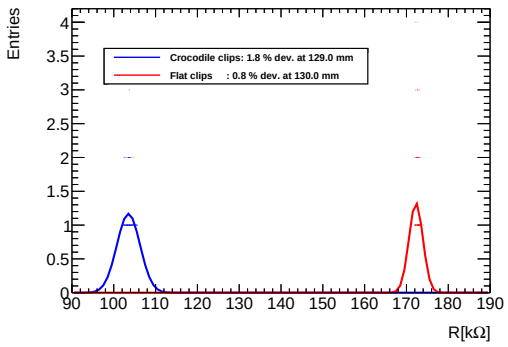

Figure 6.7: Distribution of resistance measurements for flat (red) and crocodile (blue) clips measurements at equal distance.

6.3.2 Characterization

Regarding the impact of water in the Smart Paper resistance, the following factors have being observed to play an important role: initial resistance of the paper, amount of water, wet surface relative to the sample size, shape and absorption pattern. This will

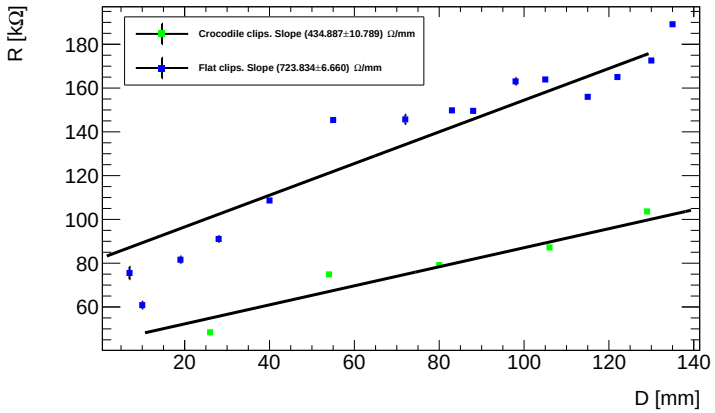

Figure 6.8: Linearity of resistance by distance. Flat clips in blue and crocodile clips in green.

be discussed in the following section.

Fig. 6.9 shows a negative correlation between the resistance in dry conditions and sample size. Measurements include samples from 75×1 cm (0.0075m^2) to the largest samples that could be manufactured at the time, 75×30 cm (0.225 m^2).

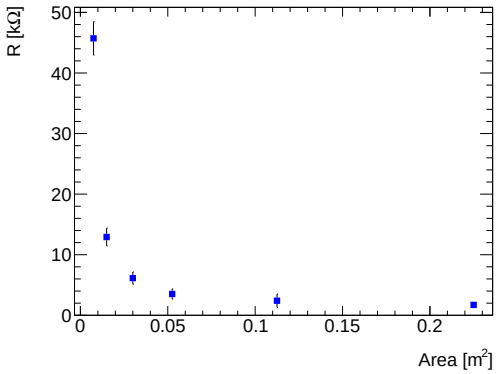

Figure 6.9: Resistance vs sample size in dry samples.

To determine the range of paper sizes that are suitable for detection of small volumes of water, a study was conducted to establish the performance at different sizes. Fig. 6.10 shows the ΔR in kΩ for measurements with 0.5 ml. Although their decrease in the response is large, being ΔR = 0.2 [kΩ] in the largest samples, it is an impressive ΔR, compared to ΔR = 200 [nΩ] of TFP samples, and good enough for signal detection even for large samples at only 0.5 ml.

Fig. 6.11 shows the minimum volume of water necessary to reach ΔR > 7 [kΩ]

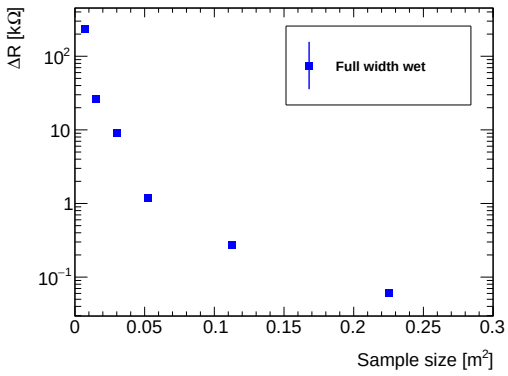

Figure 6.10: ΔR[kΩ] vs sample size in tests with 0.5 ml.

(left) and ΔR > 0.2 kΩ (right) for different sample sizes. On the left, we observe an exponential requirement in volume of water to achieve a high ΔR such as 7 kΩ. On the right, we can observe the volume requirements to reach a ΔR > 0.2 kΩ, being 0.25 ml (less than two tablespoons) in small papers and up to 2.5 ml in larger samples such as 0.05 m^2 (75×7 cm). The different colors indicate if the full width of the paper is wet (blue) or if it has only been partially wet (red).

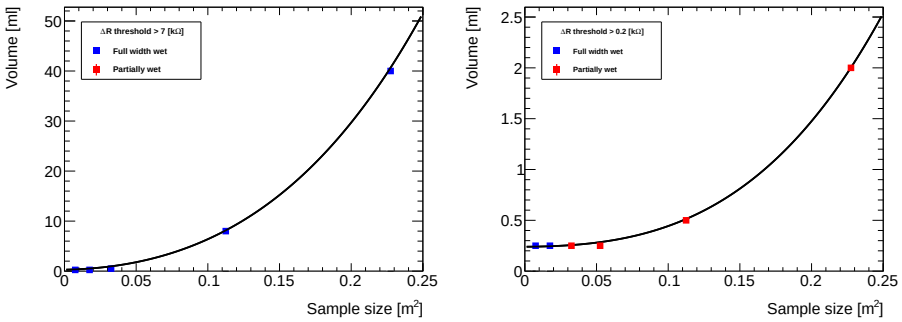

Figure 6.11: Volume of water vs sample size. Thresholds of ΔR > 6 [kΩ] (left) and ΔR > 0.2 [kΩ] (right).

The increase of ΔR is in correlation with the volume of water as observed in Fig. 6.12. As we can see, if the width of the paper is fully wet, there is an important step in the increase of ΔR. This behavior has been observed to be consistent during all the tests. The error bars are the statistical uncertainty from the various measurements with the same volume of water.

Fig. 6.13 shows the response of the Smart Paper with respect to the relative wet area. The larger the wet surface the larger the ΔR with a clear linear dependence, es-

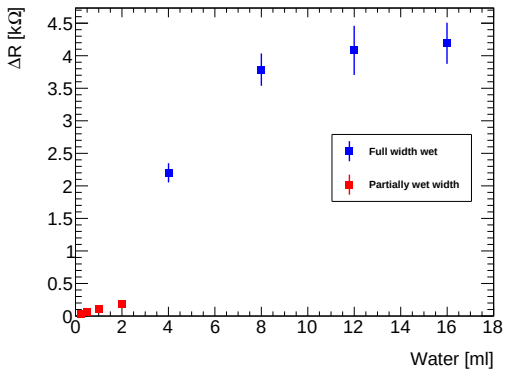

Figure 6.12: ΔR vs volume of water. Blue: wet surface reaches full width. Red: partial width is wet. Measurements with 75×30 cm Smart Paper sheets.

pecially when the full width is wet. Large variations in the resistance can be explained due to the attachment of the electrodes to the paper for different measurements, that as explained before have a large systematic which result as a small non-linearity.

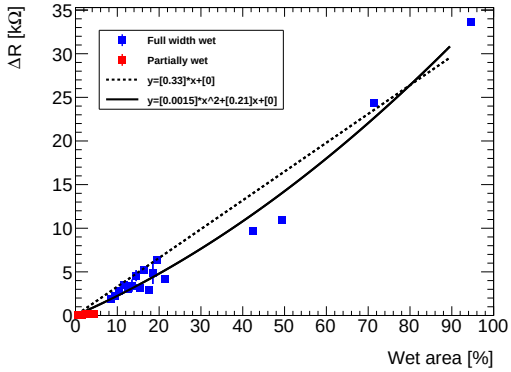

Figure 6.13: ΔR vs relative wet area. Measurements with samples between 0.03 m^2 and 0.225 m^2 and from 0.25 ml to 40 ml of water.

Fig. 6.14 shows the logarithmic increase of ΔR over wet width with an important step when the full width is wet.

6.3.3 Functional description model

Given that the Smart Paper at the microscopic scale is a network of CNT and CNF, it can be modelled as a conductive circuit with resistors which limits the flow of charge. An electrical conductivity model at the macroscopic scale is proposed on which current flows between the electrodes. As it enters the paper, current is split in parallel amongst

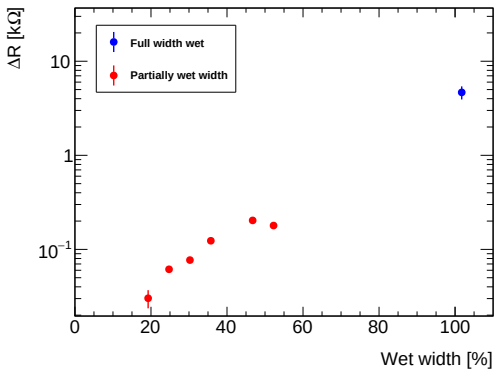

Figure 6.14: ΔR vs relative wet width. 0.225 m^2 samples with volumes of water from 0.5 ml to 16 ml.

all the width of the paper, and infinite series of resistors in parallel. As it flows along each resistor, it might find wet resistors which have a higher resistance.

We can divide the paper into a matrix of $M \times N$ resistive cells, where the change of every single one of them will affect the overall equivalent resistance between the electrodes. Eq. 6.3 shows the model matrix. R_{eq} is the total resistance of the sample, r_w is a wet resistor and r_d a dry resistor.

$$R_{eq}(M) = R_{eq} \begin{pmatrix} r_w & r_w & r_d \\ r_w & r_w & r_d \\ r_w & r_w & r_d \\ r_d & r_d & r_d \\ r_d & r_d & r_d \\ r_d & r_d & r_d \end{pmatrix} \tag{6.3}$$

Eq.6.4 shows the model definition as a sum in parallel of all resistors in series.

$$R_{eq} = \left(\sum_{i}^{n} \frac{1}{\sum_{j}^{m} (R_i j)} \right)^{-1} \tag{6.4}$$

Then we can obtain the simulated ΔR as the difference between resistance in wet R_{eq}^{wet} and the resistance in dry R_{eq}^{dry} as Eq. 6.5 shows

$$\Delta R = R_{eq}^{wet} - R_{eq}^{dry} \tag{6.5}$$

Name	Type	Init with	Unit
Matrix length	Uint16	Config.	cm
Matrix width	Uint16	Config.	cm
Wet width	Uint16	Config.	cm
Dry width	Uint16	Config.	cm
Wet resistance	Float(0,10)	Config.	kΩ
Dry resistance	Float(0,10)	Config.	kΩ

Table 6.1: Variables of the Smart Paper model.

As seen in Table 6.1 there are 6 variables in the model: matrix length, matrix width, wet length, wet width, value of dry resistors and value of wet resistors. Dry resistors has been calculated from the average of tests to be a constant 0.77 ±0.01 kΩ and the value of wet resistors has been observed to be in direct the increase wet factor as 5.

Eq. 6.6 shows an example of simulated 6×4 sample with 50% width and length wet and 1 kΩ dry resistance. The calculated ΔR is 0.75kΩ.

$$R_{eq}\begin{pmatrix} 5 & 5 & 1 & 1 \\ 5 & 5 & 1 & 1 \\ 5 & 5 & 1 & 1 \\ 1 & 1 & 1 & 1 \\ 1 & 1 & 1 & 1 \\ 1 & 1 & 1 & 1 \end{pmatrix} = 1.6 \pm 0.1k\Omega \tag{6.6}$$

To test the model, Fig. 6.15 shows a comparison between the model simulations and the data focused on partially wet width tests. On the left it is focused on width percentage and on the right on area percentage. Actual data has been narrowed to 75x30 cm samples to match the simulation. Simulations with different sizes produce close results with small deviations.

6.3.4 Other considerations

Given that the surface of the paper is conductive, any contact with conductive surfaces is expected to alter the measurements. Tests of samples wrapping a copper pipe have been taken. Although it alters the absolute value in resistance, the ΔR are very similar. Measurements of a sample in contact with a fan unit with a conductive surface produced a very noisy signal which makes water detection extremely difficult. Signal detection algorithm has to be modified accordingly. Light mechanical deformations caused by

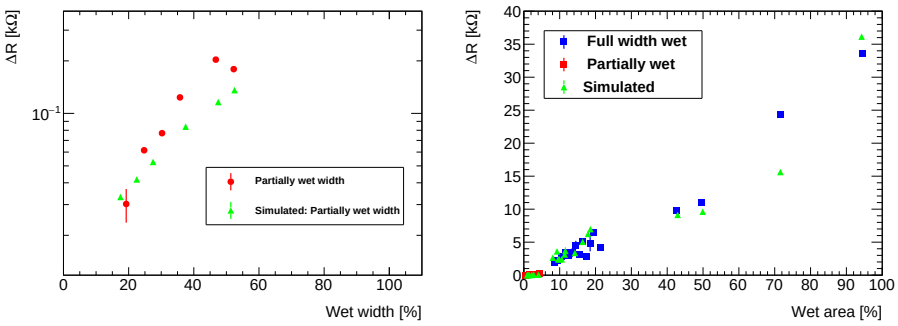

Figure 6.15: ΔR vs relative wet width (left) and ΔR vs relative wet area. Electrical model (green) and data (red). Tests correspond to 0.225m^2 samples with volumes of water from 0.5 ml to 16 ml.

normal manipulation of the paper do not affect detecting properties. Nevertheless, full bending of the paper can damage its properties.

Aging studies carried out in the University of Washington show minimal degradation of the Smart Paper properties. Fig. 6.16 shows a degradation of less than 10%, after 6 months of exposition to temperature and humidity fluctuations and after 30 cycles of full immersion in water.

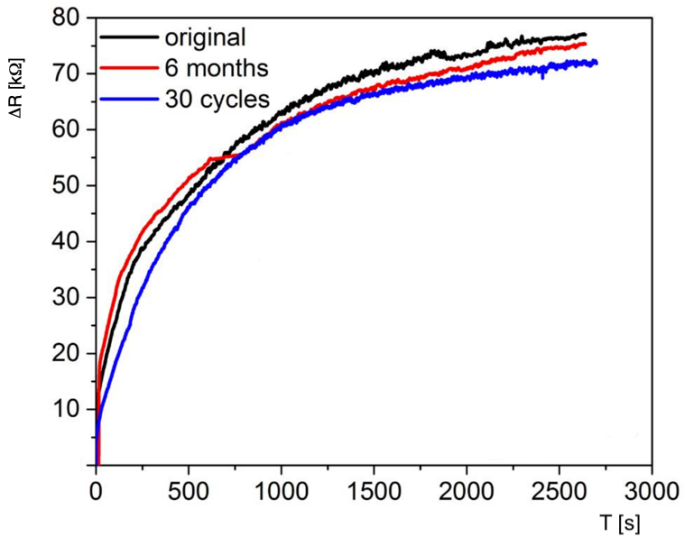

Figure 6.16: ΔR over time of samples with different degradation. From University of Washington.

During a test, the increase in resistance remains permanent along with the water presence. Therefore, the recovery is the time of natural evaporation of the water. This

obviously depends on environmental conditions, but it can be noted that the average recovery time for amounts of water over 5 ml is between 1 and 3 hours.

To summarize, there are many factors that affect the Smart Paper measurements. Some depend on the mechanical conditions of the paper and the connection to the readout. Others depend on the water: shape, amount of water, relative wet surface and width. And finally environmental conditions such as air currents, humidity and temperature.

The main conclusion after the characterization is that the Smart Paper a viable candidate to be used as detector for the project. Also, the most important factors are the amount of water and if there is a continuous dry path between the electrodes. Other factors, specially the contact with conductive surfaces and environmental humidity and temperature play a less important role but introduce noise and deviations in the signal which have to be ignored by the readout logic to distinguish them from water. This will be addressed in Section 6.4.1.

6.4 Embedded monitoring system

The Reliance box is a readout system designed and produced for the water leak detection system to detect water leaks by monitoring the Smart Paper. Three main requirements have been established: first, to provide consistent monitoring of the attached sample in the galleries. Second, to analyze the signal while ignoring false positives. And third, to communicate with DCS for configuration and to broadcast the alarm signal when given conditions are met.

The readout consists of a single board computer Raspberry Pi 4 interfaced with an ADC on a custom PCB, Fig. 6.17 shows a picture of the Reliance box. There are 8 distinguishable smaller detachable PCB modules attached to the main PCB.

Fig. 6.18 shows the schematic layout of the electronics, arrows indicate the chain of signal conditioning components, from input to the ADC. The input stage tunes the readout range from 1 kΩ to 30 kΩ and offers over-voltage protection suppressing transient voltages above 600 V using resistors and transient-voltage-suppressors (TVS). Next, composed of capacitors and inductors, there is an electromagnetic interference (EMI) filter. Followed by the passive and active filters containing a capacitive network, and operational amplifiers (OP AMP) to suppress the noise below 100 Hz and above 1 kHz.

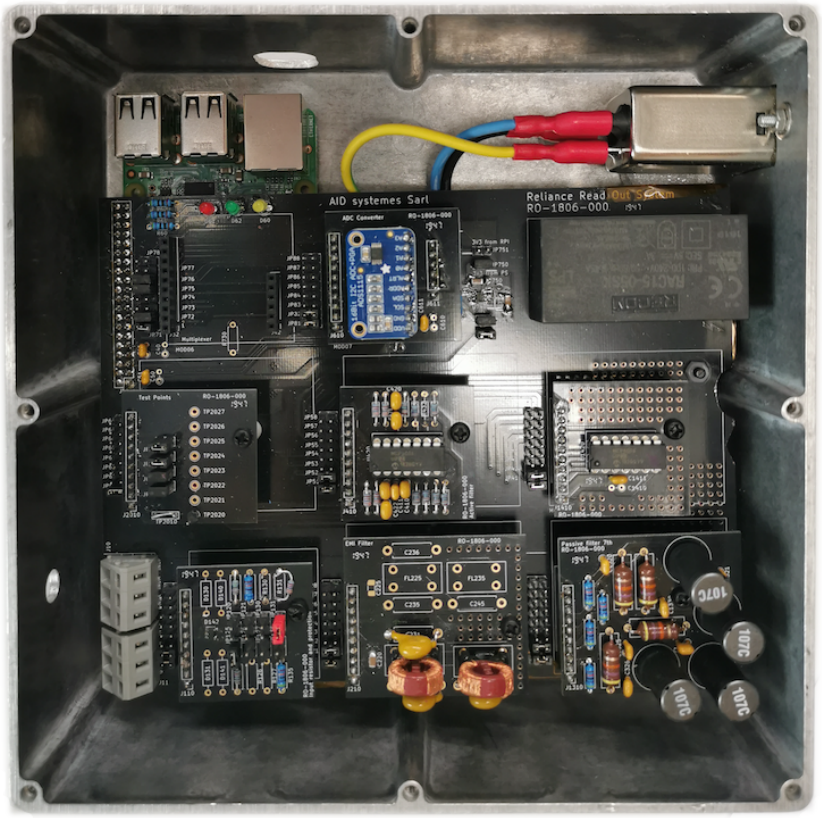

Figure 6.17: Reliance box version 2

The operational amplifier follower adapts the signal for the interface with the analog-to-digital converter ADC. The ADC is an ADS1115, a 16-bit precision differential 3.3 V which uses I^2C communication protocol with the Raspberry Pi.

The ADC counts from the ADS1115 are calibrated to Ω in the computer. The response can be modelled by a second-degree function ($f(x) = Ax^2 + Bx + C$) as shown in Fig. 6.19, where the second order degree constant is four orders of magnitude smaller than the first order degree constant. The calibration constants per gain of the ADC are listed in Table 6.2.

6.4.1 Detection algorithm

Discriminating signal variations caused by intrinsic noise or external conditions affecting the paper from variations due to presence of water requires the development of a detection algorithm. It has to address the challenge of distinguish possible large

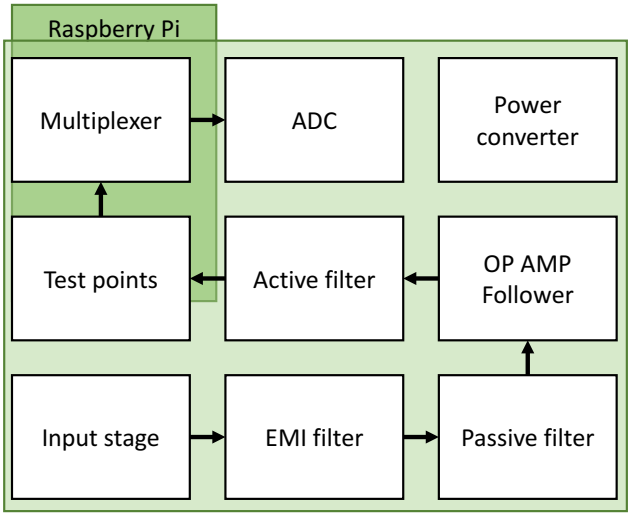

Figure 6.18: Layout diagram of the readout electronics. Arrows indicate the chain of the signal.

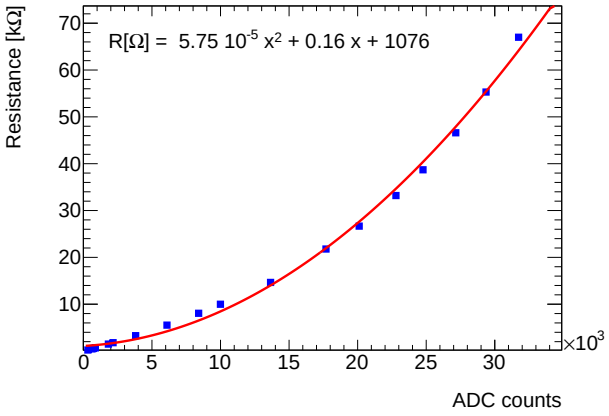

Figure 6.19: Calibrated resistance as a function of ADC counts for gain 2.

fluctuations of the background from the rapid evolution of a signal from a water leak.

This is accomplished by calculating the ratio of the average of the first m measurements ($\overline{Rm}$) and the average of the following n measurements ($\overline{Rn}$), named as Chasing Averages (CA). Due to the real-time nature of the application, the most recent sample is the last index in ($\overline{Rm}$), and the oldest sample is the first index in ($\overline{Rn}$). The Chasing

Gain	$A[10^{-5}\Omega/ADC^2]$	$B[\Omega/ADC]$	$C[\Omega]$
2/3	91.98 ±0.01	0.65	1077
1	91.99 ±0.01	0.65	1077
2	5.75 ±0.01	0.16	1076
4	5.75 ±0.01	0.16	1077
8	0.18 ±0.01	0.19	-5
16	0.18 ±0.01	0.19	-5

Table 6.2: Calibration constants for different gains of the ADC.

Averages definition is shown in Eq. 6.7.

$$\frac{\overline{R_m}}{\overline{R_n}} = \frac{\frac{1}{m}\sum_{i=0}^{m} R_i}{\frac{1}{m}\sum_{i=0}^{m+n} R_i} \tag{6.7}$$

Fig. 6.20 illustrates the monitoring of the resistance signal using different values. During this measurement, there were 0.5 ml of water poured on the sample after 1.6 hours as clearly seen in the resistance signal at the bottom in black. The lower the m, the faster will the response. The larger the n, larger the amplitude of the response. The highest CA scored value is about 1.05, with $n = 950$.

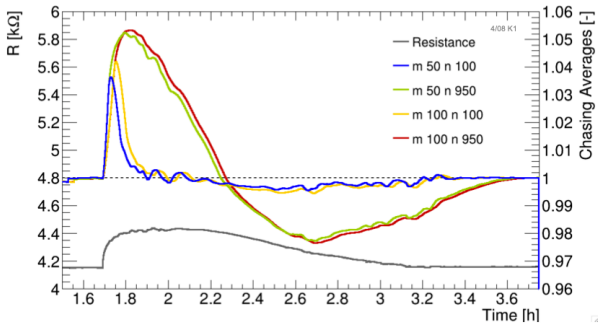

Figure 6.20: Measurement of a 75×30 cm Smart Paper with 0.5 ml of water using the Chasing Averages algorithm. Resistance and average signals over time.

Fig. 6.21 illustrates a measurement without water with different CA configurations. The noise in the signal can be explained because this sample was in contact with a conductive surface. As we can see, the Chasing Averages sigma remains lower than the previous measurement in every configuration.

Comparing both measurements, in the dry test, with $m = 100$ and $n = 900$ the CA score reaches 1.02. In the test with water, at $m = 100$ and $n = 900$ the score is above 1.05.

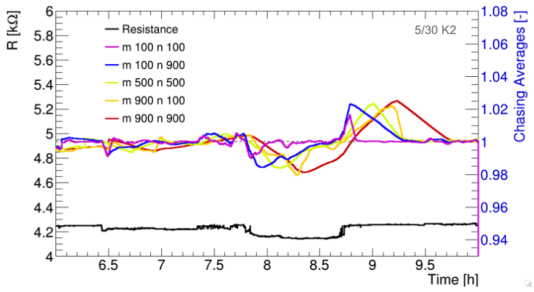

Figure 6.21: Measurement of a 75×30 cm dry Smart Paper using the Chasing Averages algorithm. Resistance and average signals over time.

Fig. 6.22 shows distributions of the chasing averages measuring background noise of two samples measured in the laboratory. The sample on the left is isolated and the one on the right is in contact with a metallic conductive surface. The sample in contact with conductive surface shows a larger distribution between CA=[0.98, 1.012] compared with CA=[0.994, 1.004]. This can be explained due to the noise introduced by the contact with the conductive surface.

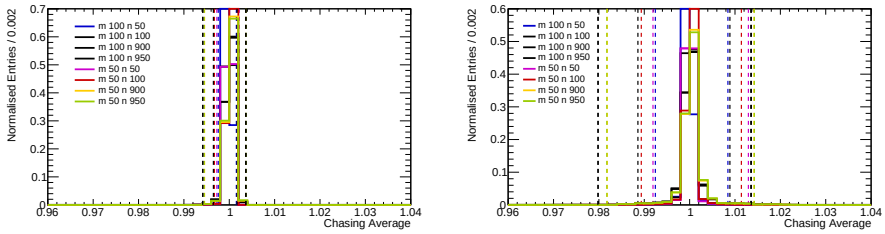

Figure 6.22: Chasing averages two distribution comparing the background noise of isolated (left) and non-isolated (right) samples. Number of entries vs chasing average index.

Fig 6.23 shows the larger distribution of chasing averages values of a measurement with 0.5 ml of water.

6.4.2 Online software

The online software is used for the operation of the Reliance box. It is executed on the Raspberry Pi, and it is composed of a library written C++, compiled with standard tools (CMake, and gcc) following the ATLAS software policy recommendations. It provides the readout operation of the ADC, conversion to resistance via calibration constants, computes the chasing averages algorithm and raises the alarm condition if

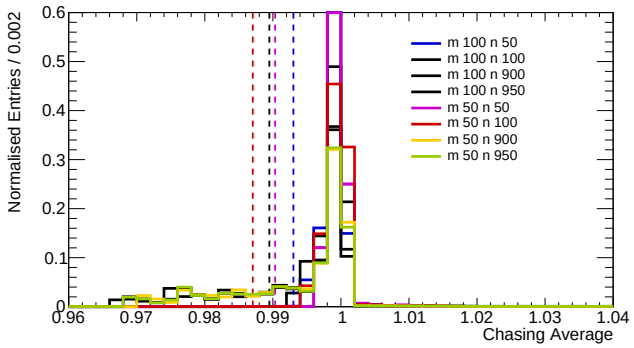

Figure 6.23: Normalized entries vs chasing averages. Measurement of Smart Paper with 0.5 ml.

the special conditions are met. The online software can be operated via Ethernet using IPBus protocol [34].

6.5 Integration into DCS

6.5.1 OPC server

The supervision of the Reliance box has been developed as a OPC Unified Architecture (OPC-UA) server [43] [44], using the Quasar framework [45][46][47]. This framework provides features such as built-in variable types, methods and advanced threading. Fig. 6.24 shows an overview of the Reliance project integration into DCS. One OPC server supervises one Reliance box, therefore a connection to each box is necessary to supervise an entire water leak detection system.

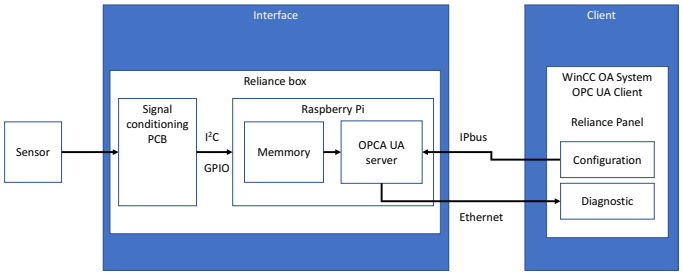

Figure 6.24: Global picture of Reliance system in ATLAS DCS

In order to handle asynchronous requests, the software implements a thread to carry out the measurements according to the state of an internal Finite State Machine (FSM)

shown in Fig.6.25. The FSM follows the state and status color and principles of the DCS ATLAS convention.

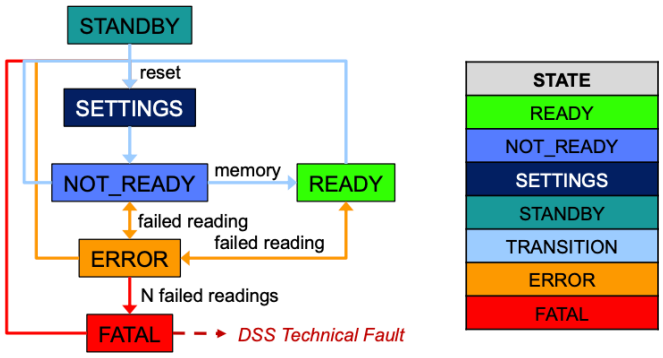

Figure 6.25: Block diagram of the Reliance software FSM.

The initial state is STANDBY during which the ADC is initialized, and the memory flushed. After one readout cycle the state changes automatically to SETTINGS where it stays for $m+n$ cycles until the Chasing Averages can be calculated and will transition to READY. Any change to the settings resets the FSM and brings it back to SETTINGS. READY is reached always after $m+n+1$ cycles. Any unexpected error will bring the FSM to FATAL state including too many measurement failures.

6.5.2 OPC server parameters

There are 10 variables defined in the OPC server design (XML file), listed in Table 6.3. ADC, Resistance, Chasing Averages and Alarm are cache type variables with forbidden address space write policy (read-only variables). They are initialized with their own value, status waiting for data, and not accepting null values, that provide an overview of the operation of the box. State Machine variable is a cache variable with delegated address space write policy, and initialized from configuration to 0 (STANDBY), that represents the internal FSM of the Reliance box online software, and can be changed by the user to interact with the Reliance box. Len D (first m samples for the chasing averages), Len C (following n samples for the chasing averages) and Gain are cache type variables with delegated address space write policy, and initialized from configuration. They can be changed by the user to interact with the Reliance box.

In detail, the ADC variable provides the raw measurement of the ADC in the Reliance box in ADC counts (16 bits), thus the possible values range from 0 to 2^{16-1}.

Name	Type	Write	Init with	Init val.	Init status	Null
ADC	Uint16	No	Val. and Status	0	Waiting	No
Resistance	Float (1k,10k)	No	Val. and Status	0	Waiting	No
Chasing Avg.	Float (0,10)	No	Val. and Status	1	Waiting	No
Alarm	Bool	No	Val. and Status	False	Waiting	No
Action	Byte	Delegated	Configuration	0	Config.	No
Time Stamp	Uint32	No	Val. and Status	0	Waiting	No
Location	String	No	Configuration	Location	Config.	No
Len D	Uint32	Delegated	Val. and Status	0	Waiting	No
Len C	Uint32	Delegated	Val. and Status	0	Waiting	No
Gain	Uint32	Delegated	Val. and Status	2	Waiting	No

Table 6.3: Variables of the Reliance OPC server.

The Resistance variable provides the resistance value of the sensor calibrated into Ω. The Chasing Average variable provides the value of the water leak detection algorithm, which ranges from 0 to 10. Values above 1.05 are typically associated with the Alarm value being true, as it is the variable that indicates the detection of water by the sensor. The Action variable is an enumerator of the Reliance box internal FSM states. Values are STANDBY=0, SETTINGS=1, READY=2, ERROR=3, FATAL=4. In order to reset the box, the typical action is to write value 0 to the Action, this will restart the internal FSM of the Reliance box, clear the memories, and restart the operation of the box.

6.5.3 DCS panel

The Reliance water leak detection system has been integrated into the Safety Project of DCS. Fig. 6.26 shows DCS online monitoring panel of the first Reliance box. Each box is associated with a location, and displays the value of the Resistance variable, which is provided in units of kΩ. The colour of the resistance text field is determined by the Alarm variable. Green corresponds to a false value indicating no leak, and red corresponds to a true value indicating a leak. A reset button beside the resistance text field could be used to write value 0 to the State Machine variable. Any change of Alarm value from false to true, should trigger a message to OPM with the corresponding location of the Reliance box to warn about the presence of water.

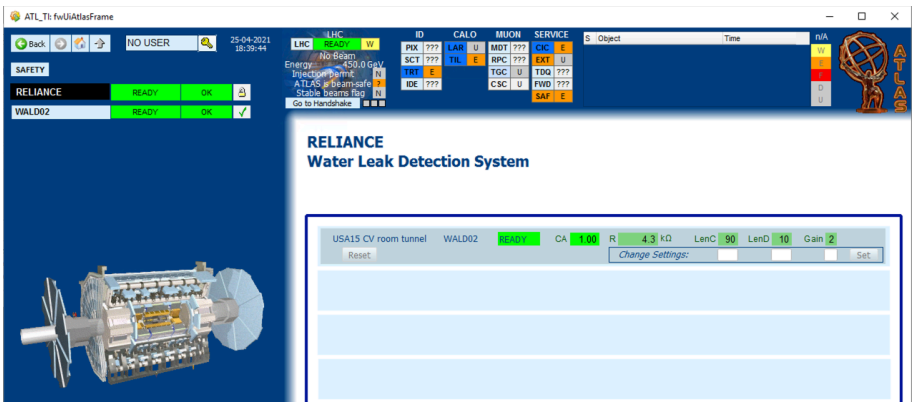

Figure 6.26: Water leak detection system integrated in DCS.

6.6 Operation in the ATLAS galleries

CERN Safety Instruction 41 [48] regarding the requirements for plastics and non-metallic materials installed at CERN including underground installations has been taken into account. An effort must be made to use materials which do not burn easily, evolve smoke of low optical density, low corrosiveness, and low toxicity. Therefore, it is fair to note that the base material for the Smart Paper is flammable pulp-made out of wood, and that extra precautions have been taken to apply a flame retardant coating on the smart paper which has been observed cool down the surface, delay the combustion, and prevent fire propagation [49].

No alternative material has been found available in the current market for this technology that shows similar water leak detection performance. The amount of material to be installed per water leak sensor is equivalent to 10 g of wood (10 cm $\times$ 75 cm $\times$ 120 g/cm^2). Therefore, it is our understanding that the risk associated to each Smart Paper sensor is low, and is a viable candidate for installation in the ATLAS galleries

ATLAS experimental galleries present many challenges due to electro-magnetic interference and high airflow currents. Fig. 6.27 shows a Reliance box installed in a rack in USA15 (left) and the Smart Paper sensor in the entrance of a tunnel where leaks are frequent.

Fig. 6.28 shows a 2 weeks measurement in the tunnel with a intentional leak to test the detector. On the left we can see the resistance over time and on the right the chasing averages score measured online. Fig. 6.29 shows the distribution during the 2 weeks measurement and the leak. Chasing averages scores above 1.5 which is above

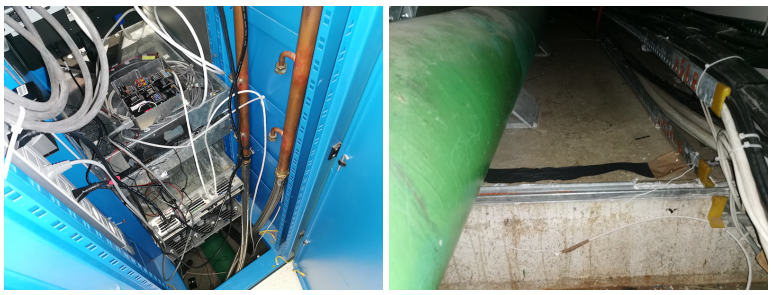

Figure 6.27: Reliance box (left) monitoring the Smart Paper (right) in the entrance of the tunnel between USA15 and the CV room.

the established a threshold.

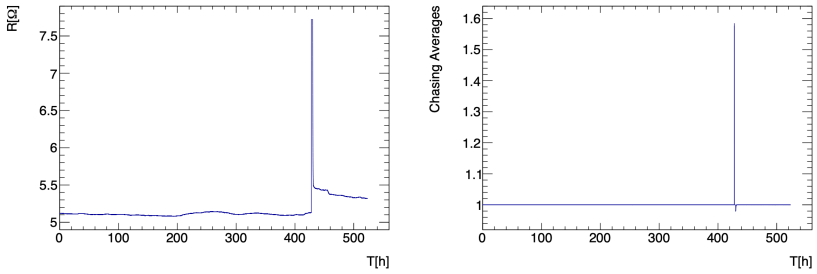

Figure 6.28: Resistance vs time (left) and chasing averages score vs time (right). Measured with the Reliance box.

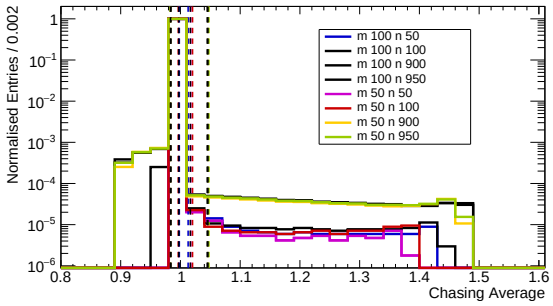

Figure 6.29: Chasing averages score distribution.

6.6.1 Commissioning

Ten Reliance boxes are considered to be installed in the ATLAS galleries before Run 3. Places where standard detection has not been possible such as inside selected racks or wrapped around pipes are interesting candidates. The locations match those of the

Name	Gallery	Location
WALD01	UX15	Muon cooling station A
WALD02	UX15	Muon cooling station C
WALD03	UX15	Tile cooling station
WALD04	UX15	LAr cooling station
WALD05	USA15	Y.22-14.A1
WALD06	USA15	Racks level 2
WALD07	To be decided	To be decided
WALD08	To be decided	To be decided
WALD09	To be decided	To be decided
WALD10	To be decided	To be decided

Table 6.4: Location of Reliance boxes in the ATLAS galleries

cooling stations in UX15 and racks in USA15 Level 2. Table 6.4 shows a preliminary list of proposed locations for the Reliance boxes in the ATLAS galleries.

6.7 Conclusions

This chapter has described the design and development of a water leak detection solution based on a carbon nano-tubes (CNTs) based paper. The electrical properties have been characterized to detect water and ignore environmental factors such as temperature changes and EM noise. The supervision of the detector is carried out by a custom read-out system and an algorithm that ignores these factors. It is able to detect very small amounts of water, starting from 0.25 ml, in a surface of 75×7 cm. The project has been integrated as part of the Detector Control System (DCS) and the commissioning of the boxes in the ATLAS galleries will be carried out before Run 3.

Chapter 7

Summary and outlook

Over the course of the work of this thesis several aspects about the safety and control systems in the ATLAS experiment have been discussed and it has been a great opportunity to make contributions in a broad range of technologies and areas.

A key objective of this thesis was to evaluate the safety of the ATLAS infrastructure which has been addressed by the development of the ATLAS Expert System. To address this matter, a good knowledge of the infrastructure has been gathered from documentation and experts of many areas. This work has achieved the development of the ATLAS Expert System, a knowledge base of the experiment in the form of a simulation with a easy-to-use user interface similar to those used in the SCADA systems.

It has become a tool used by ATLAS Technical Coordination as an intervention planning tool in the standard procedures for interventions. Allowing the deep understanding of the extent of the intervention and allowing for implementation of compensatory measures to reduce their impact. It extends its functionality in risk analysis tools like Fault Tree Analysis. It also helps in the understanding of real events with a Most Probable Cause tool that answers to the question of what can be the cause of a problem.

The Expert System is a live system, and it will only be useful while it is kept up to date with the modifications to the infrastructure and detectors foreseen during the life of the experiment. It must be pointed out that the interpretation of a complex system like the ATLAS experiment is just a simplification that requires an abstraction and generalization effort. This process still requires a deductive attitude, and many hours of thinking. The Expert System is still far from being capable of learning on its own or

interpreting the schematics of a cooling plant without the expert knowledge. However, many tools have been made available to make this process easier for future generations of experts.

Additionally, a contribution to the safety systems of the ATLAS infrastructure has been targeted to reduce the risk from water leaks in the experiment areas. A new water leak detection solution based on a paper-like material with carbon nano-tubes have been developed for the ATLAS detector infrastructure and similar experiments.

The development of a water leak sensor based on cellulose micro-fibers has an extensive impact on sustainability of the ATLAS experiment. Such a sensor has a huge potential to become a new standard for water sensing technology given its large sensitivity and non solubleness in water. Despite one of the challenges for this technology is the connectivity with a read-out system that has to be compatible with industrial processes, the deployment of this technology in ATLAS, will provide increased understanding of the development of a water leak and the protection of very expensive equipment that could not be provided with the current water leak detection system.

Another key objective of this thesis is the contribution to the characterization of Pixel detectors technology, focused on the MALTA family of Monolithic Active Pixel Sensors which target the High Luminosity LHC and future HEP experiments.

A MALTA TLU has been developed for the recently created beam telescope that uses MALTA based planes. The new TLU explores the benefits of using FPGA systems to replace the NIM technology previously used. The benefits obtained are many, a far more lightweight and cheaper electronics, more flexibility in the configuration and usage; and less interruptions during operation of the telescope due to the remote capabilities of FPGAs. The FPGA based MALTA TLU has proven its capabilities during beam tests campaigns with results that meet the requirements for telescope.

A framework has been designed and produced for the study of the radiation effects in the memory cells technology used in the MALTA family of pixel detectors in TowerJazz 180 nm using the dedicated SEU_TJ180 chip. These studies are necessary to benchmark the technology to target the installation in a HEP experiment like the last layer of the ATLAS ITK.

Acronyms

ALICE	A Large Ion Collider Experiment
ATLAS	A Toroidal LHC AparatuS
CNF	Carbon Nano-Fibers
CNT	Carbon Nano-Tubes
CERN	European Organisation for Nuclear Research
CMOS	Complementary Metal-Oxide-Semiconductor
CSC	Cathode Strip Chambers
DAC	Digital to Analogue Conversion
DCS	Detector Control System
DESY	Deutsches Elektronen-Synchrotron
DSS	Detector Safety System
DUT	Device Under Test
ELSA	Elektronen-Stretcher Anlage
EM	ElectroMagnetic
EMEC	ElectroMagnetic End-cap Calorimeter
FIFO	First In First Out
FPGA	Field Programmable Gate Array
HEP	High Energy Physics
IBL	Inner Barrel Layer
ID	Inner Detector
ITk	ATLAS Phase 2 Inner Tracker
L1A	Level-1 Accept
LET	Linear Energy Transfer
LHC	Large Hadron Collider

LVDS	Low-Voltage Differential Signalling
MAPS	Monolithic Active Pixel Sensors
MDT	Monitored Drift Tube chambers
MOS	Metal Oxide Semiconductor
MOSFET	Metal Oxide Semiconductor Field Effect Transistor
NIEL	Non-ionizing Energy Loss
ODH	Oxygen Deficiency Hazard
RPC	Resistive Plate Chamber
SMA	Sub-Miniature version A
SPS	Super Proton Synchrotron
TGC	Thin Gap Chambers
TRT	Transition Radiation Tracker
TC	Technical Coordination
OPC-UA	Object Process Control Unified Architecture
PCB	Printed Circuit Board
RAD	Radiation Absorbed Dose
RELIANCE	Reliable Liquid Detection for Critical Environments
SEE	Single Event Effect
SEL	Single Event Latch-up
SEU	Single Event Upset
TID	Total Ionizing Dose
VME	Versa Module Eurocard
wt%	Percentage by mass

Bibliography

[1] The ATLAS Collaboration. The ATLAS experiment at the CERN Large Hadron Collider. *Journal of Instrumentation*, 3(08):S08003, August 2008.

[2] The CMS Collaboration. The CMS experiment at the CERN LHC. *Journal of Instrumentation*, 3(08):S08004, August 2008.

[3] The LHCb Collaboration. The LHCb experiment at the CERN LHC. *Journal of Instrumentation*, 3(08):S08005, August 2008.

[4] The ALICE Collaboration. The ALICE experiment at the CERN LHC. *Journal of Instrumentation*, 3(08):S08002, August 2008.

[5] A. Ledeul et al. Remus: The new cern radiation and environment monitoring unified supervision. In *Proc. 15th Int. Conf. on Accelerator and Large Experimental Physics Control Systems (ICALEPCS'15)*, pages 574–577. JACoW Publishing, 2015.

[6] O. Beltramello et al. The Detector Safety System of the ATLAS experiment. *Journal of Instrumentation*, 4(09):P09012, Sep 2009.

[7] A. Barriuso Poy et al. The Detector Control System of the ATLAS experiment. *Journal of Instrumentation*, 3(05):P05006, May 2008.

[8] I. Asensi et al. Planning of interventions with the ATLAS expert system. In *Proc. 17th Int. Conf. on Accelerator and Large Experimental Physics Control Systems (ICALEPCS'19)*, page 105. JACoW Publishing, 2019.

[9] A. Wardzinska et al. The evolution of CERN EDMS. *Journal of Physics: Conference Series*, 664(3):032032, Dec 2015.

[10] M. Negnevitsky. *Artificial Intelligence: A Guide to Intelligent Systems*. Addison-Wesley Longman Publishing Co., Inc., USA, 1st edition, 2001.

[11] B. K. Bose. Expert system, fuzzy logic, and neural network applications in power electronics and motion control. *Proceedings of the IEEE*, 82(8):1303–1323, 1994.

[12] R. Jones et al. The OKS persistent in-memory object manager. *IEEE TNS*, 45(4):1958–1964, 1998.

[13] Networkx, 2020 [sotware] version 2.3. https://networkx.org/.

[14] Mxgraph, 2020 [sofware] version 4.1.0. https://github.com/jgraph/mxgraph.

[15] I. Asensi et al. ATLAS Technical Coordination Expert System. *EPJ Web Conf.*, 214:05035, 2019.

[16] A. Myers. *Complex system reliability*. Springer, London, 2010. http://link.springer.com/10.1007/978-1-84996-414-2.

[17] L. Rossi et al. *Pixel detectors: from fundamentals to applications*. Particle acceleration and detection. Springer, Berlin, 2006.

[18] Particle Data Group. Review of Particle Properties. *Phys. Rev. D*, 86(1):010001, 2012.

[19] N. S. Saks et al. Radiation Effects in MOS Capacitors with Very Thin Oxides at 80°K. *IEEE Transactions on Nuclear Science*, 31(6):1249–1255, 1984.

[20] N. S. Saks et al. Generation of Interface States by Ionizing Radiation in Very Thin MOS Oxides. *IEEE Transactions on Nuclear Science*, 33(6):1185–1190, 1986.

[21] I. Jun et al. Proton non-ionizing energy loss (NIEL) for device applications. *IEEE Transactions on Nuclear Science*, 50(6):1924–1928, 2003.

[22] E. L. Petersen et al. Rate prediction for single event effects — a critique. *IEEE Transactions on Nuclear Science*, 39(6):1577–1599, 1992.

[23] I. Asensi et al. MALTA: an asynchronous readout CMOS monolithic pixel detector for the ATLAS high-luminosity upgrade. *Journal of Instrumentation*, 14(06):C06019–C06019, Jun 2019.

[24] C. Solans Sanchez et al. Monolithic pixel development in TowerJazz 180 nm CMOS for the outer pixel layers in the ATLAS experiment. *Journal of Instrumentation*, 13(01):C01023–C01023, Jan 2018.

[25] I. Asensi et al. Mini-MALTA: radiation hard pixel designs for small-electrode monolithic CMOS sensors for the high luminosity LHC. *Journal of Instrumentation*, 15(02):P02005–P02005, Feb 2020.

[26] Xilinx Virtex-7 FPGA VC707. https://www.xilinx.com/products/boards-and-kits/ek-v7-vc707-g.html.

[27] Xilinx Kintex-7 FPGA VC705. https://www.xilinx.com/products/boards-and-kits/dk-k7-embd-g.html.

[28] C. Marin Tobon. *PADRE pixel read-out architecture for Monolithic Active Pixel Sensor for the new ALICE Inner Tracking System in TowerJazz 180 nm technology*. PhD thesis, Universitat Politècnica de València. Departamento de Ingeniería Electrónica, 2017. https://cds.cern.ch/record/2316141.

[29] C. Marin Tobon et al. Radiation hardness and detector performance of new 180 nm CMOS MAPS prototype test structures developed for the upgrade of the ALICE Inner Tracking System. In *IEEE Nuclear Science Symposium and Medical Imaging Conference (2013 NSS/MIC)*, pages 1–5, 2013.

[30] M. Kiehn et al. Proteus beam telescope reconstruction [software] version v1.4.0. https://doi.org/10.5281/zenodo.2586736, March 2019.

[31] C. Kleinwort. General broken lines as advanced track fitting method. *Nucl. Instrum. Methods. Phys. Res. A*, 673:107–110, 2012.

[32] S. Spannagel et al. Allpix2: A modular simulation framework for silicon detectors. *Nucl. Instrum. Methods. Phys. Res. A*, 901:164–172, Sep 2018.

[33] A. Sharma. MALTA FMC Board Version 4.0. Tech Rep. CERN EDMS Number 2142554, 2019. https://edms.cern.ch/document/2142554/.

[34] C. Ghabrous Larrea et al. IPbus: a flexible Ethernet-based control system for xTCA hardware. *Journal of Instrumentation*, 10:C02019, 02 2015.

[35] I. Asensi. TJ SEU Chip carrier board. Tech Rep. CERN EDMS Number 2261607 v.1.1, 2019. https://edms.cern.ch/document/2261607/1.1.

[36] NVENT Raychem TraceTek. *Sensing Cable for Conductive Liquids*, 2018. TraceTek-DS-H53829-TT3000-EN-1805.

[37] NVENT Raychem TraceTek. *Sensing Module with Relay Contacts*, 2021. TraceTek-DS-H53587-TTC1-EN-2105.

[38] Technical fibre products. https://www.tfpglobal.com.

[39] A. Dichiara et al. Smart papers comprising carbon nanotubes and cellulose microfibers for multifunctional sensing applications. *J. Mater. Chem. A*, 5:20161–20169, 2017.

[40] P. Zhipeng et al. Fabrication and application of carbon nanotubes/cellulose composite paper. *Vacuum*, 122:135 – 142, 2015.

[41] K. Myounguk et al. Structures, electrical and mechanical properties of epoxy composites reinforced with MWCNT-coated basalt fibers. *Composites Part A: Applied Science and Manufacturing*, 123:123 – 131, 2019.

[42] Do-Hyun et al. Conductive carbon nanotube paper by recycling waste paper. *RSC Adv.*, 5:32118–32123, 2015.

[43] OPC Foundation Unified Architecture. https://opcfoundation.org/about/opc-technologies/opc-ua.

[44] W. Mahnke et al. *OPC Unified Architecture*. Springer, Berlin, 2009.

[45] S. Schlenker et al. Quasar - A Generic Framework for Rapid Development of OPC UA Servers. In *Proc. 15th Int. Conf. on Accelerator and Large Experimental Physics Control Systems (ICALEPCS'15)*, page WEB3O02, 2015.

[46] S. Schlenker et al. Generic OPC UA Server Framework. *Journal of Physics: Conference Series*, 664(8):082039, dec 2015.

[47] P. Nikiel et al. Quasar : The Full-Stack Solution for Creation of OPC-UA Middleware. In *Proc. 17th Int. Conf. on Accelerator and Large Experimental Physics Control Systems (ICALEPCS'19)*, 2019.

[48] CERN. Revised Safety Instruction 41 EDMS Number 335806, Nov 2005. https://edms.cern.ch/document/335806.

[49] A. Dichiara et al. Lignin-modified carbon nanotube/graphene hybrid coating as efficient flame retardant. *International Journal of Molecular Sciences*, 18(11), 2017.

List of Figures

List of Tables